2013

Determination Of Adhesive Strength And Freezing Rate Of Ice On Aircraft Structures At Subcooled Temperatures

Elijah Mendoza Kibler
North Carolina Agricultural and Technical State University

Determination of Adhesive Strength and Freezing Rate of Ice on Aircraft Structures at Subcooled Temperatures

Elijah Mendoza Kibler

North Carolina A&T State University

A thesis submitted to the graduate faculty

in partial fulfillment of the requirements for the degree of

MASTER OF SCIENCE

Department: Mechanical Engineering

Major: Mechanical Engineering

Major Professor: Dr. John P. Kizito

Greensboro, North Carolina

2013

School of Graduate Studies

North Carolina Agricultural and Technical State University

This is to certify that the Master's Thesis of

Elijah Mendoza Kibler

has met the thesis requirements of

North Carolina Agricultural and Technical State University

Greensboro, North Carolina

2013

Approved by:

Dr. John P. Kizito	Dr. Cynthia K. Waters
Major Professor	Committee Member
Dr. Vinayak N. Kabadi	Dr. Samuel Owusu-Ofori
Committee Member	Department Chair

Dr. Sanjiv Sarin

Dean, The Graduate School

Biographical Sketch

Elijah Mendoza Kibler was born on July 9, 1988 in Washington, D.C. He attended North Carolina Agricultural and Technical State University, where he graduated with his Bachelors of Science in mechanical engineering with highest honors in 2011. From 2010 to 2013, he conducted research for the NASA Center of Aviation Safety at North Carolina Agricultural and Technical State University. In 2012 he received support for his research from the National Space Grant College Fellowship Program, and the North Carolina Space Grant Consortium, receiving the North Carolina Space Grant for 2012-13. Elijah Mendoza Kibler is a candidate for the Master of Science in Mechanical Engineering at North Carolina Agricultural and Technical State University in Greensboro, North Carolina.

Dedication

This thesis is dedicated to all of my family and friends, and my nephew Byron L. Jefferson II. Thank you all for your support; love you all.

Acknowledgments

First and foremost I thank God for all of the blessings that he has bestowed upon me; with Him, all things are possible. I would like to thank my friends and family who have stood by and supported me throughout life and my educational career. I would like to express my appreciation and gratitude to Dr. John P. Kizito; thank you advising me throughout my years as a graduate. I would also like to thank all of the graduate researchers that are part of Dr. John P. Kizito's Astronautics and Thermofluids Lab for their assistance and support throughout my graduate experience. Lastly, I would like to thank the NASA University Research Center (funding grant #NNX09AV08A), NASA Center of Aviation Safety, the National Space Grant College Fellowship Program, and the North Carolina Space Grant Consortium.

Table of Contents

List of Figures

List of Tables

Abstract

Icing is widely recognized as one of the most dangerous, and potentially fatal, weather hazards in aircraft operations. Ice accretion on lifting surfaces is known to increase flow separation and drag, decrease lift, alter the moment and pitch of an aircraft, and cause undesired vibrations throughout the aircraft structure, all of which can lead to loss of control of an aircraft and accidents. It is for these reasons that developing methods to deter ice adhesion to aircraft structures is important to the aircraft operations. The average adhesive strength of ice on aluminum at -5, -10, -20, and -30°C, was measured to be 0.215±0.031, 0.184±0.031, 0.213±0.041, and 0.202±0.035 MPa respectively, suggesting that temperature does not affect on the adhesive strength of ice. The adhesive strength of ice was then measured on bare and methoxymethylethoxypropanol, polymethylhydrosiloxane, and octylphenol ethoxylate treated aluminum, stainless steel, copper, and polycarbonate substrates at -10°C. None of the surfactants used in the present study were found to be truly ice-phobic. Wettability was measured on the surfaces of all substrates used. The octylphenol ethoxylate, a surfactant that caused all of the materials observed in the present study to exhibit superhydrophilic surface properties, was revealed to be the only surfactant to reduce the adhesive strength of ice on all of the substrates. At -40°C the volumetric freeze rate of a sessile droplet was measured to be 4.62 mm^3/second, and the duration of the entire freezing process of a sessile droplet was 10.67 seconds.

CHAPTER 1

Introduction

Icing is widely recognized as one of the most dangerous, and potentially fatal, weather hazards in aircraft operations. Icing can occur while an aircraft is in-flight or on the ground, causing increases in drag, decreases in lift, changes in the aircrafts pitch and moment, turbulence, and undesired flow separation, all of which can ultimately lead to loss of control of an aircraft. Aircraft icing not only affects the aerodynamics of the aircraft, but also poses a threat to aircraft engines as well, having the potential to accrete on propeller and compressor blades, extinguish the flames in combustion chambers, and cause complete power loss. Throughout years of research in aircraft icing, anti-icing and de-icing techniques have been developed, each with its own benefits and drawbacks. No single anti-icing or de-icing technique has been proven to completely deter ice accretion without any disadvantages.

The primary goals of aircraft ice protection are to avoid, detect, and recover from any degradation of an aircraft caused by icing conditions and environments (Reehorst et al., 2010). The motivation of the present study is based on the need derived from the National Aeronautics and Space Administration (NASA), in an effort to contribute to aircraft ice protection and safety. The specific objectives of the present study are to determine:

- The adhesive strength of ice on various substrates at subcooled temperatures,
- The wettability of surfactant treated substrates,
- The freezing rate of sessile droplets using shadowgraphing techniques.

Chapter two entails a literature review of previous studies that have been conducted in the area of aircraft icing. Chapter two begins with a slight history on aircraft icing, followed by a more detailed section on the degradation of an aircraft caused by ice, and anti-icing and de-icing

techniques currently being researched. Chapter three describes the experimental setup and procedures done to fulfill the specific objectives of the present study. Chapter four describes the results of all of the experiments done as they pertain to the specific objectives. Finally, Chapter five concludes the present study based on the results presented in Chapter four, and suggests areas to be considered for further studies.

CHAPTER 2

Literature Review

2.1. History of Aircraft Icing

Aircraft icing has been a hazard that has plagued aircraft safety for decades. NASA has been conducting research efforts towards the detection and prevention of the occurrence and accumulation of icing on aircrafts, as well as the removal of ice from aircraft structures, since 1928 (Atchison & Bohn, 1981; Geer & Scott, 1930). In the 1950s, NASA's persistent research in aircraft icing helped lead to solutions in in-flight aircraft icing for large transport aircrafts, and in 1981 NASA initiated a new focus in their research: icing protection for small aircrafts and helicopters (Atchison & Bohn, 1981). The research in icing protection for small aircrafts and helicopters was due in-part to increases in the purchase of private planes, certification of private pilots, and the lack of de-icing and anti-icing capabilities available to helicopters. The increase in private pilots becoming certified came with an increase in pilots lacking the knowledge, experience, and skill necessary to operate an aircraft under icing conditions (Geer & Scott, 1930; Reehorst et al., 2010).

Figure 1 shows statistics of weather related accidents that were reported by the Aircraft Owners and Pilots Association between 1990 and 2000 (Landsburg, 2008). Between 1990 and 2000 there were reportedly 3,230 weather related aircraft accidents, 105 of which involved fatalities. Of the 3,230 accidents, 388 accidents were due to icing, and of the 388 icing related accidents, 203 accidents were due to ice induction into the aircraft propulsion system during flight, 153 accidents were due to structural icing during flight, and 32 accidents were due to the accumulation of ice on the aircraft while on the ground. The pilot time represents ranges, in minutes, at which aircraft were piloted before the icing related accidents occurred. Most of the

icing related aircraft accidents (48%) occurred during flights greater than 1000 minutes, while the least amount of icing related aircraft accidents (7%) occurred during flights less than 100 minutes. In regards to the landing gears associated with the aircraft, a majority of the icing related accidents occurred amongst fixed gear aircrafts, as opposed to multi-gear and single retractable gear aircraft.

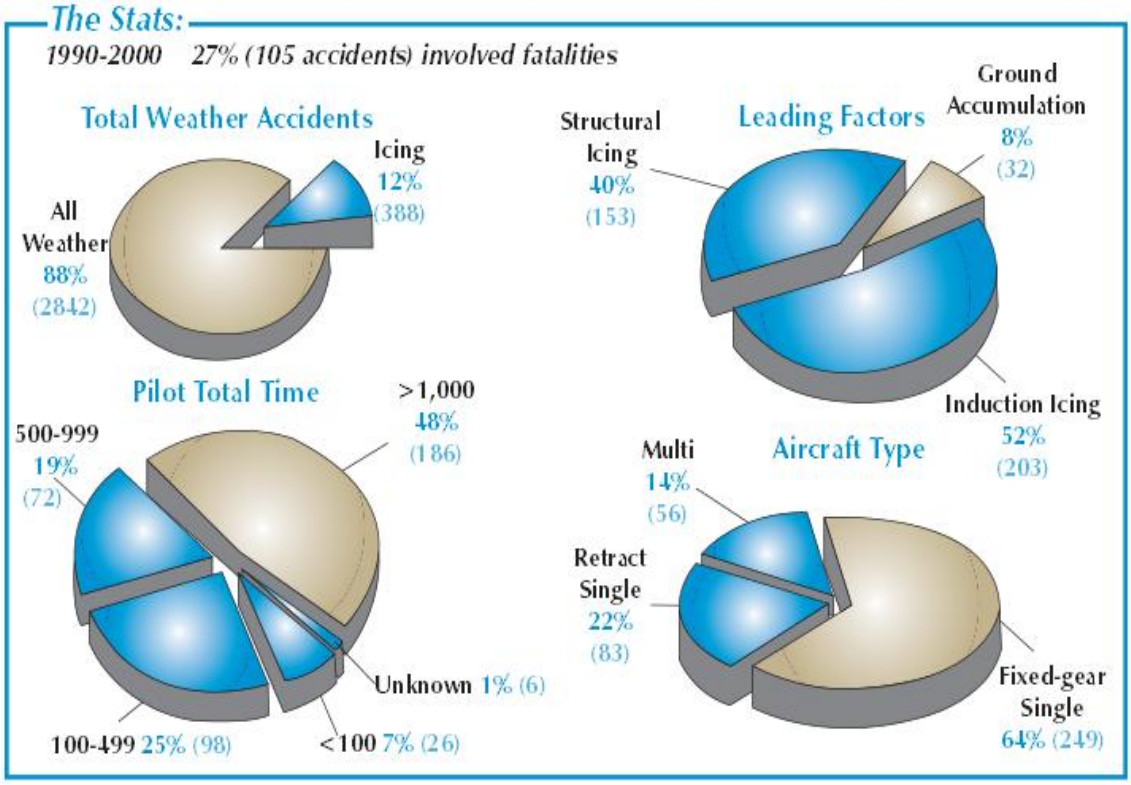

Figure 1. Weather related accidents that were reported by the Aircraft Owners and Pilots Association between 1990 and 2000.

Today, aircraft icing for small aircraft and helicopters is still existent, however, anti-icing and de-icing techniques have improved compared to those used in 1981. One of the most recent accounts of an icing related aircraft incident occurred in December of 2011 (Flegenheimer, 2011). A Tocata TBM-700 single engine aircraft traveling from Teterboro, NJ to Atlanta, GA became undetectable by radar after reaching an altitude of 17,500 feet, crashing 14 minutes after

takeoff, claiming the lives of all of its passengers. Later reports claimed the accident was caused by ice that accrued on the right wing of the aircraft, which led to the wing separating from the aircraft during flight, and severing the empennage of the aircraft (Hicks, 2013a, 2013b). The temperature that day was 6°C at ground level, however, at altitudes between 15,000 and 17,500 moderated icing conditions were present (Hicks, 2013b).

2.2. Ice Formation on Aircraft Propulsion Systems and Lifting Surfaces

Icing can accumulate on aircrafts in the forms of: rime ice, glaze ice, or a mixture of both rime and glaze ice (Atchison & Bohn, 1981; Geer & Scott, 1930; Korkan et al., 1983; NASA, 2013b; Thomas et al., 1996). Rime ice is observed when supercooled droplets come into contact with a surface and essentially freezes on contact. Rime ice can be characterized by its white appearance, which is due to air being entrapped within the supercooled droplets during the freezing process. Glaze ice is observed when cooled droplets come into contact with a surface and are allowed to runback along the surface, leaving a thin film of liquid water that eventually solidifies into ice. Since glaze ice is allowed to run back there is not much air entrapped within the droplets undergoing the glazing process, thus it appears transparent, as opposed to white. Lastly, the mixture of both glaze and rime icing is observed when a single ice formation displays characteristics of both glaze and rime formations. Thomas, Cassoni, et. al. (1996) described the mixture formation as "glaze ice surrounded by delicate feather-shaped rime ice formations."

Icing can occur while an aircraft is in-flight, and on the ground. The type and shape of the ice formations are dependent on a variety of parameters such as: airfoil geometry, airspeed, altitude, liquid water content within clouds, frequency of droplet impingement, ambient air temperature, etc. (Hallett & Isaac, 2008; Thomas et al., 1996) The temperature range normally associated with aircraft icing is from -40°C to 0°C (Geer & Scott, 1930; Hallett & Isaac, 2008;

Thomas et al., 1996). Thomas et al. (1996) reported that rime ice is observed at temperatures ranging from -40°C to -10°C, glaze ice is observed from -18°C to 0°C, and mixed icing can occur anywhere within those temperature ranges.

On the ground, precipitation at freezing temperatures can fall onto an aircraft and adhere to the surfaces of the aircraft in the form of snow, slush, ice, or a mixture of the three (NASA, 2013a; Thomas et al., 1996). Freezing on the ground can not only be due to ambient temperatures below freezing, but the presence of fuel that has been cooled below freezing in the fuel tanks, as was the case in an accident involving a McDonnell Douglas MD-81 according to the Swedish board of accident investigations (Sparaco, 1994).

Ice is generally formed by means of nucleation. Nucleation is a phase transformation where at least one new phase is formed that is composed of different physical and chemical characteristics and/or a different structure than that of the parent phase. The process generally begins with the formation of numerous particles of the new phase(s), referred to as nuclei, which increase in size until the transformation has fully developed (Callister, 2005). There are two types of nucleation processes: homogeneous nucleation and heterogeneous nucleation. Homogenous nucleation occurs when the nuclei of the new phase are allowed to form throughout the original phase without the presence of a distinguishable nucleation site. During heterogeneous nucleation nuclei form at structural inhomogeneities, therefore, the presence of a surface possessing potential nucleation sites is required for heterogeneous nucleation to occur (Callister, 2005).

2.2.1. Heterogeneous and homogeneous nucleation processes. Nucleation involves a thermodynamic parameter referred to as Gibbs free energy, *G*. Gibbs free energy is a function of enthalpy and entropy, which describe the internal energy of a system, and the randomness of

atoms and molecules, respectively. The change in free energy, ΔG, indicates the occurrence of phase transformation. Phase transformation will occur spontaneously if ΔG is a negative value (Callister, 2005; Ohring, 2002).

Figure 2 is a schematic plot of the free energy with respect to the radius of the developing embryo or nucleus. The parameter ΔG is influenced by the difference in volume free energy between the liquid and solid phases, ΔG_v, and the interfacial energy due to the formation of the solid-liquid phase boundary during the solidification transformation (Callister, 2005). The interfacial energy corresponds with surface energy, γ, of the developing solid-liquid phase boundary. As solid particles begin to cluster together, the free energy increases until the cluster reaches a critical radius, r^*, at which point growth will continue as free energy decreases.

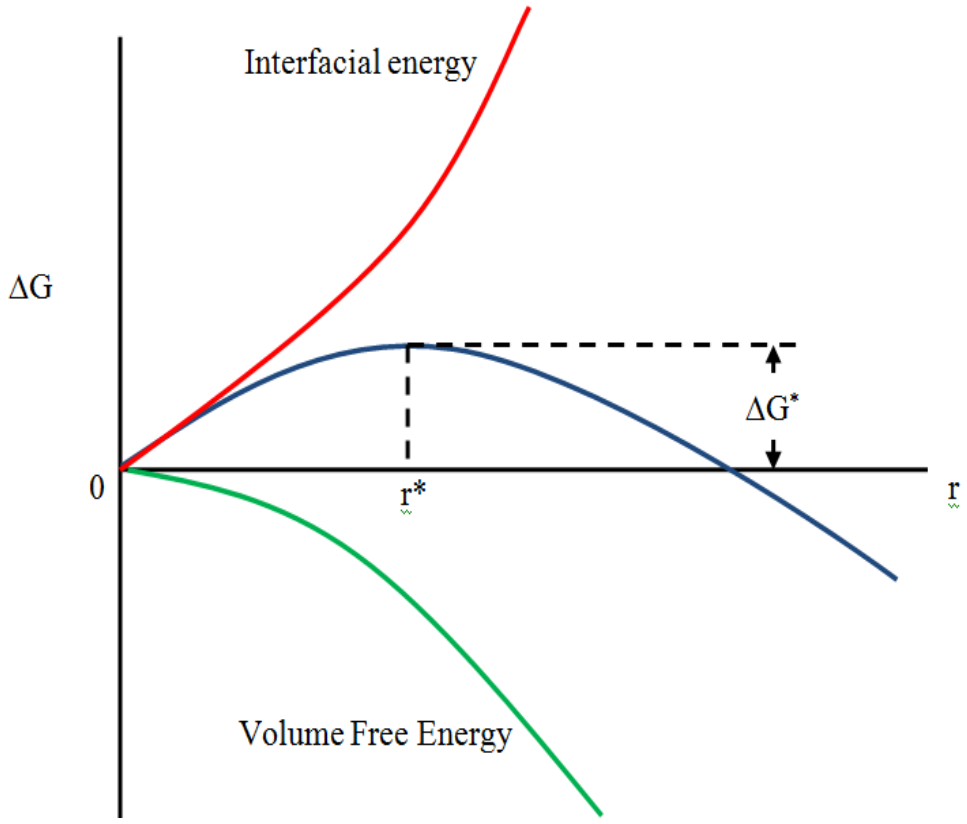

Figure 2. Schematic of the free energy with respect to the radius of the developing nucleus.

The magnitude of the contribution of the surface energy is dependent on the surface area of the nucleus. The magnitude of the contribution of ΔG_v is dependent on the volume of the nucleus. Thus, the total free energy is given by

$$\Delta G = \frac{4}{3}\pi r^3 \Delta G_v + 4\pi r^2 \gamma \tag{2.1}$$

where r is the radius of a nucleus. The parameter ΔG_v can be expressed as

$$\Delta G_v = \frac{\Delta H_f (T_m - T)}{T_m} \tag{2.2}$$

where ΔH_f is the latent heat of fusion, T_m is the equilibrium solidification temperature, and T is temperature. From Equation 2.2 it is shown that ΔG_v is a function of temperature.

Clusters are regarded as "embryo" if the clusters formed cannot achieve a radius greater than the critical radius, r^*. Embryos typically shrink and dissolve since they are incapable of undergoing the nucleation process. However, if the cluster can achieve a radius greater than r^*, then the cluster is regarded as a nucleus, and nucleation and growth will occur. The critical free energy, ΔG^*, represents the energy required to form a stable nucleus. The critical free energy corresponds with the activation free energy. The parameter r^* can be obtained by differentiating Equation 2.1 with respect to r and applying the condition $r = r^*$ (Callister, 2005). The parameter ΔG^* can be obtained by substituting the expression for r^* into Equation 2.1. The parameters r^* and ΔG^* differ when considering the type of nucleation that is occurring. When considering a homogeneous nucleation process, r^* and ΔG^* is expressed as

$$r^*_{hom} = \left(-\frac{2\gamma T_m}{\Delta H_f}\right)\left(\frac{1}{T_m - T}\right) \tag{2.3}$$

and

$$\Delta G^*_{hom} = \left(\frac{16\pi\gamma^3 {T_m}^2}{3{\Delta H_f}^2}\right)\frac{1}{(T_m - T)^2}. \quad (2.4)$$

Considering a heterogeneous nucleation process, r^* and ΔG^* are represented by

$$r^*_{het} = \left(-\frac{2\gamma_{SL} T_m}{\Delta H_f}\right)\left(\frac{1}{T_m - T}\right) \quad (2.5)$$

and

$$\Delta G^*_{het} = \left(\frac{16\pi {\gamma_{SL}}^3 {T_m}^2}{3{\Delta H_f}^2}\right)\left(\frac{1}{(T_m - T)^2}\right) S(\theta) \quad (2.6)$$

where γ_{SL} is the surface free energy between the solid-liquid interface and $S(\theta)$ is a function of the contact angle.

Figure 3 shows a schematic of the change in free energy with respect to the radius of a nucleus and temperature. At lower temperatures nucleation more readily occurs, requiring a smaller critical radius and less activation energy compared to a nucleation process at higher temperatures (Callister, 2005; Chung et al., 2011; Ohring, 2002).

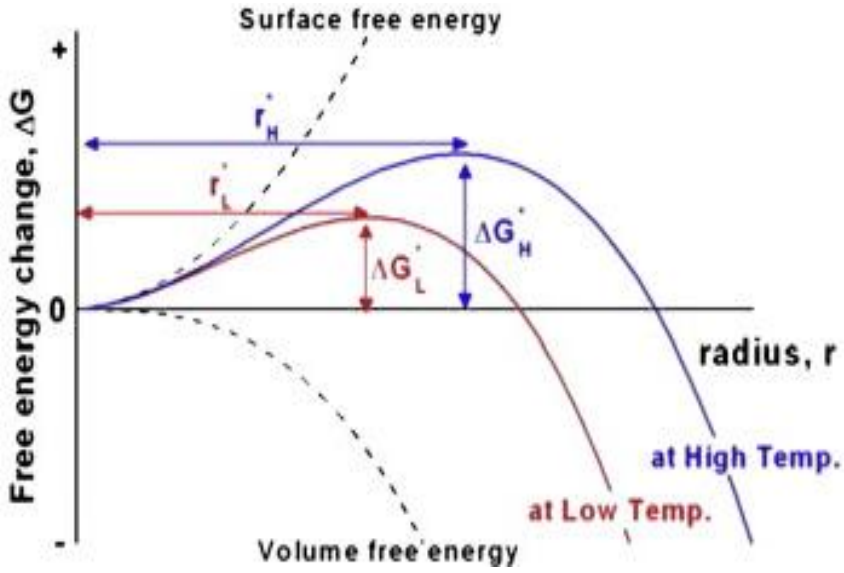

Figure 3. Schematic of change in free energy with respect to radius and temperature (Chung et al., 2011).

Figure 4 shows a schematic of the free energy versus the radius of a nucleus with respect to the acting nucleation process. Heterogeneous nucleation requires less free energy to achieve its critical radius compared to a homogeneous nucleation process. Therefore heterogeneous nucleation occurs more readily than homogeneous nucleation (Callister, 2005; Ohring, 2002; Qi et al., 2004).

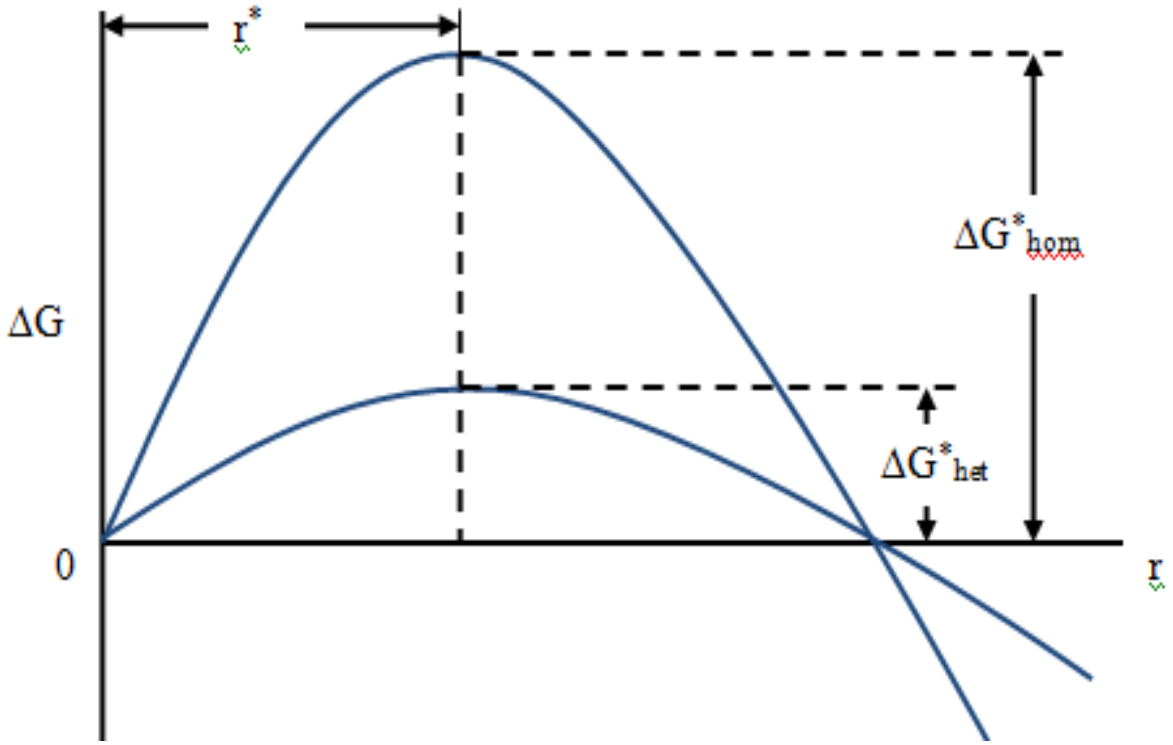

Figure 4. Schematic of the free energy versus the radius of a nucleus with respect to the acting nucleation process.

Icing on an aircraft is generally formed when water, in its liquid form, impinges on a surface in the presence of subcooled conditions, allowing for a heterogeneous nucleation process to occur. It should be noted that it is possible for water to remain in its liquid state at subcooled temperatures if a surface is not present (Freiberger & Lacks, 1961; Geer & Scott, 1930). Ice developing by means of heterogeneous nucleation can be formed the following ways:

- Supercooled water impinging on a surface (Jin & Hu, 2009; Miller et al., 2004; Sparaco, 1994; Thomas et al., 1996),
- Water impinging on a supercooled surface (Jin & Hu, 2010; Sparaco, 1994),
- Supercooled water impinging on a supercooled surface (D. N. Anderson & Reich, 1997; Freiberger & Lacks, 1961; Jin & Hu, 2010; Reich, 1994).

According to Hallett and Isaac (2008), aircrafts are typically certified to fly through clouds, however some clouds contain entirely supercooled liquid particles. These clouds are referred to as glaciated and mixed phase clouds since these particular clouds contain both supercooled water and ice particles. The ambient temperature within glaciated and mixed phase clouds has been reported to reach temperatures as low as -40°C.

Clouds are known to possess electrical charges, which can influence the charge of particles within the clouds (Fletcher, 2013; Pähtz et al., 2010). Farzaneh (2000) reviewed the effects of atmospheric ice deposits on high-voltage conductors and concluded that the amount and density of ice deposits decrease with an increase in the electric field at the surface of conductors due to the electrical charge of water droplets, the mode of corona discharge, and the presence of ionic winds.

Figure 5 shows the phosphorescence images and lifetime-based molecular tagging thermometry (MTT) of the icing process of a small liquid water droplet impinging on a plate at -2°C (Jin & Hu, 2010). The bottom of the droplet in direct contact with the cooled surface immediately solidified after the liquid droplet impinged onto the cooled surface of the substrate, while the remainder of the droplet remained liquid. As time progressed, freezing throughout the droplet progressed rapidly until the droplet was completely solid at 35 seconds.

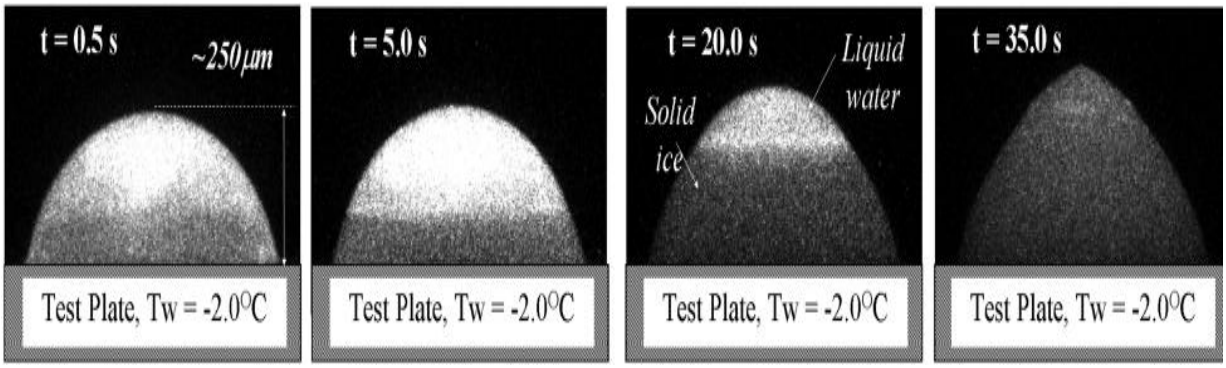

(a)

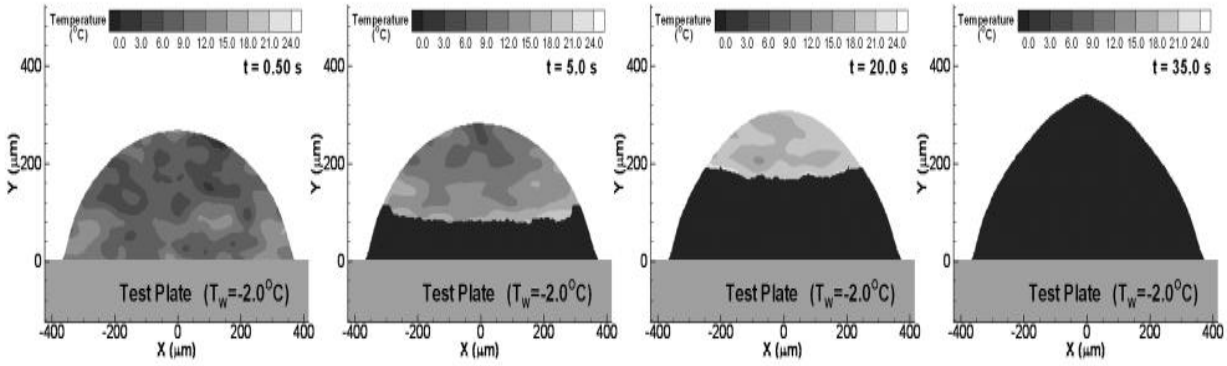

(b)

Figure 5. (a) Phosphorescence images and (b) Lifetime-based MTT results of the phase changing process within a freezing water droplet (Jin & Hu, 2010).

Figure 6 is a plot of the temperature of the liquid content remaining in the sessile droplet shown in Figure 5 with respect to time. Jin and Hu (2010) observed that as the freezing process progressed throughout the droplet, the average temperature of the remainder of the droplet that was liquid was reported to have increased, which can be seen in Figure 6. In Figure 6, the temperature of the droplet appeared to have risen in a nearly linear fashion with respect to time. Initially, the droplet impinged onto the cooled surface at 8°C, and during the nucleation process before, the temperature of the remainder of the liquid content in the droplet was reported to have risen in the remaining liquid content to 26°C. Jin and Hu (2010) concluded that the results could

have been due to the release of heat from the freezing portion of the droplet during the solidification process.

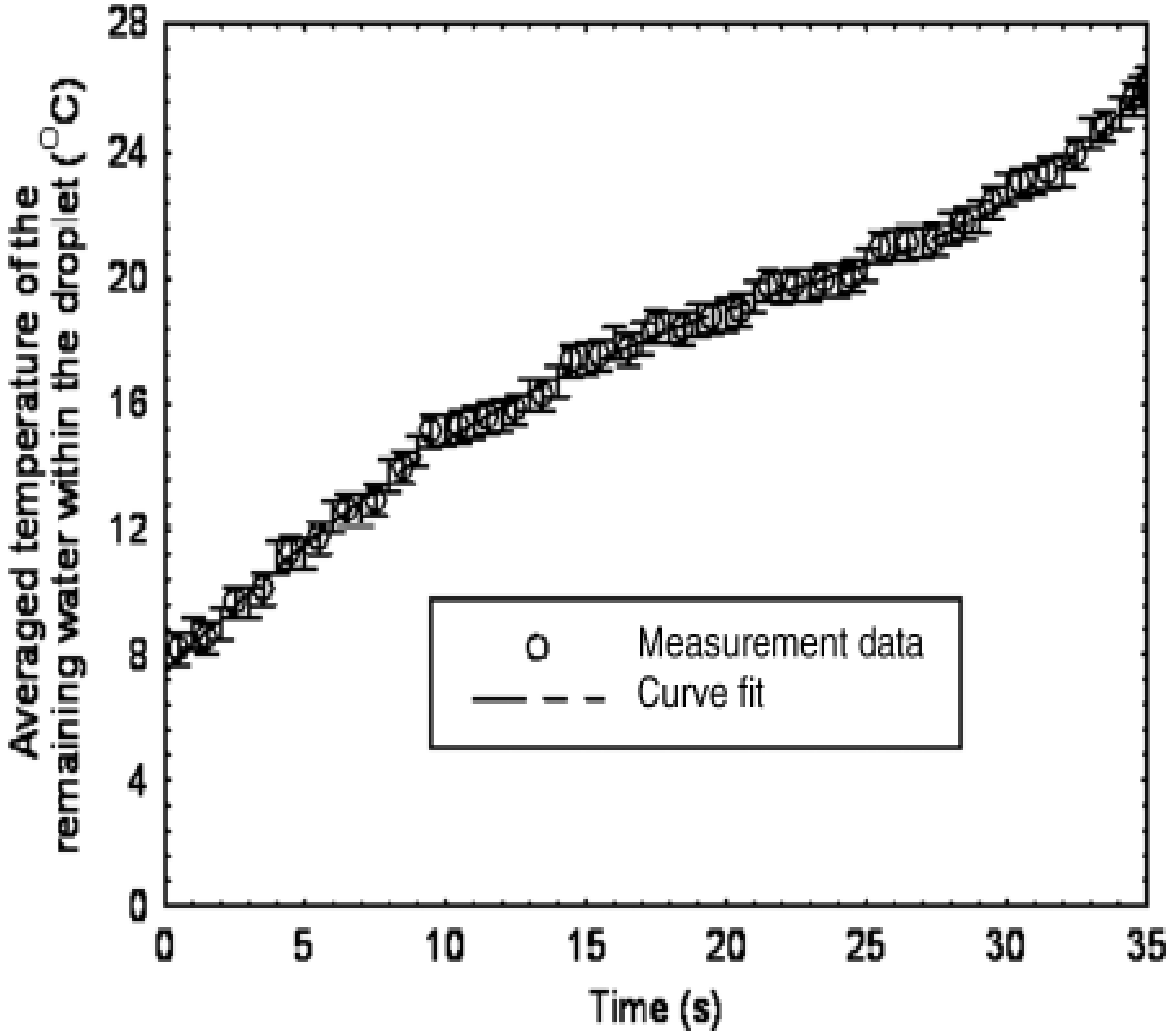

Figure 6. The average temperature of the remaining liquid in the freezing droplet with respect to time (Jin & Hu, 2010).

2.2.2. Performance degradation on lifting surfaces due to icing. Ice accretion on an aircraft is an extremely dangerous hazard that has claimed the lives of many throughout the years of aircraft travel (Jin & Hu, 2010; Landsburg, 2008). Once ice has adhered to an aircraft structure, ice has been known to accrete in the form of rime ice, glaze ice, or a mixture of rime

and glaze ice. According to Thomas et al. (1996), the most critical locations where ice accretes on aircraft vehicles are the leading edges of wings, propellers, and windshields.

Figure 7 shows a comparison of airflow around a clean airfoil and an airfoil with ice adhered to its leading edge (NASA, 2013b). As ice forms on an airfoil, there are increases in flow separation, drag, decreases in lift, the moment and pitch of an aircraft become altered, and undesired vibrations throughout the aircraft structure are produced, all of which can potentially lead to loss of control of the aircraft (Landsburg, 2008; Scavuzzo et al., 1994; Thomas et al., 1996). Ice accumulation on an aircraft structure can also lead to the failure of the components of an aircraft important to maintaining the aircrafts capability of flight. The adhesion of ice on an aircraft structure can occur during flight and on the ground.

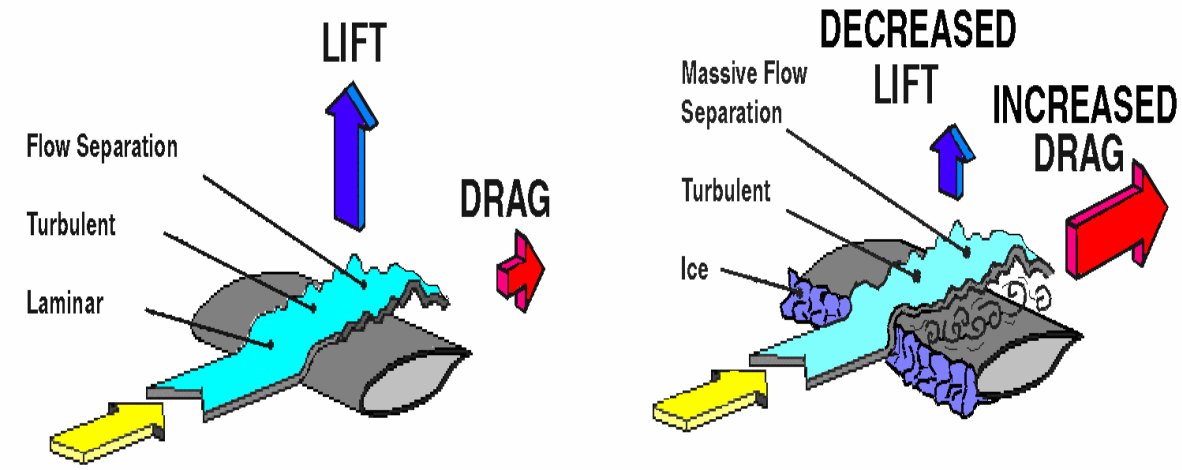

(a) (b)

Figure 7. Comparison of airflow around (a) a clean airfoil and (b) an airfoil with ice adhered to its leading edge (NASA, 2013b).

Figure 8 compares the lift coefficient of a clean airfoil and an airfoil with ice adhered to its leading edge with respect to angle of attack (NASA, 2013b). The coefficient of lift of the clean airfoil and the airfoil with ice adhered to its leading edge remained similar until the airfoils

reached an angle of attack of approximately 5°. Beyond 5°, the coefficient of lift between the two airfoils noticeably differs. Both airfoils continued to increase in coefficient of lift, however, the coefficient of lift of the clean airfoil increased with a greater slope than that of the airfoil with ice along its leading edge. The airfoil with ice along its leading edge stalls and the airfoil is no longer capable of generating lift after reaching an angle of attack of 7.5°.

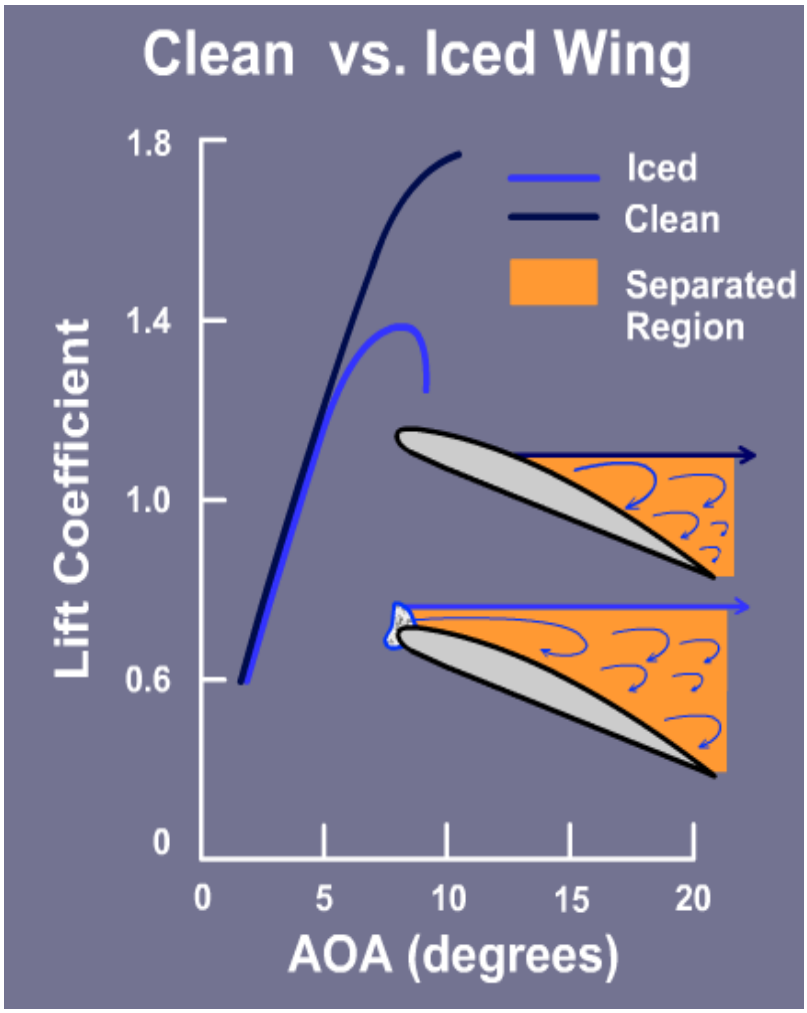

Figure 8. Lift coefficient of a clean airfoil and an airfoil with ice adhered to its leading edge with respect to angle of attack.

Stalling is due to the airfoil with ice along its leading edge having a greater region of flow separation than the clean airfoil. Flow separation can cause the flow of air around an airfoil

to be altered from laminar flow to turbulent flow, deterring the generation of lift of an airfoil. The free stream airflow around an airfoil generates pressure around an airfoil. As air flows towards the trailing edge of an airfoil, the pressure gradually increases until it reaches values slightly above the free stream pressure. The region in which the pressure increases is referred to as the adverse pressure gradient (J. D. Anderson, 2007). Typically, at relatively high angles of attack, airfoils generate adverse pressure gradients beyond their design capabilities and in turn flow separation occurs. Ice accretion on an airfoil causes flow separation to occur prematurely, causing airflow to detach from the once aerodynamic profile of an airfoil.

On the ground, when an aircraft is introduced to hazards such as ice, snow, or slush, the aircraft can become potentially dangerous. Usually while on the ground, during precipitation and temperatures below freezing, aircrafts are treated with an alcohol based de-icing solution, however, the solution is not promised to last throughout the entire duration of the aircraft being grounded (Due et al., 1996).

Figure 9 depicts a schematic of the initial stages of flight to aid as a visual in explaining the hazards involved with ground icing (FAA, 2013). In order to achieve flight, aircraft must travel a length known as the "takeoff distance". The pilot generally travels the takeoff distance at a velocity which is best to achieve climb given the environmental condition such as temperature, wind speed, and wind direction (J. D. Anderson, 2007). While traveling along the takeoff distance at a velocity air is allowed to flow around the wings of the aircraft, generating lift, and contributing to the aircraft achieving the climb. The pilot of the aircraft will continue to climb until reaching the desired altitude for cruising. Ice, snow, and slush can contribute to longer takeoff distances, failure of the aircraft to achieve lift-off, engine power loss or failure, pitch and roll instability during the climb, and the inability to climb during lift-off (NASA,

2013a). The inabilities to climb during lift-off, longer takeoff distances, and pitch and roll instability during the climb are all consequently due to turbulent flow around an airfoil.

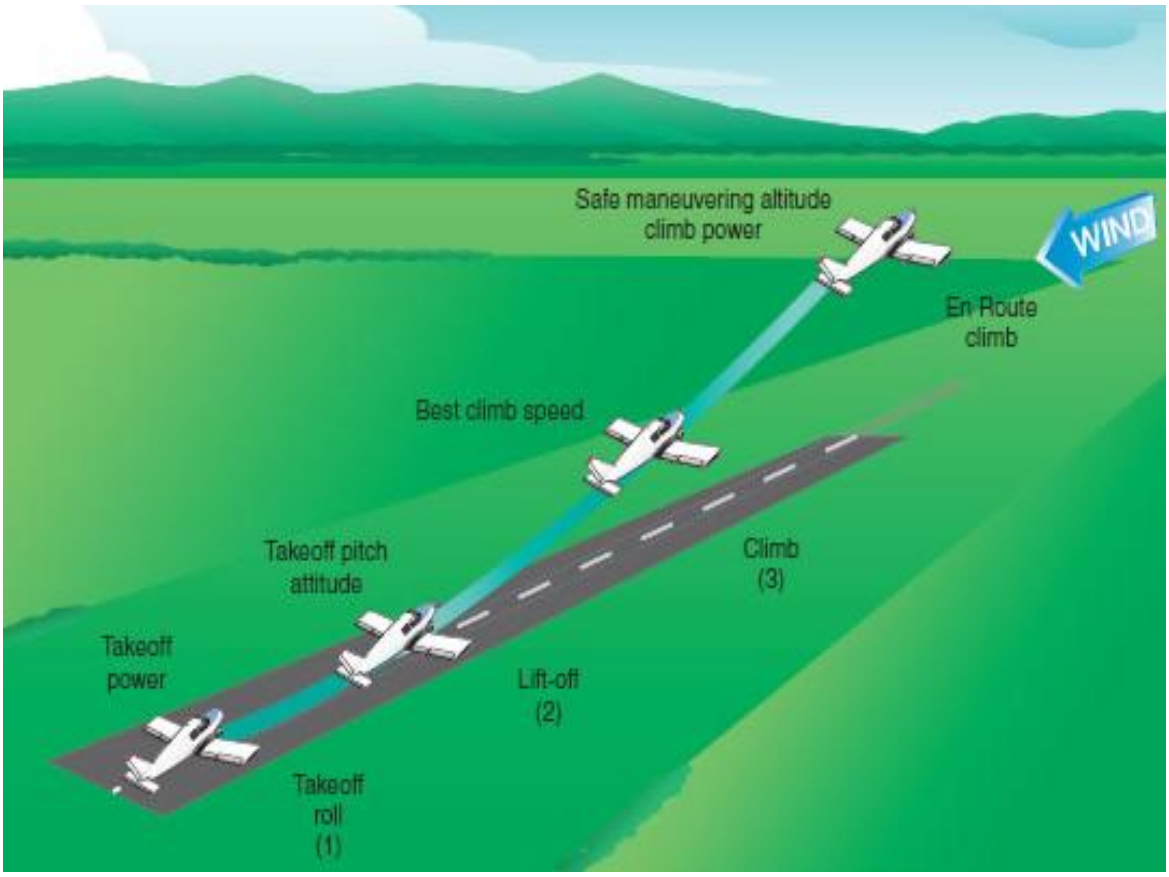

Figure 9. Schematic of the initial stages of flight.

2.2.3. Performance degradation on propulsion systems due to icing. In regards to the aircraft engine, ice can accrete on the aircraft propeller and compressor blades, causing undesired vibrations among the blades, which can lead to failure and ingestion of the blades into the aircraft propulsion system, resulting in internal damage of the aircraft (Mason et al., 2006; Scavuzzo & Chu, 1987). Constant ingestion of supercooled droplets into an aircraft engine at a relatively high frequency can extinguish the flame in the combustion chamber, causing "roll back". "Roll back" is a term used to describe an aircraft engine that has become irresponsive to

any changes in thrust attempting to be made by the pilot, and loss of power (Mason et al., 2006; Reehorst et al., 2010; Shastri et al., 1994).

Numerous simulations and predictor codes have been created in an effort to predict the characteristics and end result of the complete formation of icing once it has began to adhere to aircraft lifting surfaces. In addition to simulations and numerical predictor codes that attempt to predict the formation of icing along aircraft structures, simulations and numerical predictor codes have also been written to predict the magnitude of degradation that can occur based on ice structures that have formed on airfoils. Extended information on the topic of simulations and numerical predictor codes as they relate to ice formations and degradation on aircraft structures due to icing is discussed in greater detail by Scavuzzo, Chu, Woods, et al. (1990), Scavuzzo, Chu, and Kellacky (1990), Scavuzzo et al. (1994), Scavuzzo and Chu (1987), Harireche et al. (2008), Labeas et al. (2006), and Thomas et al. (1996).

2.3. Anti-Icing and De-Icing Techniques

The primary goals of aircraft safety are to avoid, detect, and recover from any degradation on an aircraft caused by icing conditions and environments (NASA, 2013b; Reehorst et al., 2010). While detecting and recovering are both important in their own respects, the present study will focus more towards avoiding any degradation on an aircraft caused by icing conditions and environments. If aircraft icing can be avoided, then there will little, to no need, to detect or recover from any degradation on an aircraft caused by icing.

De-icing techniques are often used to remove ice formations after they have adhered to a surface, while anti-icing techniques are used to prevent ice from adhering from a surface. Anti-icing techniques are used to avoid aircraft icing and de-icing techniques are used to recover from degradation caused by ice accretion (Thomas et al., 1996). There are three types of anti-icing

and de-icing techniques: chemical surfactants, mechanical systems, and thermal heating, each with its own individual benefits and limitations (Geer & Scott, 1930; Scavuzzo & Chu, 1987; Thomas et al., 1996).

2.3.1. Chemical surfactants. Chemical surfactants are used on aircrafts in the form of surface treatments. These surface treatments directly affect the surface energy during contact between the liquid droplets and the surface itself, resulting in surface properties capable of generating hydrophilic and hydrophobic effects on droplets. A surface is considered to have hydrophilic properties if it contributes to a liquid droplet wetting a surface, causing the liquid droplet to display a contact angles below 90°. In contrast, hydrophobic surfaces repel liquid droplets, causing the liquid droplets to display contacts angles greater than 90°. Surface energy and the possible surface properties are explained in greater detail in Chapter 2.5.

The level of performance of a surfactant and whether the surfactant is capable of achieving a desired objective depends on a variety of factors, such as the chemical compound of the surfactant, environmental conditions which the surfactant is used, and even the rate at which the surfactant is exposed to a given environmental condition. Using a combination of siloxane(s), ethyl alcohol, ethyl sulfate, isopropyl alcohol, and fine-particle polytetrafluoroethylene, NASA developed a hydrophobic coating, referred to as the Shuttle Ice Liberation Coating, which they claim can reduce the adhesion of ice by as much as 90 percent when compared to corresponding bare surfaces (Smith et al., 2008). Reich (1994) suggests that chemicals possessing levels of silicone, such as siloxane, contribute to low adhesive strength in the bond between icing and various materials used on aircraft.

Sakaue et al. (2008) developed a micelle polymer comprised of poly(N-isopropylacrylamide) demonstrating that it is possible to utilize hydrophobic and hydrophilic

coatings in a strategic manner and control how droplets interact with surfaces. Figure 10 depicts a schematic of the micelle polymer and how the micelle polymer reacts to changes in temperature. The micelle polymer features a reversible formation in its chemical makeup that allows for the polymer to exhibit hydrophilic and hydrophobic properties with respect to temperature.

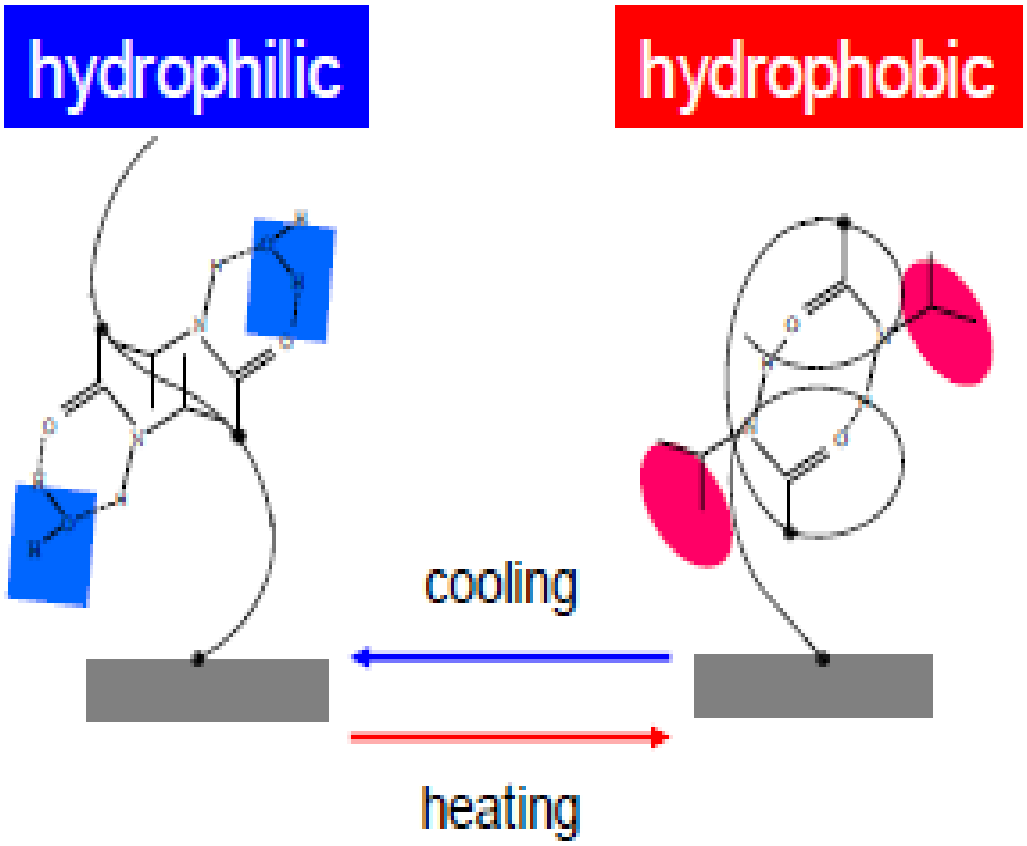

Figure 10. Schematic of the how the micelle polymer interacts to changes in temperature (Sakaue et al., 2008).

Figure 11 shows images of a liquid droplet interacting with an aluminum plate treated with the micelle polymer. As temperature increased the micelle polymer treated aluminum displayed hydrophobic surface properties and as temperature decreased, the micelle polymer treated aluminum exhibited hydrophilic properties.

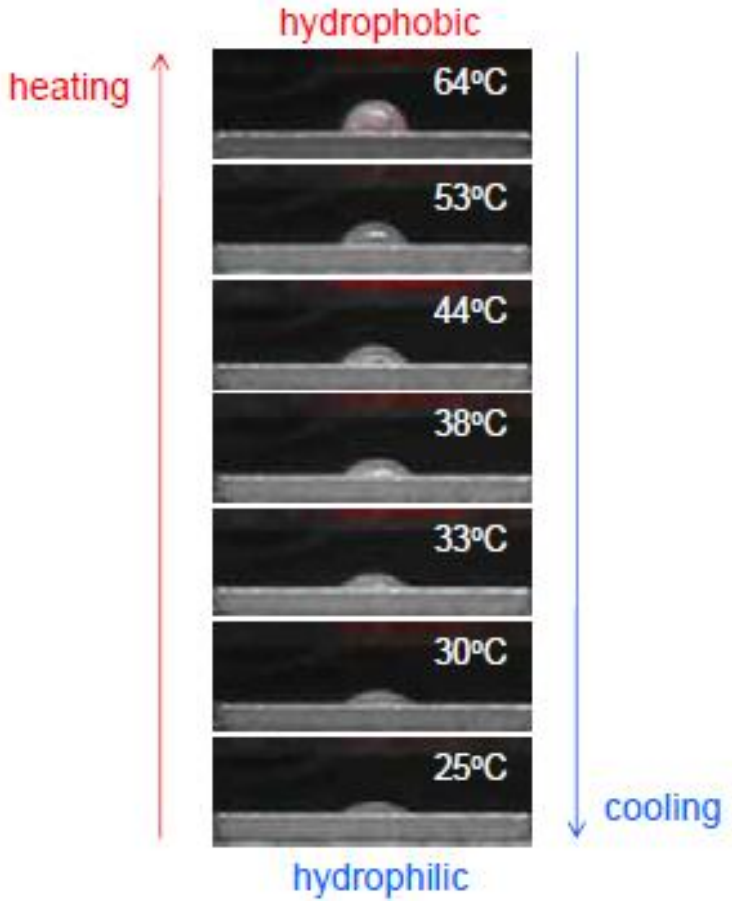

Figure 11. Images of a liquid droplet interacting with an aluminum plate treated with the micelle polymer (Sakaue et al., 2008).

Limitations develop in surface treatments when the repetitive cycle of applying and removing ice or water is present, causing treatments to eventually lose their affect (Scavuzzo & Chu, 1987). Figure 12 shows results of ice removal tests using elastic ceramic coatings and an ice-phobic Du Pont coating (D. N. Anderson & Reich, 1997). The adhesive strength necessary to cause debonding between the ice and substrates increase the number of ice removals increased. According to Due et al. (1996), the repeated action of removing ice from a surface coated with a surfactant, forms craters in the coatings, creating local areas where the film thickness is dramatically reduced, leading to premature failure of the film. Cratering was found

to be driven by surface tension gradients at the surface of coatings that cause surface movement and removal of the underlying coating.

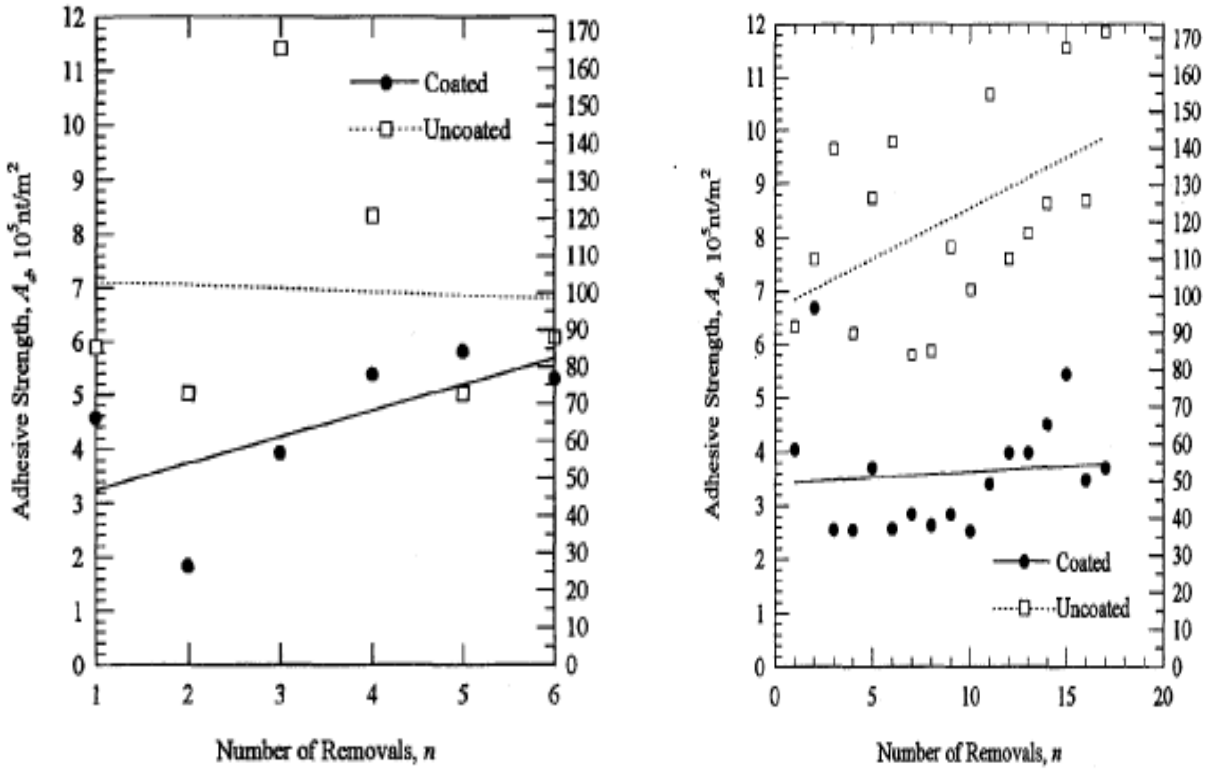

Figure 12. Results of ice removal tests using (a) an elastic ceramic coating and (b) an ice-phobic Du Pont coating.

Another factor that affects the efficiency of a chemical surfactant is the rate at which precipitation impinges on a surface treatment. Figure 13 shows results from a test comparing failure time of a glycol based freezing depressant to the average precipitation rate of ice (Due et al., 1996). The failure time of a surfactant decreases as the rate of precipitation increases. Depreciation of a surfactant is not limited to the repeated removal of ice however; water has also been reported to depreciate the effectiveness of surfactants. According to Reich (1994), rain erosion is a more severe process which not only destructs coatings, but at higher velocity and

time, possesses the capabilities of eroding the substrate. The ideal chemical surfactants, in regards to aircraft icing, must serve as an ice-phobic coating which can not only prevent ice from adhering to the surface of an aircraft, but can also withstand rain erosion (Reich, 1994).

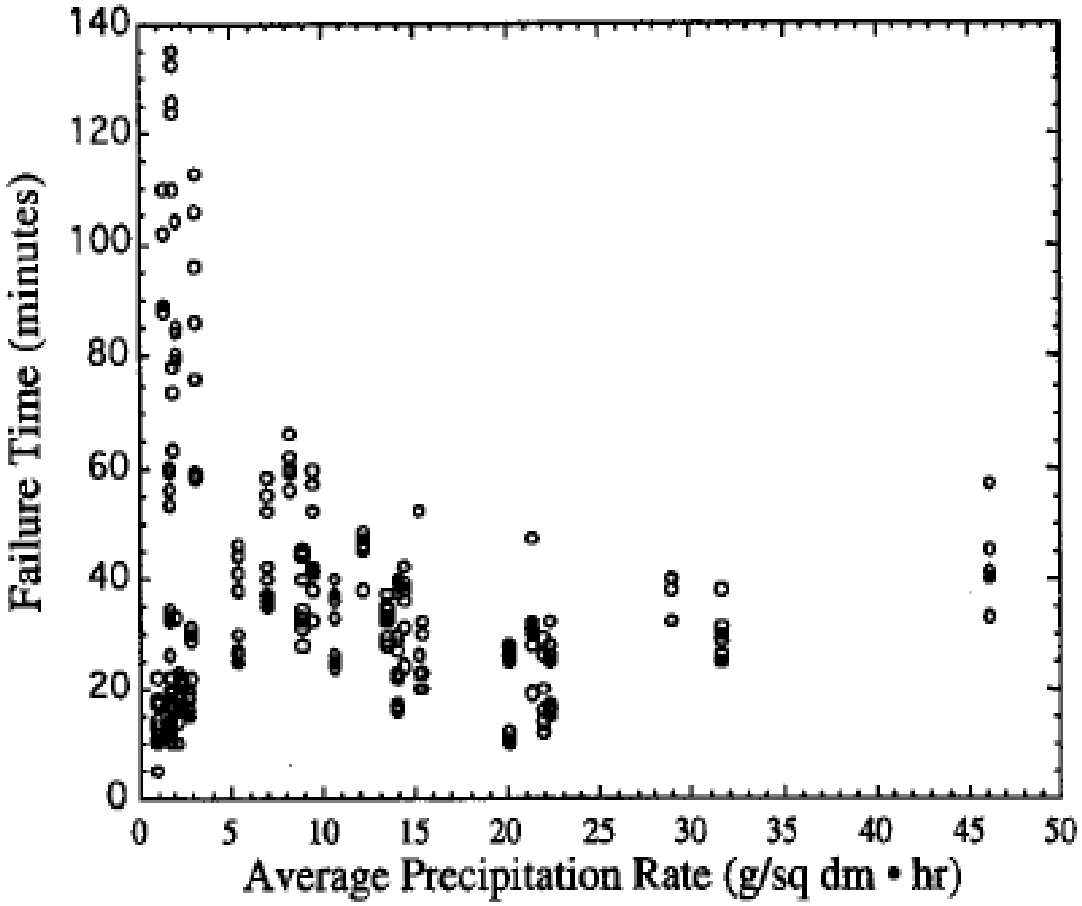

Figure 13. Results from a test comparing failure time of a glycol based freezing depressant to the average precipitation rate of ice (Due et al., 1996).

2.3.2. Mechanical systems. De-icing techniques that require a power source to cause a surface to become modified or deformed from its original shape is considered a mechanical system (Thomas et al., 1996). The goal of mechanical systems is to modify an iced surface in a manner that initiates cracking within the ice formation and cause debonding between the ice formation and the surface of the aircraft, allowing for the aerodynamic forces acting on the

aircraft to carry away the fractured ice. The three notable types of mechanical systems that have been researched are: pneumatic boots, electromagnetic impulse, and electromagnetic expulsive boots (Labeas et al., 2006; Scavuzzo, Chu, Woods, et al., 1990; Thomas et al., 1996; Venna et al., 2007). Figure 14 is a schematic of a pneumatic boot used on commercial aircrafts. When deactivated, the aircraft airfoil simply appears as a relatively normal airfoil, but when the pneumatic boot is activated, the rubber boots equipped onto the airfoil inflate, deforming the airfoil.

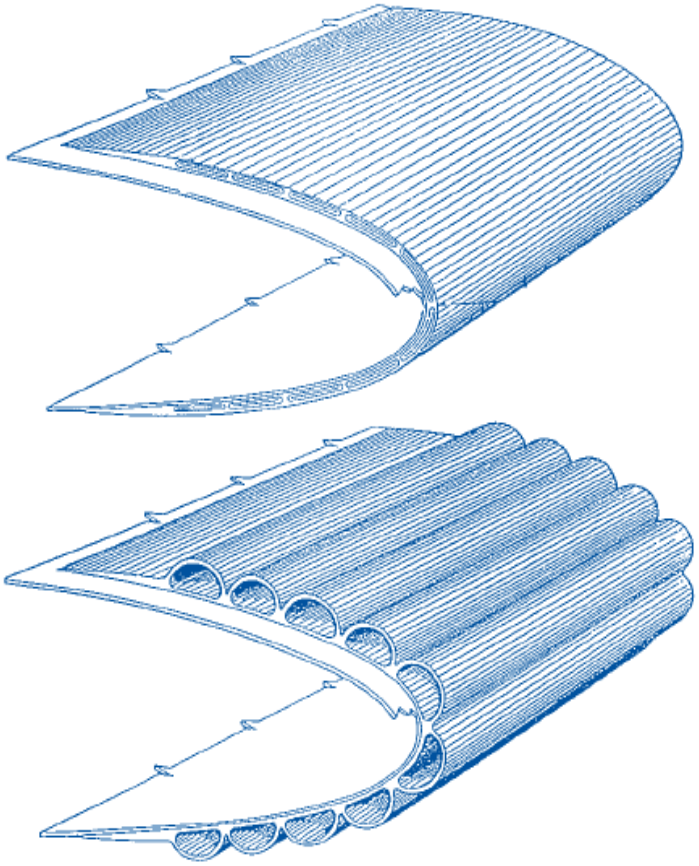

Figure 14. Schematic of a pneumatic boot used on commercial aircrafts.

Mechanical systems are strictly a de-icing technique, thus before the use of a mechanical system can be utilized to its full potential, a particular amount of ice must adhere and accrete to an aircraft structure (Landsburg, 2008; Thomas et al., 1996). The allowance of ice to accrete to

the aircraft structure invites an increase in drag to the aircraft. Mechanical systems require a power source, which is typically the aircraft battery. Some mechanical system power requirements are more demanding than others, which can be more straining on the aircraft battery. An even bigger issue arises when an aircraft equipped with mechanical systems is presented with relatively high rates of icing (Thomas et al., 1996). High rates of icing may require that a mechanical system operate continuously throughout flight which can lead to failure of the mechanical system (Venna et al., 2007). In addition to the power consumption needed to operate mechanical systems, some mechanical systems are physically heavy and add additional weight to the aircraft (Venna et al., 2007).

2.3.3. Thermal heating. Thermal heating is the heating of the exterior of an aircraft by means of either a power source, or redirecting heat generated from the aircraft engine (Thomas et al., 1996). The heat generated by either heat source serves as both an anti-icing and de-icing technique. Ice present on the aircraft structure prior to activating the thermal heating will melt, and ice that impinges on a thermally heated surface will melt on contact. Miller, Lynch, and Tate (2004) observed ice particles impinging on a thermally protected surface and concluded that some particles bounced off of the heated surface, while others melted onto the heated surface creating pools of cooled liquid. The supercooled liquid pools proceeded to freeze with the impingement of subsequent ice particles. Miller, Lynch, and Tate (2004) also observed ice particles cooled to -12.2°C impact on hotwire water content sensors, which also resulted in bouncing of the ice particles and the creation of pools of cooled liquid.

Heat must be applied along the entire aircraft structure for thermal heating to work well in a cooled environment; else precipitation can melt, runback due to aerodynamic forces, and refreeze at sections of the aircraft that lack proper heating (Geer & Scott, 1930). The rate at

which precipitation impingement occurs is a factor that determines the efficiency of thermal heating. At relatively high impingement rates, thermal heating sources can be cooled, causing the thermal heat sources to lose their heating potential and can no longer contribute to preventing ice from forming (Miller et al., 2004). Thermal heating also contributes to the corrosion of the aircraft structure (Geer & Scott, 1930; Thomas et al., 1996). Corrosion of an aircraft structure can lead to the premature failure of the aircraft.

2.4. Shear Strength of Ice on Aircraft Structures

Numerous shear stress tests were conducted throughout literature, each in their own respective method, in effort to determine the shear strength necessary to cause debonding between ice and substrates used to simulate aircraft structures (D. N. Anderson & Reich, 1997; Fortin et al., 2010; Reich, 1994). Fortin et al. (2010) developed a centrifugal adhesion test in which a beam was connected to a motor and programmed to rotate while supercooled droplets impinged on its surface. Measuring the centrifugal force necessary to cause debonding between the beam and impinging supercooled droplets, the adhesive strength of the impinging droplets on aluminum was determined. Scavuzzo and Chu (1987) conducted shear stress tests at the Icing Research Tunnel at the NASA Glenn Research Center in which two cylinders were utilized. One cylinder was hollow with a larger inside diameter than the outside diameter of the second cylinder. Ice was formed between the two cylinders, and a force was applied to the cylinders until debonding occurred.

Figure 15 is a schematic of an experimental setup used by Reich (1994), and (D. N. Anderson & Reich, 1997) to determine the shear strength of the bond between ice and a substrate. Ice was adhered to a substrate, which was held between a moving stage and a

stationary stage with a rough surface. Force was applied to the moving stage until debonding occurred between the substrate and ice that has adhered to its surface.

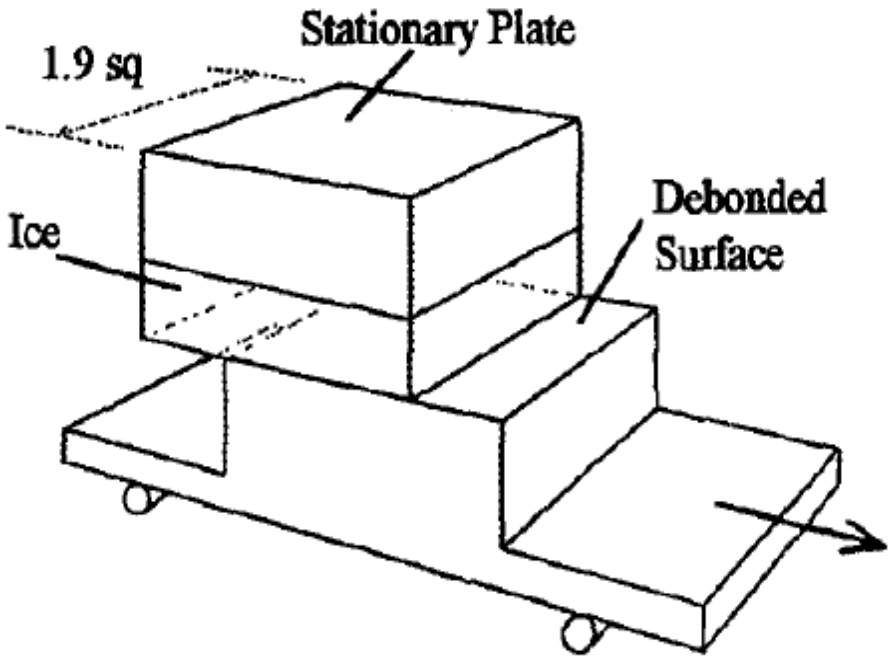

Figure 15. Schematic of an experimental setup used by to determine the shear strength of the bond between ice and a substrate (D. N. Anderson & Reich, 1997; Reich, 1994).

Table 1 lists the results of numerous ice adhesion tests conducted on various substrates throughout literature (Fortin et al., 2010). According to Fortin et al. (2010) the highest adhesive strength reported in literature for bare aluminum was 1.520 MPa, and the lowest reported adhesive strength was 0.002 MPa. The large range and the variation in the reported adhesive strength data throughout literature is due to a number of factors, such as different testing conditions and experimental techniques, as well as surface finish, size, and type of substrate being used, making it difficult to quantify the adhesive strength of ice with an absolute value (Fortin et al., 2010). Refer to Fortin et al. (2010) for additional information, such as the sources of the values in Table 1.

Table 1

Results of ice adhesion tests conducted throughout literature (Fortin et al., 2010).

Substrate	Adhesive Shear Stress (MPa)		
	Minimum	Average	Maximum
Aluminum	N/A	1.520	N/A
Copper	N/A	0.850	N/A
Polymers	1.030	N/A	1.170
Aluminum	0.067	N/A	0.400
Aluminum	0.002	N/A	0.110
Stainless Steel	N/A	0.480	N/A
Aluminum	0.050	N/A	0.300
Aluminum	0.142	N/A	0.267 (smooth) 2.279 (rough)

In an effort to quantify the adhesive strength of ice on a substrate and the effectiveness of coatings used on substrates against icing, Fortin et al. (2010) developed the adhesion reduction factor (ARF). The ARF compares the average shear stress measured on coated substrates to the average shear stress measured for bare substrates. The ARF is given by

$$\frac{\tau_{bare}}{\tau_{coated}} = ARF. \qquad (2.7)$$

A bare beam would have an ARF of one, while numbers less than one would indicate an increase in the adhesive strength of ice on a substrate, and numbers larger than one would indicate a decrease in the adhesive strength of ice.

2.5. Shadowgraphing Visualization Technique

Shadowgraphing is a technique utilized in experimental fluid mechanics and heat transfer as a tool for flow visualization by displaying refractions of light based on changes in fluid density (Nepf, 2003; Panigrahi & Maralldhar, 2012). Figure 16 is a schematic of the general experimental setup for the shadowgraphing technique (Panigrahi & Maralldhar, 2012). A light source, a laser in the case of Figure 16, projects light through an object of interest, typically a fluid, dispersing light throughout the object at a certain level of intensity. As an event occurs that alters the density of the fluid, variations in the refractive index occur, deflecting or causing a phase shift in the light passing through the fluid (Nepf, 2003). A screen is typically placed opposite of the light source to capture the events occurring in the form of shadows, hence the name "shadowgraphing".

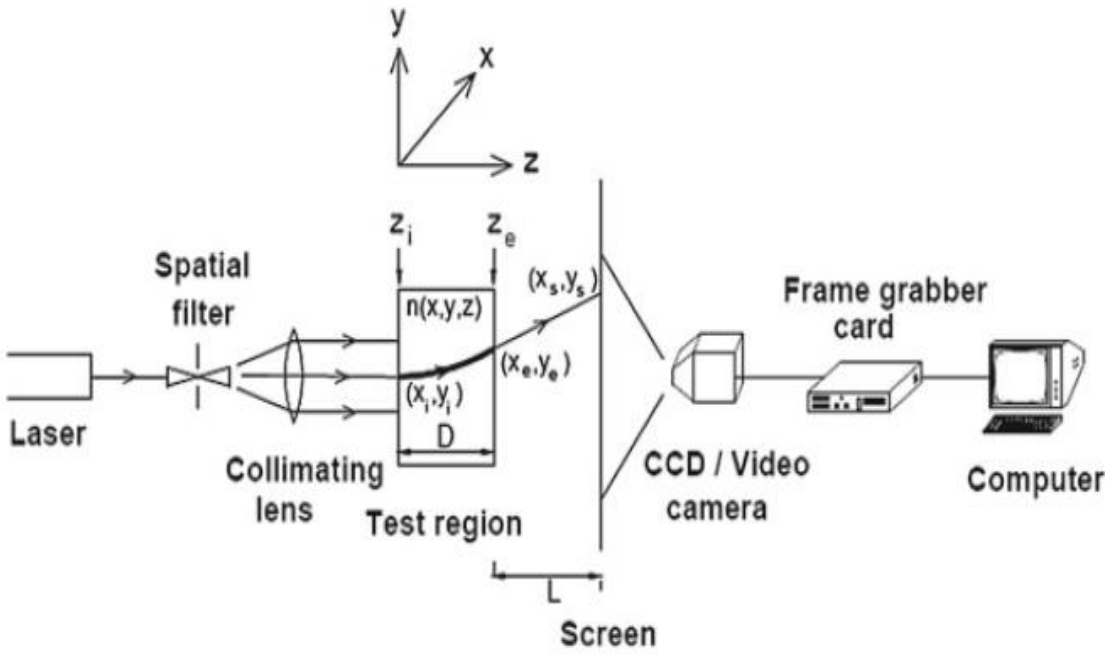

Figure 16. Schematic of the experimental setup for the shadowgraphing technique (Panigrahi & Maralldhar, 2012).

Figure 17 shows images of a heated water jet before and after the jet was activated using the shadowgraphing technique (Panigrahi & Maralldhar, 2012). Initially, ring vortices formed, progressively breaking down into turbulent flow, all of which are visible using shadowgraphing.

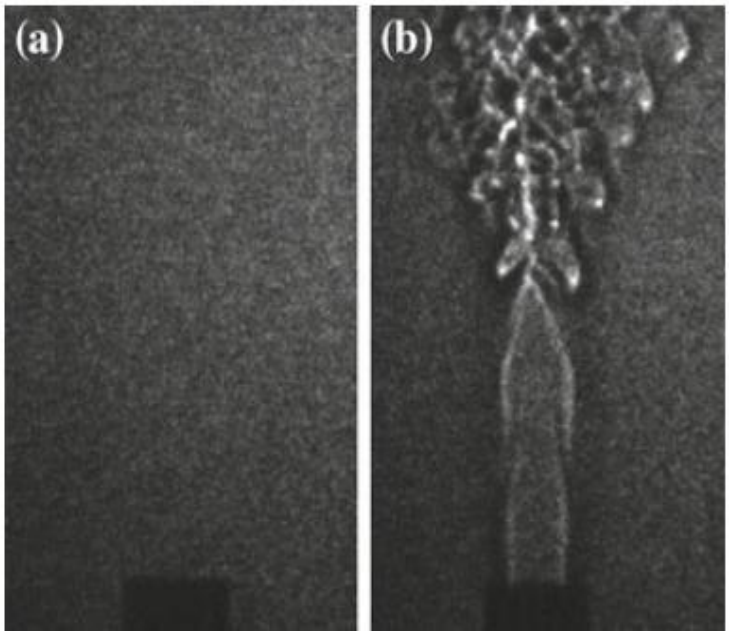

Figure 17. Images of a heated water jet (a) before and (b) after the jet was activated using the shadowgraphing technique (Panigrahi & Maralldhar, 2012).

Shadowgraphing allows for events that typically cannot be seen with the human eye to be visualized. Shadowgraphing and other flow visualization techniques are discussed in greater detail by Nepf (2003), Panigrahi and Maralldhar (2012), Parthasarathy et al. (1985), Settles et al. (2001), and Benson (2009) are recommended.

2.6. Definition of Wettability

Surface energy determines the type of interaction made by a liquid droplet when the droplet comes into contact with a surface with respect to the solid, liquid, and vapor phases present during the interaction Throughout literature, the accepted concept that is considered with regards to surface energy is Young's equation, which states that

$$\gamma_{LV} \cos\theta = \gamma_{SV} - \gamma_{SL}$$

or

$$\cos\theta = \frac{\gamma_{SV} - \gamma_{SL}}{\gamma_{LV}} \qquad (2.8)$$

where γ_{LV}, γ_{SL}, and γ_{SV} are the surface energy of the liquid-vapor, solid-liquid, and solid-vapor interfaces respectively, and θ is the contact angle of the droplet. Figure 18 is a schematic of a liquid droplet at equilibrium on a flat plate identifying the respective surface tension interfaces (Liu & German, 1996). Equation 2.2 and Figure 18, assume that the resulting contact angle of the liquid droplet depends strictly on the surface energy of the liquid-vapor, solid-liquid, and solid-vapor interfaces. Young's equation only holds true for droplets at equilibrium on a flat plate. Young's equation becomes modified when droplets are introduced to tilting plates (Kawanishi et al., 1969; Krasovitski & Marmur, 2005; Pierce et al., 2007).

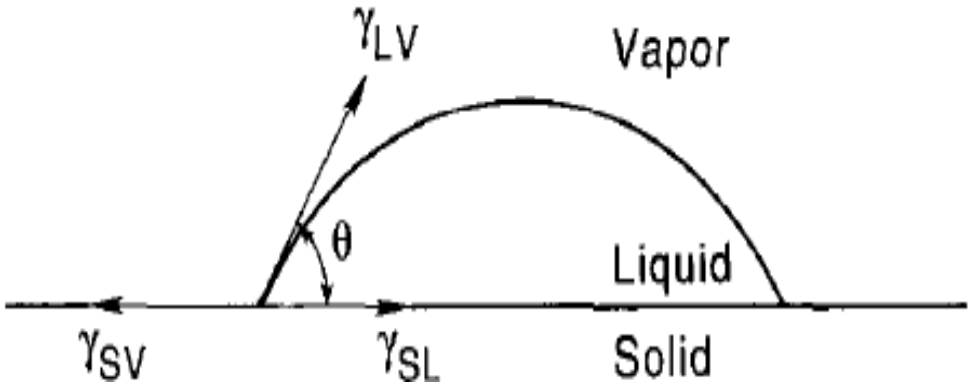

Figure 18. Schematic of a liquid droplet at equilibrium on a flat.

Characteristics of the interaction between a liquid droplet and a flat solid surface have also been reported to become modified with the addition of external influences. The wetting capabilities of a surface increase with the addition of heat, causing the sessile droplet to display contact angles below 90° (De Coninck et al., 2000; De Gennes, 1985; Findenegg & Herminghaus, 1997; Karmakov, 2000). The wetting capabilities of liquid droplets increase as

heat increases, suggesting that there may be a correlation between heating and wetting (Aksay et al., 1974; Bernardin et al., 1996; Boinovich & Emelyanenko, 2011; Hidaka et al., 2006; Janecek & Nikolayev, 2013).

Figure 19 is an image of a sessile droplet on a substrate with voltage flowing throughout the substrate (Kuo et al., 2003). In Figure 19, the droplet appears to be non-wetting, displaying a contact angle above 90°. The sessile droplet was induced with potassium chloride and set on a substrate with 700 volts flowing throughout the substrate. It is suggested that these reactions from the liquid droplet when introduced to electricity or heating is due to the fact that in its initial state, the liquid-solid interface is not at chemical equilibrium. When the droplet is presented with heat or electricity generated throughout the surface that the droplet is in contact with, the liquid-solid interface reacts accordingly (Aksay et al., 1974; Bernardin et al., 1996).

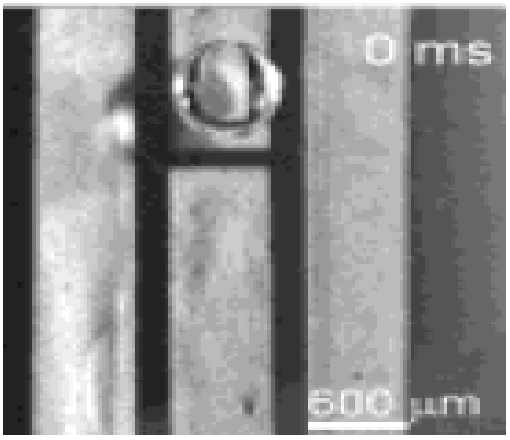

Figure 19. Potassium chloride induced sessile droplet on a substrate subject to voltage (Kuo et al., 2003).

Surfaces can be classified in five categories: hydrophobic, superhydrophobic, hydrophilic, superhydrophilic, and ice-phobic (Kako et al., 2004; Sakaue et al., 2008; Salas-Vernis et al., 2004; Zhang et al., 2010). The following sub-sections describe the classification of surfaces.

2.6.1. Hydrophobic and superhydrophobic surfaces. Surfaces are considered hydrophobic if the surface causes droplets to display a contact angle greater than 90° and superhydrophobic if the surface causes droplets to display a contact angle greater than 150°. Therefore, hydrophobic and superhydrophobic surfaces are considered non-wetting (Karmakov, 2000; Ma & Hill, 2006; Samaha & Gad-al-Hak, 2011). Hydrophobic surfaces can be produced using either coatings, or through the development of micro- and nanostructures (Kako et al., 2004; Ma & Hill, 2006; Samaha & Gad-al-Hak, 2011; Zhang et al., 2010). The effectiveness of hydrophobic and superhydrophobic materials in regards to icing has varied throughout literature. Zhang et al. (2010) developed superhydrophobic copper surfaces that they claimed had "excellent" ice resistant characteristics. Farhadi et al. (2011) developed superhydrophobic surfaces using micro- and nano-rough hydrophobic coatings and witnessed an increase in the adhesive strength of ice. Farhadi et al. (2011) concluded that superhydrophobic surfaces may not always be ice-phobic in the presence of humidity. The variance in results in the area of aircraft icing as it pertains to hydrophobic surfaces is another example of the different testing conditions and experimental techniques making it difficult to quantify the adhesive strength of ice with an absolute value (Fortin et al., 2010).

2.6.2. Hydrophilic and superhydrophilic surfaces. Surfaces are considered hydrophilic if the surface causes droplets to display a contact angle less than 90° and superhydrophobic if the surface causes droplets to display a contact angle less than 30°. Therefore, hydrophilic and superhydrophilic surfaces are considered wetting (Bonn et al., 2009; De Coninck et al., 2000; Findenegg & Herminghaus, 1997; Karmakov, 2000). Similar to hydrophobic surfaces, hydrophilic surfaces can be produced using coatings, or through the development of micro- and nanostructures (Kako et al., 2004; Salas-Vernis et al., 2004). Sakaue et al. (2008) developed a

coating capable of exhibiting hydrophobic and hydrophilic characteristics with respect to temperature. The surface of the substrate was hydrophobic as temperature increased and hydrophilic as temperature decreased. Kako et al. (2004) demonstrated that the sliding behavior of wet snow can be controlled by introducing hydrophilic channels to a superhydrophobic surface. Throughout the literature review, hydrophilic surfaces have not been reported to reduce ice adhesion.

The technique used to measure the contact angle of the sessile droplet shown in Figure 18 becomes inaccurate and impractical when measuring the contact angles of superhydrophilic sessile droplets (Allen, 2003). The measurement technique in Figure 18 assumes the droplet is in the shape of a spherical cap. However, the profile of a droplet is not in the shape of a spherical cap at contact angles below 30°. The method used to determine the contact angle of droplets that do not form as spherical caps is by calculating the curvature of the droplet by numerically solving the Laplace-Young equation (Allen, 2003). Allen (2003) developed much simpler method to determine the contact angle of droplets that display contact angles below 30° knowing only the volume and area of the droplet. The method reported by Allen (2003) is accurate only for droplets less than 30°.

2.6.3. Ice-phobic surfaces. Ice-phobicity does not particularly fall within the realms of hydrophobic or hydrophilic (Freiberger & Lacks, 1961; Thomas et al., 1996). Ice-phobicity is characterized by its ability to repel ice and not water, hence a surface that is characterized as hydrophobic does not necessarily mean that same exact surface is ice-phobic (D. N. Anderson & Reich, 1997; Thomas et al., 1996). Ice possesses different characteristics than water in terms of density and phase. Techniques used to deter water, will not deter ice. Materials specifically tailored to be ice-phobic have only been known to be produced in the form of coatings (Fortin et

al., 2010; Freiberger & Lacks, 1961). Ice-phobic coatings lose their effectiveness with each application and removal of icing (Due et al., 1996; Scavuzzo & Chu, 1987).

2.7. Literature Review Conclusion

Each anti-icing and de-icing technique developed comes with its own benefits and limitations. No single anti-icing or de-icing technique reviewed throughout the literature review reportedly completely deterred icing without any issues. The data collected throughout years of literature on the adhesive strength of ice varies due to different testing conditions and experimental techniques used by various authors making it difficult to assign an absolute value to the adhesive strength of ice (Fortin et al., 2010). Reich (1994) commented that the ideal method for deterring ice adhesion to aircraft structures should be both hydrophobic and ice-phobic. Numerous studies have been, and are continuing to be, conducted to develop a material that possesses a surface that is both hydrophobic and ice-phobic in the area of aircraft icing. There is not much emphasis being put on the ice-phobic property. It should be noted that throughout the literature review, hydrophilic surfaces have not been reported to reduce ice adhesion.

CHAPTER 3

Methods and Materials

The following chapter describes the equipment, experimental setup, and procedures used to meet the specific objectives of the present study. The adhesive strength tests were used to determine the adhesive strength of the bond between ice that has formed and adhered to the surfaces of bare and surfactant coated aluminum, stainless steel, copper, and polycarbonate substrates at subcooled temperatures. The contact angles of sessile droplets interacting with bare and treated substrates were measured to monitor changes in surface energy as it pertains to the particular surfaces being observed. Observations of freezing of sessile droplets were conducted to monitor the nucleation process of sessile droplets at subcooled temperatures and develop a rate of freezing for the event. Finally, heat transfer lumped system analysis on the sessile droplet exposed to subcooled conditions was done to develop an understanding of the cooling process of a sessile droplet in a cooled environment analytically.

3.1. Determination of the Adhesive Strength of Ice on Various Substrates

Shear stress tests were performed to determine the adhesive strength of ice that has adhered to various substrates chosen to simulate materials aircraft structures. The shear stress tests were conducted on bare aluminum at -5, -10, -20, and -30°C. Experiments were also conducted on methoxymethylethoxypropanol, polymethylhydrosiloxane, and octylphenol ethoxylate treated aluminum, stainless steel, copper, and polycarbonate substrates at -10°C. An additional experiment was conducted on bare aluminum, stainless steel, copper, and polycarbonate substrates to determine a baseline of the adhesive strength of ice.

All shear stress testing was conducted in an environmental chamber built in-house at North Carolina Agricultural and Technical State University. Determining the size of the substrates was important before any tests were conducted. Shear strength is given by

$$\tau = \frac{F}{2A_s} \tag{3.1}$$

where F is the applied force, and A_s is the surface area at which the force is being applied. The shear strength of the bond between the ice and various substrates was monitored with a PASCO brand High Resolution Force Sensor, model number PS-2189. In order to determine the size of the substrates, it was necessary to know the capabilities and limitations of the PASCO PasPort High Resolution Force Sensor being used in this experiment and develop the substrates accordingly. The force sensor senses forces up to ±50 N and features a resolution of 0.002 N, a maximum sampling rate of 1000 Hz (or 1000 samples per second), and dynamic variable over-sampling, which aids in the reduction of measurement noise at low sample rates. According to literature, the highest shear strength reported was 1.520 MPa, and the lowest 0.002 MPa, both on aluminum substrates at -10°C (Fortin et al., 2010). Given that information, the following parameter regarding the area of the substrates used in this experiment was developed

$$0.004\ MPa\ \leq \frac{50\ N}{A_s} \leq 3.04\ MPa$$

or

$$0.00002\ m^2 \leq A_s \leq 0.0125\ m^2.$$

In order for this experiment to be successful, given the limitations of the PASCO PasPort High Resolution Force Sensor, the surface area of the substrates had to fall within the parameters above. The substrates used in this experiment were 19.05 mm by 6.35 mm by 0.76 mm aluminum, copper, steel, and polycarbonate strips. The surface area of the substrates used in this

experiment was calculated to be 0.00024 m^2. The thickness was neglected and it was acknowledged that ice adhesion would occur on the front and back surfaces of the substrate.

Each material was chosen to simulate the materials used to fabricate aircrafts and the particular size of the materials was determined to accommodate the capabilities of the PASCO PasPort High Resolution Force Sensor being used. The PASCO PasPort High Resolution Force Sensor was connected to a PASCO Xplorer GLX Handheld Datalogger. The PASCO Xplorer GLX Handheld Datalogger directly collected, graphed, and allowed for analysis of collected data without the use of a computer.

Fishing wire, with a maximum strength of up to 13.61 kg was used in this experiment to link the substrates to the PASCO PasPort High Resolution Force Sensor. In order to accommodate the fishing wire being used in this experiment, a 1.60 mm hole was drilled into each substrate. Figure 20 shows an image of the configuration of the fishing wire used in the present study. The Trilene fishing wire was tied through each substrate, secured by a knot, and a loop was made at the opposite ends of the Trilene fishing wire, secured by another knot, to allow the substrates to hang.

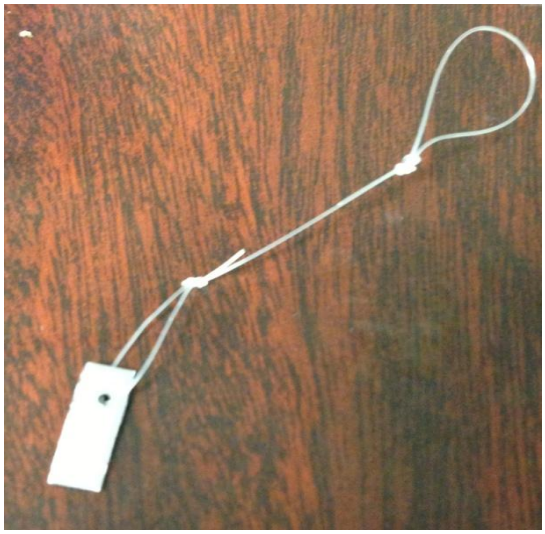

Figure 20. Configuration of the fishing wire used in the present study.

Each substrate was wiped thoroughly using Sterahol, an ethanol, methanol, and isopropyl alcohol solution, to rid the surfaces of the substrates of any contamination, as well as fingerprints after the Trilene fishing wire was tied through the substrate and the loop was created at the opposite end. Ridding the surfaces of the substrates of contamination was important to do before placing the substrates into the environmental chamber because any sort of contamination, or fingerprints, can affect the surface energy and adhesive strength between the ice and substrate. As each substrate was cleansed, they were hung on a rod and allowed to air dry.

Figure 21 is a schematic of a substrate frozen within ice and the direction that force was applied, all of which are within a modified ice tray. In order to successfully complete the shear stress testing while ensuring that the substrates are never exposed to room temperature and allowed to melt, an ice tray was modified with a polycarbonate cover. The polycarbonate cover ensured that all ice that formed in the ice tray was held in its respective area in the event that the ice dislodged from the tray. All tests were conducted within the environmental chamber.

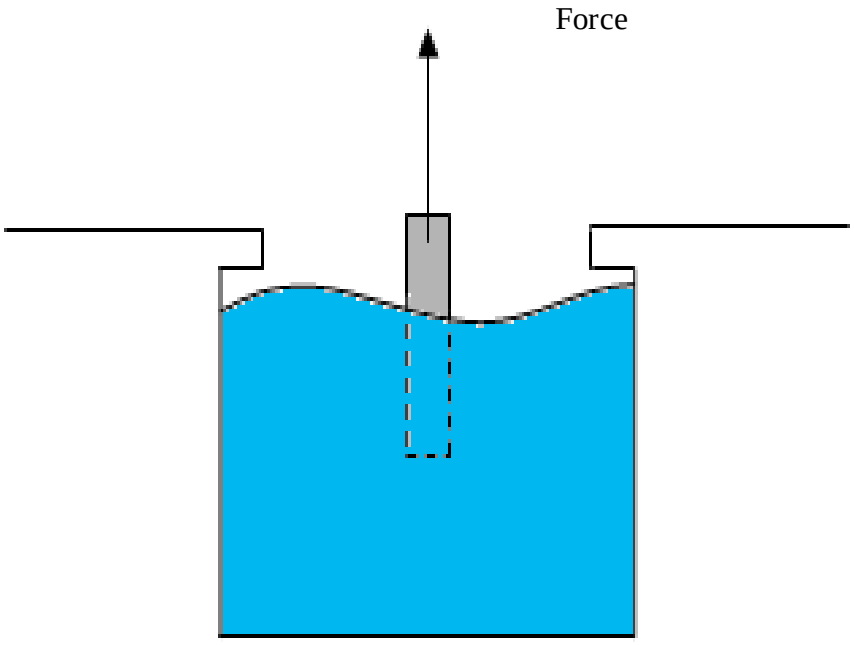

Figure 21. Schematic of a substrate frozen within ice in a section of the modified ice tray.

The modified ice tray was also cleaned with Sterahol, while the substrates were drying. The substrates were then placed into their own respective sections of the tray and distilled water was poured into each section of the tray accordingly, covering approximately 6.35 mm of the substrates. It was important to ensure that the water does not come into contact with the Trilene fishing wire or the hole drilled to accommodate the fishing wire and be aware that water expands as it freezes. Measurements would exceed the sensing capabilities of the PASCO PasPort High Resolution Force Sensor if the Trilene fishing wire or the holes drilled in the substrates to accommodate the fishing wire were frozen within the ice. Trials that exceeded the sensing capabilities of the force sensor were discarded, and testing would be redone.

Prior to every test, before a load was applied, the button labeled "zero" on the PASCO PasPort High Resolution Force Sensor was pressed to calibrate the data acquisition system. Pressing the "zero" button would set the sensor to zero before any load was placed on the PASCO PasPort High Resolution Force Sensor. Values measured while the force sensor was not calibrated were discarded and the test was redone.

Figure 22 is an image of the experimental setup used to conduct the shear strength tests. The PASCO PasPort High Resolution Force Sensor was equipped with a hook. The loop used to originally hang the substrate was placed over the hook. The button on the PASCO Xplorer GLX Handheld Datalogger with the "play" symbol was pressed after pressing the button labeled "zero". The button with the "play" symbol initiates the data logger and any force applied to the force sensor would be measured and recorded by the force sensor. The data logger stores all of the values measured internally until the user manually stops the data logger by pressing the "play" button a second time. Force was manually applied until the substrate was dislodged from

ice. As the load was applied to the PASCO PasPort High Resolution Force Sensor, the PASCO Xplorer GLX Handheld Datalogger recorded the event.

Figure 22. Experimental setup for the shear strength tests.

Figure 23 is an image of ice that has been cracked due to the application of cyclic loading while conducting a shear strength test. It was important to ensure that the force being applied was constant and not done in a repetitive loading and unloading type cycle. Loading and unloading the force would apply a cyclic load to the substrate, causing cracks to propagate within the ice, weakening the integrity of the bond, and causing the PASCO Xplorer GLX Handheld

Datalogger to log incorrect data. In the event of ice cracking, as shown in Figure 23, the data measured was discarded.

Figure 23. Ice cracked due to the application of cyclic loading.

Measurements of the shear strength of ice was made on aluminum, stainless steel, copper, and polycarbonate substrates, bare and treated with methoxymethylethoxypropanol, polymethylhydrosiloxane, and octylphenol ethoxylate. The measured data was recorded in an excel spread sheet. Fortin et al. (2010) commented that there is a large range and variation in the reported adhesive strength data throughout literature due to factors, such as different testing conditions and experimental techniques, as well as surface finish, size, and type of substrate

being used, making it difficult to quantify the adhesive strength of ice with an absolute value. In order to gauge the effectiveness of the data collected from the shear strength tests while using surfactants, an adhesion reduction factor developed by Fortin et al. (2010) was used. Equation 2.1 was used to calculate the ARF. The ARF compares the average shear stress measured on treated substrates to the average shear stress measured for bare substrates. A bare beam would have an ARF of one, while numbers less than one would indicate an increase in the adhesive strength of ice on a substrate, and numbers larger than one would indicate a decrease in the adhesive strength of ice.

3.1.1. Environmental chamber. Shear strength tests were conducted in an environmental chamber built in-house at North Carolina Agricultural and Technical State University. Figure 24 is an image of the environmental chamber used to simulate subcooled conditions. The structure of the environmental chamber was built using 80/20 Incorporated 2020 aluminum beams from their 10 series profile. The dimensions of the environmental chamber are 546.10 mm by 736.60 mm by 1485.90 mm. Housed within the chamber are two large custom aluminum cooling plates built in-house, and between the larger cooling plates are four smaller Lytron Total Thermal Solutions aluminum cooling plates (304.80 mm by 95.25 mm by 8.13 mm). Copper tubing (12.7 mm OD) purchased from McMaster-Carr was used throughout the entire system to direct the flow of all working fluids. The aluminum beams that the environmental chamber was comprised of were covered by 6.35 mm thick Lexan polycarbonate sheeting. The polycarbonate sheeting was attached to the environmental chamber using sealed by 50.8 mm wide silicone sealing strips. The exterior of the entire environmental chamber is encased in reflective air-bubble wrap insulation, while the inside of the chamber is layered with polystyrene foam panels.

Figure 24. Environmental chamber used to simulate subcooled conditions.

Initially, the ambient temperature within the lab appeared to affect the temperature of the working fluid by ±3°C. The fluctuation in temperature was possibly due to the lack of less than perfect insulation around the copper tubing as well as the chamber itself. To deter this problem, the insulation was observed and modifications were made to the insulation accordingly. Figure 25 shows the interior of the environmental chamber before and after polystyrene foam panels and polystyrene spray foam were installed into the environmental chamber. The copper tubing outside of the chamber was heavily insulated with foam pipe insulation and the inside of the chamber was layered with polystyrene foam panels. The crevices around the foam panels were sealed using polystyrene spray foam. Installing the polystyrene foam panels and polystyrene spray foam enhanced the cooling capabilities of the environmental chamber by lowering the

temperature inside the environmental chamber from -2°C to -15°C. The Polyscience Circulating bath struggled to cool the working fluid to temperatures below -30°C. The aforementioned lack of insulation and the pump speed of the fluid were possible contributing factors affecting the lack of cooling. Reducing the pump speed of the Polyscience Circulating bath contributed to cooling the fluid by as much as -5°C.

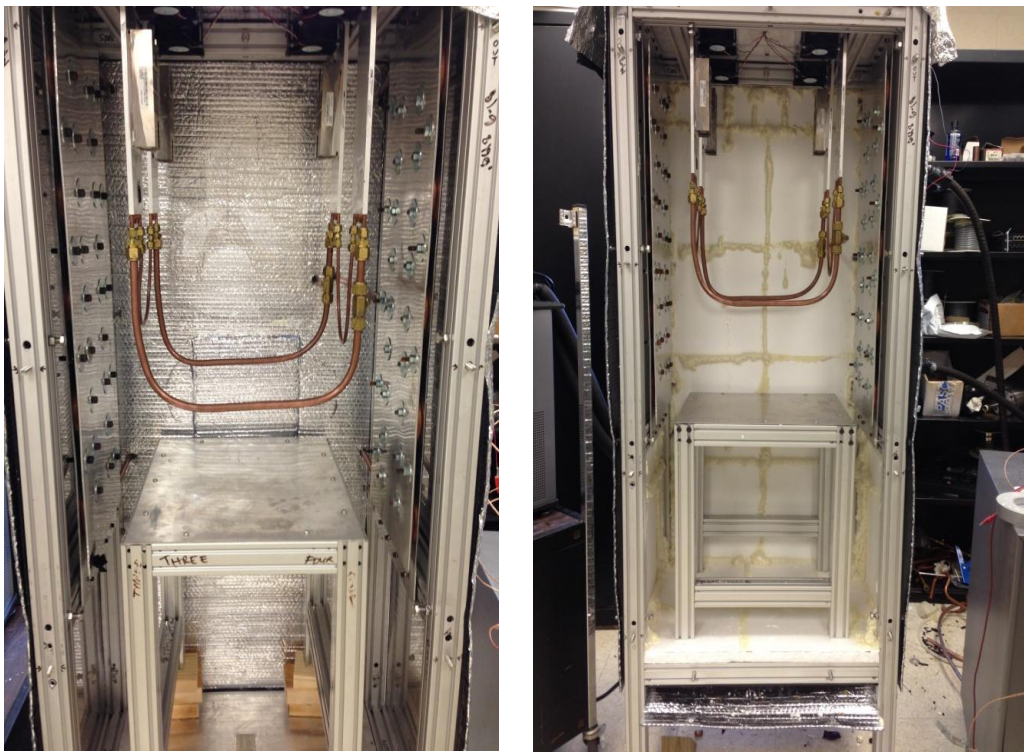

(a) (b)

Figure 25. Environmental chamber (a) before and (b) after installing polystyrene panels.

The environmental chamber utilizes a Remcor Industrial chiller (model CH-950) and a Polyscience Circulating Bath (model PP15R-40). The working fluid throughout the entire system is Dynalene HC, purchased from Polyscience under the consumer name: Polycool-HC50. Dynalene HC is a colorless to light yellow, odorless, liquid capable of achieving temperatures as high as 100°C and as low as -50°C. The chiller and bath combination was used because the

Remcor Industrial chiller can only reach a minimum of -1.11°C by itself and the cooling capacity of the Polyscience Circulating Bath alone was not enough to cool the entire chamber to the desired temperatures in a timely fashion. The Remcor Industrial chiller was initially activated and allowed to cool the larger cooling plates and the air within the chamber to approximately -1.11°C. The Polyscience Circulating Bath was then activated to take on the remainder of the cooling process and allowed to cool all of the cooling plates simultaneously, along with the air within the chamber, to the desired temperatures.

Flow of the fluid throughout the chamber was controlled by two sets of valves which allowed either the Remcor Industrial chiller or the Polyscience Circulating Bath to cool the entire system alone, or both chillers to run and cool the system simultaneously. Through numerous trials it was observed that achieving -40°C using the chiller and bath combination alone was not possible, and the minimum temperature possible was -15°C. There are several reasons why this holds to be true: less than perfect insulation, the absorption of energy from heat sources, flow rate of the working fluid throughout the system, or even the configuration of the copper tubing that the working fluid was transported through are just a few possibilities. In order to contribute to the cooling process, 45.36 kg of solid carbon dioxide, dry ice, was placed at the bottom of the chamber and allowed to sublimate within the chamber, further cooling the air within the chamber to reach the desired temperature of -40°C.

Heat sinks were attached to the Lytron Total Thermal Solutions cooling plates within the environmental chamber to assist in the heat transfer process. Each heat sink was attached to a Lytron cooling plate using Omega Engineering brand thermally conductive epoxy. Above each heat sink was 0.85 ampere, 12 volt cooling fans. The cooling fans allowed the energy from the cooling plates, as well as the heat sinks, to circulate within the chamber. The cooling fans were

scavenged from decommissioned Gateway computers, model number E-2610S. The wiring of the cooling fans were arranged in a parallel circuit and powered by a 12 volt power supply. The cooling fans were activated while the Dynalene HC-50 flowed throughout the system. Temperature was monitored using an IOTech Data Acquisition System, series number 6222. The IOTech Data Acquisition System is a twelve channel, 12 port, 24 bit, thermocouple input module device that connects directly to a PC via Ethernet cable.

3.1.2. Uncertainty analysis. Uncertainty analysis was done for the data measured in the shear stress tests in order to determine the quality of the measured data. Uncertainty analysis provides a range of which the true value is expected to fall within, while taking into account measurement errors and random uncertainty. The true value of the shear stress necessary to cause debonding between ice and the various substrates under the given conditions throughout the shear stress tests are unknown, however, the data measured throughout the experiment provides enough information to formulate a range of probable error. Since there were less than 30 values measured per data set, each data set was approached as a sample data set, thus the sample mean, $\bar{x}$, sample variance, ${s_x}^2$, and the sample standard deviation, s_x, are respectively defined by

$$\frac{1}{N}\sum_{i-1}^{N} x_i = \bar{x} \tag{3.2}$$

$$\frac{1}{N-1}\sum_{i-1}^{N} (x_i - \bar{x})^2 = {s_x}^2 \tag{3.3}$$

$$\sqrt{\frac{1}{N-1}\sum_{i-1}^{N} (x_i - \bar{x})^2} = \sqrt{{s_x}^2} = s_x \tag{3.4}$$

where *N* is the total number of samples, and x_i is each individual measured value, where $i = 1, 2, 3, \ldots, N$. The sample mean value provides the most plausible estimate of the true mean value, and the sample variance the most plausible measurement of the variation within a data set (Figliola & Beasley, 2011). Experiments that require repeated measurements be taken under fixed operating conditions inevitably encounter random error, which could be due to measurement procedures and techniques, calibration of the equipment, resolution of the equipment, and even the environmental conditions which measurements are being taken (Figliola & Beasley, 2011). Random error is, in essence, the explanation for why data sets in experiments that require multiple measurements are often scattered, as opposed to constant. Random uncertainty provides an estimate of probable range of random error present within a data set. Random uncertainty, x', is defined by

$$\bar{x} \pm t_{\nu,P} s_{\bar{x}} = x' \tag{3.5}$$

where ν is the degrees of freedom in a data set, defined by $\nu = N - 1$, P is the percent probability, $t_{\nu,P}$ is a coverage factor used for finite data sets that represents a precision interval at a given percent probability, and $s_{\bar{x}}$ is the random standard uncertainty. The parameter $s_{\bar{x}}$ can be defined as

$$\frac{s_x}{\sqrt{N}} = s_{\bar{x}}. \tag{3.6}$$

The solutions for $t_{\nu,P}$ were found using a t distribution chart. Assuming a t distribution through a data set also assumes that there is a normal distribution of random error throughout the data set. Equations 3.2 through 3.6 were applied in order to determine the random error throughout the data at 95% probability after acquiring the data during the shear stress tests.

3.2. Determination of Contact Angles

The contact angles of water on the various substrates were measured in order to monitor any deviation that occurred between the surface energy between distilled water and the modified substrates, compared to that of distilled water and the bare substrates. The contact angles of a sessile droplet on bare, aluminum, stainless steel, copper, and polycarbonate substrates was measured to develop a reference for the contact angles. The contact angles of methoxymethylethoxypropanol, polymethylhydrosiloxane, and octylphenol ethoxylate treated, aluminum, stainless steel, copper, and polycarbonate substrates was then measured. The reference contact angles indicate any deviation of the contact angles measured on the treated surfaces compared to the respective bare substrates.

The substrates used in this experiment were 25.40 mm by 25.40 mm aluminum, stainless steel, copper, and polycarbonate square plates. As in the previous section, each substrate was wiped thoroughly using Sterahol, an ethanol, methanol, and isopropyl alcohol solution, to rid the surfaces of the substrates of any contamination, as well as fingerprints. Ridding the surfaces of the substrates of contamination was important to do before observing the contact angles that the distilled water displayed while interacting with the surfaces of the substrates because any sort of contamination, or fingerprints could affect the surface energy and contact angles between the distilled water and substrate.

Figure 26 shows a schematic of the experimental setup used to observe the contact angles of droplets on the various substrates used throughout the present study. The substrates were then allowed to air dry after being cleansed with Sterahol. A 0.10 mL droplet of distilled water was then administered on the surface of the various substrates. The substrates were then placed in

between a Cowboy Studio Tricolor backlight, and a Nikon D5100 Digital Camera. All images were taken using the Nikon D5100 Digital Camera and saved as JPEG files on a local computer.

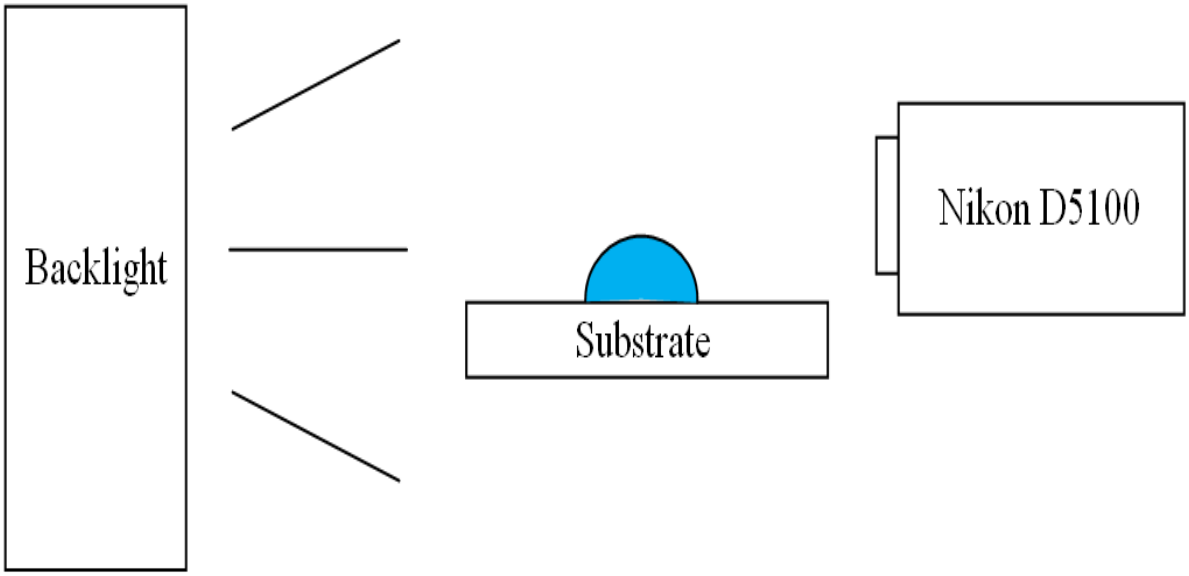

Figure 26. Schematic of the experimental setup used to observe the contact angles of droplets on the substrates used throughout the present study.

Figure 27 shows a schematic of the method used to measure the contact angle of a droplet relative to the surface of the substrates. The particular angle being measured was the angle created between the liquid-solid interface and the solid-vapor interface of the droplet. All of the images were then analyzed using ImageJ, a Java based image processing program developed by the National Institute of Health (Ferreira & Rasband, 2013). ImageJ features an Angle tool that was utilized to measure the contact angle of the droplets on the various substrates. The Angle tool in ImageJ requires the user to draw two intersecting lines and measures the angle between the lines. The JPEG files saved of the images of the droplets on the various substrates taken by the Nikon D5100 Digital Camera were each individually imported into ImageJ and analyzed. The plane that the liquid-solid interface was located on was identified in the JPEG files and the

first line was drawn along that plane. The contact point of the droplet was then identified, and a second line was drawn linearly along the surface of the droplet, intersecting with the contact point of the droplet and the initial line drawn along the plane of the liquid-solid interface.

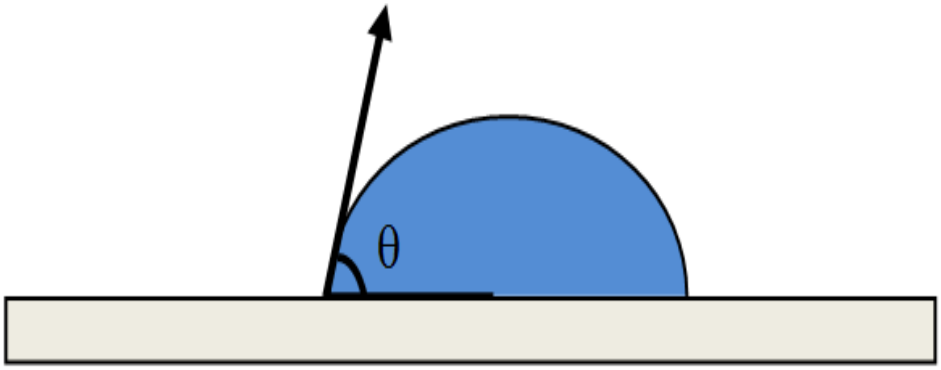

Figure 27. Schematic of the method used to measure the contact angle of a droplet.

The Measure tool was used in ImageJ in order to obtain an approximate value for the angle between the intersecting lines after drawing the two intersecting lines. Wettability was measured on bare, methoxymethylethoxypropanol, polymethylhydrosiloxane, and octylphenol ethoxylate treated aluminum, stainless steel, copper, and polycarbonate substrates. When applying the surface treatments to the substrates, similar procedures were followed as those used to measure the contact angles of distilled water on the bare materials.

The substrates were first cleaned with Sterahol to rid the surfaces of any unwanted contamination and fingerprints and allowed to air dry. The surfactants were then applied and allowed to air dry once more before applying a 0.10 mL droplet of distilled water. The bare and methoxymethylethoxypropanol treated substrates dried in approximately twenty minutes. However, the polymethylhydrosiloxane and octylphenol ethoxylate surfactants possessed an oily consistency and would not completely dry. Since neither the polymethylhydrosiloxane nor octylphenol ethoxylate surfactants would air dry, the 0.10 mL droplet of distilled water was

applied on top of the surfactants and the contact angle made during that interaction was observed.

Surfaces that displayed superhydrophilic characteristics were measured using an analytical solution for the determination of small contact angles of sessile droplets of arbitrary size developed by Allen (2003) was used. The contact angle of sessile droplets less than 30° is given by

$$\theta \approx tan\,\theta \cong \frac{4V}{\pi r^3} \tag{3.7}$$

where *V* is volume, and *r* is radius. Equation 3.7 is only valid if the contact angle is less than 30° and the bond number, β, is less than one. Allen (2003) provided equations for bond numbers greater than one, but warned that the equations for bond numbers greater than one are not as accurate as Equation 3.7. The contact angle of superhydrophilic sessile droplets where β>4, can be approximated by

$$\theta \approx tan\,\theta \cong \frac{V}{\pi r^2 L_c}\left(\frac{\beta}{\beta - {}^3/_2}\right). \tag{3.8}$$

The contact angle of superhydrophilic sessile droplets where β>25, can be approximated by

$$\theta \approx tan\,\theta \cong \frac{V}{\pi r^2 L_c}. \tag{3.9}$$

The bond number is a measure of the relative effects of the gravitational and capillary forces on the shape of the liquid surface. The bond number is expressed as

$$\frac{r}{L_c} = \beta \tag{3.10}$$

where *r* is the radius of the sessile droplet, and L_c is the capillary length, which is given by

$$\sqrt{\frac{\sigma}{(\rho_l - \rho_v)g}} = L_c \tag{3.11}$$

where σ is surface tension, g is acceleration due to gravity, and ρ_l and ρ_v are the density of the liquid and vapor phases, respectively. Throughout literature, the surface tension of water has been reported to be 72 N/m^2, gravity due to acceleration is 9.81 m/s^2, and the density of water and air are accepted at 1000 kg/m^3 and 1.20 kg/m^3 respectively (Cengel & Boles, 2008; Samaha & Gad-al-Hak, 2011). Given the parameters of the variables necessary to determine the capillary length, the capillary length can be calculated.

The radius of the sessile droplet, *r*, was determined by analyzing JPEG images captured by the high speed camera using ImageJ. An image was opened in ImageJ, and initially, a scale was set using the 'set scale…' feature in ImageJ based on any distinguishable, yet measureable, feature in the image with respect to the number of pixels. The distinguishable feature chosen for this experiment was the substrate that the droplet was placed on, which was measured to be 25.40 mm by 25.40 mm. Using the 'straight line' tool, a horizontal line was made across the substrate to reference the width of the substrate. 'Set scale…' was found in the ImageJ toolbar under the tab labeled 'analyze'. The number of pixels within the line made earlier to reference the width of the substrate was noted after choosing 'set scale…' in ImageJ. The known distance and unit of the known distance were input into ImageJ.

A horizontal line was then made across the solid-liquid interface of the sessile droplet, from end to end of the droplet profile. The "measure" feature was then utilized to determine the length of the newly drawn line based on the scale that was previously set. The length that was measured in ImageJ using the "measure" feature is the diameter of the sessile droplet. A vertical line was drawn at the center of the sessile droplet using identical procedures to determine the

height of the sessile droplet. The parameter β was then calculated to determine the bond number after determining the diameter of the sessile droplet. Once the bond number is determined, Equation 3.7., 3.8, or 3.9 can then be applied accordingly. Equations 3.7-9 require the volume of the sessile droplet to be known to determine the contact angle of sessile droplet. As mentioned in Chapter 2.5.2., the profile of a superhydrophilic sessile droplet does not form in the shape of a spherical cap. It is adequate to assume the shape of a spherical cap after determining the radius and height of the sessile droplet. The volume, *V*, of a spherical cap is given by

$$\frac{1}{6}\pi h(3r^2 + h^2) = V. \tag{3.12}$$

The contact angle of the sessile droplet can be calculated after calculating the volume of the superhydrophilic sessile droplet.

3.3. Visualization and Measurement of Freezing Rate of Sessile Droplets

A sessile droplet is a static droplet; therefore it is a steady droplet with no form of velocity or acceleration. Observation of freezing a sessile droplet was made in order to determine the nature and rate of the freezing process. Observations were made in an environmental chamber built in-house at North Carolina Agricultural and Technical State University. Figure 28 shows a schematic of the experimental setup used to observe the freezing process of a sessile droplet. A 0.5 mL syringe was filled with distilled water and placed on a chemistry test stand equipped with a clamp that was used as a syringe holder. The syringe was first held upside down so that any air entrapped within the syringe would rise to the needle tip and the syringe was relieved of any air before observing the freezing process of the sessile droplet. Residual air was released from the syringe to avoid air bubbles from getting captured within the sessile droplets being formed.

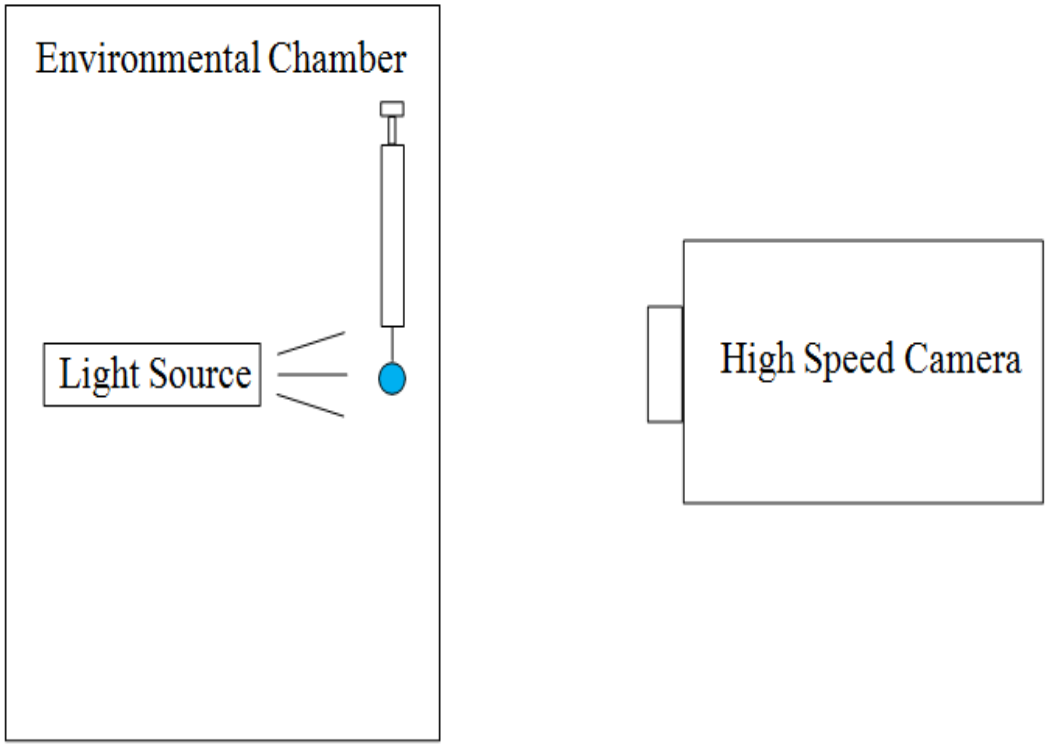

Figure 28. Schematic of the experimental setup used to observe the freezing of a sessile droplet.

The tip of the syringe was removed and made flat as opposed to maintaining its original acute tip. The needle tip was removed using a Dremel saw and the tip was smoothened using 360 grit sand paper. Removing the needle tip was done because the sharp tip on the syringe diffracted light into the camera and appeared as a dark oval. The acute tip also affected the orientation of the droplet itself; with the sharp tip, the droplet did not dispense from the syringe as a symmetrical droplet but rather one that was lopsided. During this experiment it was essential to ensure that the droplet was dispensed symmetrically and the tip was flat because the orientation of the droplet (i.e. a lopsided droplet due to the syringe needle with the pointed tip) affected how and where the droplet began to nucleate during the freezing process.

Figure 29 shows an image of the experimental setup used to visualize freezing sessile droplets. The test stand was placed into the environmental chamber between the Fiber-Lite

Illuminator System and a high speed camera after the syringe was clamped and secured to the chemistry test stand. Images were taken in the chamber using a high-speed camera. The high speed camera had capabilities of recording up to 50,000 frames per second and the software associated with the high speed camera was the Photon FASTCAM Viewer (PFV) for High-speed Digital Imaging, version .323.

Figure 29. Experimental setup used to visualize freezing sessile droplets.

The interface for the PFV software was used to specify the settings for the high speed camera prior to operating the camera. The general settings used while recording video for this experiment with the high speed camera was a resolution of 1024 by 1024 and a frame rate of 250 frames per second. The high speed camera records a total of 5457 frames, each frame occupying a frame of time. The higher the frame rate the smaller the window of time the user was allowed to record and vice versa. At smaller frame rates, the user is allowed to record a larger window of

time, but risks missing important events due to the lack of frames being recorded. A frame rate setting of 250 frames per second was optimal for this experiment since it captured enough frames to reveal what occurred throughout the freezing process, as well as allowing an efficient time window.

Icing can occur within a matter of milliseconds, and what makes icing even more inconvenient is the unpredictability of when the sessile droplet would begin to nucleate. The trigger mode of the high speed camera was changed to 'end mode' to account for the unpredictability of nucleation. In 'end mode' the high speed camera continuously records until the user manually stops recording an event. However, while in 'end mode' when the high speed camera reaches the maximum number of frames it can record, the high speed camera proceeds to continuously dump the earliest images, which are temporarily saved internally within the high speed camera, to make room for the newest images. The time window allowed for the user to manually stop recording the images taken by the high speed camera correlates with the frame rate chosen, and as previously mentioned, the higher the frame rate the smaller the window of time the user is allowed to record, and vice versa.

A Fiber-Lite Illuminator System was used as the backlight while recording images with the high speed camera within the chamber. The Fiber-Lite Illuminator System uses fiber optics as a method of absorbing heat and producing a high intensity cold light. The fiber optic backlight does not radiate heat into the chamber, while other types of lighting sources generally operate as hot lights and become heating sources. The fiber optics in the Fiber-Lite Illuminator System was housed in a gooseneck light pipe which allowed for versatility in the positioning of the lighting. The ability of having versatility in the positioning of the lighting was important because when positioning the light behind the sessile droplet, the light had to be repeatedly positioned where

there was little to no inequalities in the lighting throughout the droplet. The inequalities would typically show in the images being recorded by the high speed camera as dark spots around the edges of the droplet. The goal behind adjusting the Fiber-Lite Illuminator System was to eliminate the majority of the dark spots within the droplet that was being captured by the high speed camera, leaving only a faint outline of the sessile droplet.

The test stand was placed into the environmental chamber between the Fiber-Lite Illuminator System and a high speed camera after the syringe was clamped and secured to the chemistry test stand. The proper settings were applied to the high speed camera. The Fiber-Lite Illuminator System was adjusted to the desired position. The high speed camera was activated and images were captured. The camera was manually stopped after the sessile droplet was completely frozen. The freezing process was monitored using a shadowgraphing technique. Shadowgraphing is an optical tactic that reveals non-uniformities throughout events that would regularly appear transparent via refractions in the lighting. The outline of the droplet with light being generated from the Fiber-Lite Illuminator System shining through the droplet should be visible if configured correctly. As freezing occurred, the droplet began to darken until it was almost completely black, and most of the light generated by the Fiber-Lite Illuminator System was no longer seen through the droplet. However, if configured incorrectly, the light will not be diffracted from the high speed camera in a manner that would reveal the solidification process; instead the outline of the droplet will remain as an outline throughout the freezing process.

The frames that were recorded by the high speed camera was viewed and edited to remove any useless and repetitive frames that were recorded, minimizing the size of the files that were to be saved. All of the frames recorded by the high speed camera were saved as both AVI and JPEG files. The AVI file offered a visual of the entire event in real time as it occurred, while

the JPEG files offered frame by frame visuals of the event. The JPEG files become helpful when observing the transitions made by the sessile droplet during the freezing process with respect to time, which is impractical when viewing the AVI file. Each individual JPEG possesses important information such as the frame rate and resolution that was used while recording the image and the specific time of occurrence of the event within that frame. The time elapsed for the sessile droplet to completely solidify was found using the time given in each frame.

The JPEG images were reviewed and several were chosen to illustrate the nature of the occurrence of the freezing process of a sessile droplet. Images chosen were analyzed using ImageJ, a Java based image processing program developed by the National Institute of Health. The images were each individually opened and analyzed in ImageJ using identical procedures. Initially, a scale was set using the 'set scale…' feature in ImageJ based on any distinguishable, yet measureable, feature in the image with respect to the number of pixels within the distinguished feature. The feature chosen for this experiment was the syringe needle. Using the 'straight line' tool, a horizontal line was made across the syringe needle to reference the diameter of the needle. The syringe needle was measured with a Venier Caliper, and was found to be 1.0 mm in diameter. 'Set scale…' was found in the ImageJ toolbar under the tab labeled 'analyze'. The number of pixels within the line made earlier to reference the diameter of the syringe needle was noted after choosing 'set scale…'in ImageJ. The known distance and unit of the known distance were input into ImageJ.

A square was then made around the area of interest using the "rectangular" tool and the "clear outside" feature was then applied to the image, isolating the droplet from the original image. Next, the image was converted to black and white by adjusting the threshold of the original image. The image was converted to black and white by utilizing the "threshold" feature

in ImageJ. In the "threshold" interface, a drop down menu that represents the extremities of the color schemes used in ImageJ was changed from "red" to "B&W" which represents black and white. Converting the color scheme of the images to black and white allowed the solid content of the droplet, which appeared as black, to be clearly distinguished from the liquid content remaining within the droplet, which appeared as white. The "analyze particle" feature was then used to analyze the area of the liquid and solid content throughout the droplet. The "analyze particle" feature demonstrated a limitation in that the feature could only identify particles in their entirety. The "analyze particle" feature could not identify droplets within droplets. In the case of a droplet being encased within another droplet, ImageJ tended to only identify the properties of the black area within the images. For example, the images that consisted of a partially solidified droplet, meaning there was a visible distinction between the solid and liquid content of the droplet recognized by ImageJ, could only be analyzed as a complete solid droplet using the "analyze particle" feature.

In order to maneuver around that particular limitation, the "analyze particle" feature was first used to find the area of the entire droplet. The black and white color scheme of the droplet was inverted, causing solids to appear white and liquids to appear black. The area was then found solely for the liquid content remaining within the droplet. The solid content of the droplet was found by taking the difference between the area of the entire droplet and the area of the liquid content within the droplet. The solid and liquid content of the droplet was converted into percentages using Equations 3.10 and 3.11 respectively after the areas for the solid and liquid was determined.

$$\frac{A_{Total} - A_{Solid}}{A_{Total}} \times 100 = Percentage\ of\ Solid\ Content \tag{3.10}$$

$$\frac{A_{Total} - A_{Liquid}}{A_{Total}} \times 100 = Percentage\ of\ Liquid\ Content \tag{3.11}$$

ImageJ assumes all images uploaded into the program are two dimensional images. In order to account for that assumption being applied to the spherical sessile droplets observed in the present study, the radius of the liquid content was measured. The radius of the liquid content of the sessile droplets was determined from the area of the liquid using Equation 3.12.

$$A_{Liquid} = \pi r^2 \rightarrow r = \sqrt{\frac{A_{Liquid}}{\pi}} \tag{3.12}$$

The volume of the liquid was determined using Equation 3.13 after determining the radius of the liquid content remaining in the sessile droplet. Knowing the volume, volumetric freezing rate was then determined using Equation 3.14. The volumetric freeze rate provides a rate at which freezing is occurring in terms of volume with respect to time. The total freeze time provides the time elapsed for freezing to occur from the onset of freezing until the droplet has completely solidified. The total freeze time of the freezing process was determined using Equation 3.15.

$$V_{Liquid} = \frac{4}{3}\pi r^3 \tag{3.13}$$

$$Volumetric\ Freeze\ Rate = \frac{V_{Liquid}}{time} \tag{3.14}$$

$$Total\ Freeze\ Time = \frac{V_{Droplet}}{Volumetric\ Freeze\ Rate} \tag{3.15}$$

In addition to visualizing freezing of sessile droplets dispensed from a syringe, droplets were visualized freezing in subcooled silicone oil. Figure 30 is a schematic of the experiment setup used to visualize freezing in silicone oil. A polycarbonate test tube was filled with supercooled silicone oil and placed between a Cowboy Studio Tricolor backlight and high speed

camera. The high speed camera was set at a resolution of 1024 by 1024 and a frame rate of 125 frames per second. Water droplets were dispensed into the supercooled silicone oil using a 0.5 mL syringe. Water droplets were visualized freezing in supercooled silicone oil in an effort to determine a homogeneous nucleation freezing process.

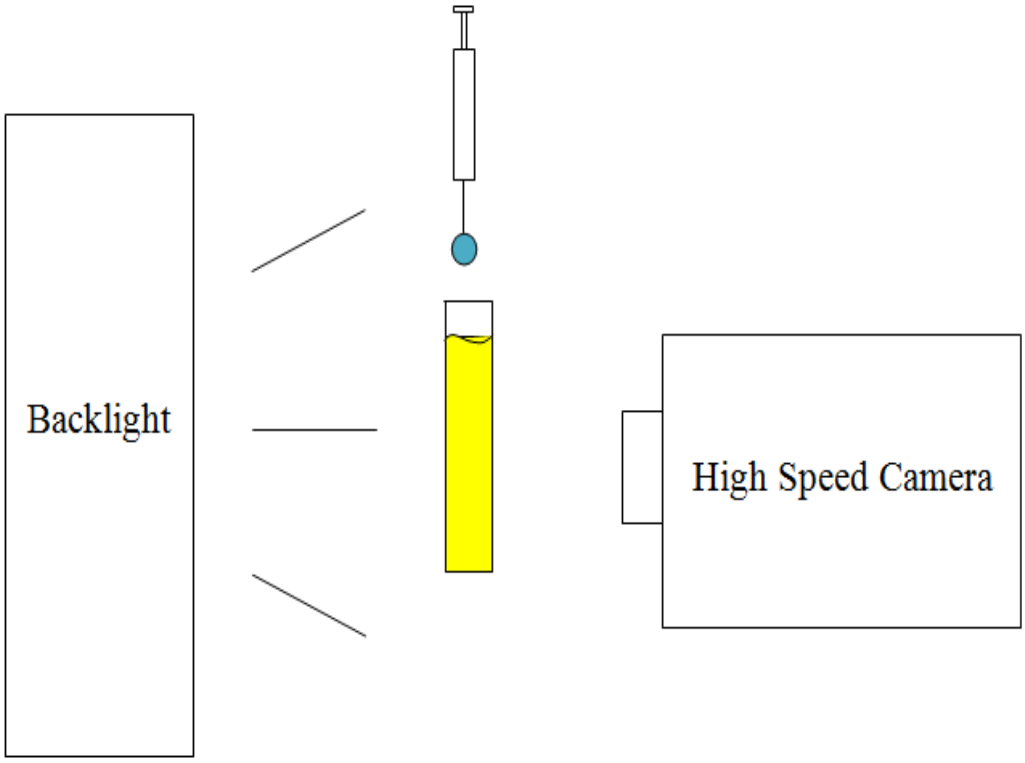

Figure 30. Schematic of the experiment setup used to visualize freezing in silicone oil.

3.4. Heat Transfer Lumped System Analysis

Lumped system analysis was done in order to determine the rate of heat transfer of the sessile droplet when placed in the environmental chamber numerically. Figure 31 is a schematic of the condition that were simulated using the heat transfer lumped system analysis. A spherical liquid droplet was exposed to a subcooled surrounding temperature, T_∞. The temperature distribution around the spherical droplet is assumed to be equal. As the surrounding temperature

begins to influence the temperature of the droplet by means of convection, heat flux is loss. The heat transfer process between the droplet and the surrounding temperature is dependent on the thermal conductivity, *k*, density, ρ, and specific heat, *c* of the liquid droplet.

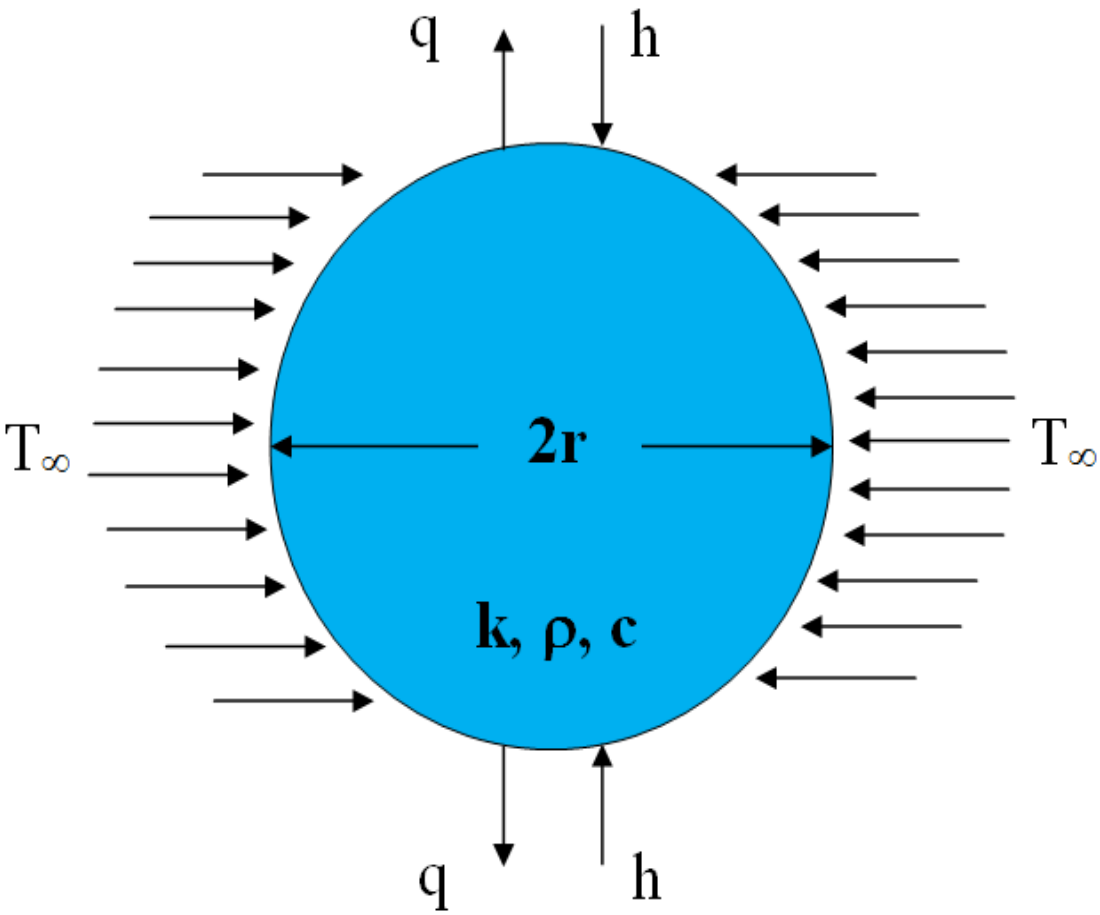

Figure 31. Schematic of the condition simulated using heat transfer lumped system analysis.

Prior to conducting the heat transfer lumped system analysis, an experiment was conducted to measure the convective heat transfer coefficient, *h*. Figure 32 is a schematic of the experimental setup used to measure the convective heat transfer coefficient. A heater cartridge connected to a power supply was placed into the subcooled environmental chamber. The power supply allowed for the input of a known voltage and current to be applied to the heater cartridge.

The surrounding temperature and the temperature of the heater cartridge was monitored by a data acquisition system equipped with K-type thermocouples.

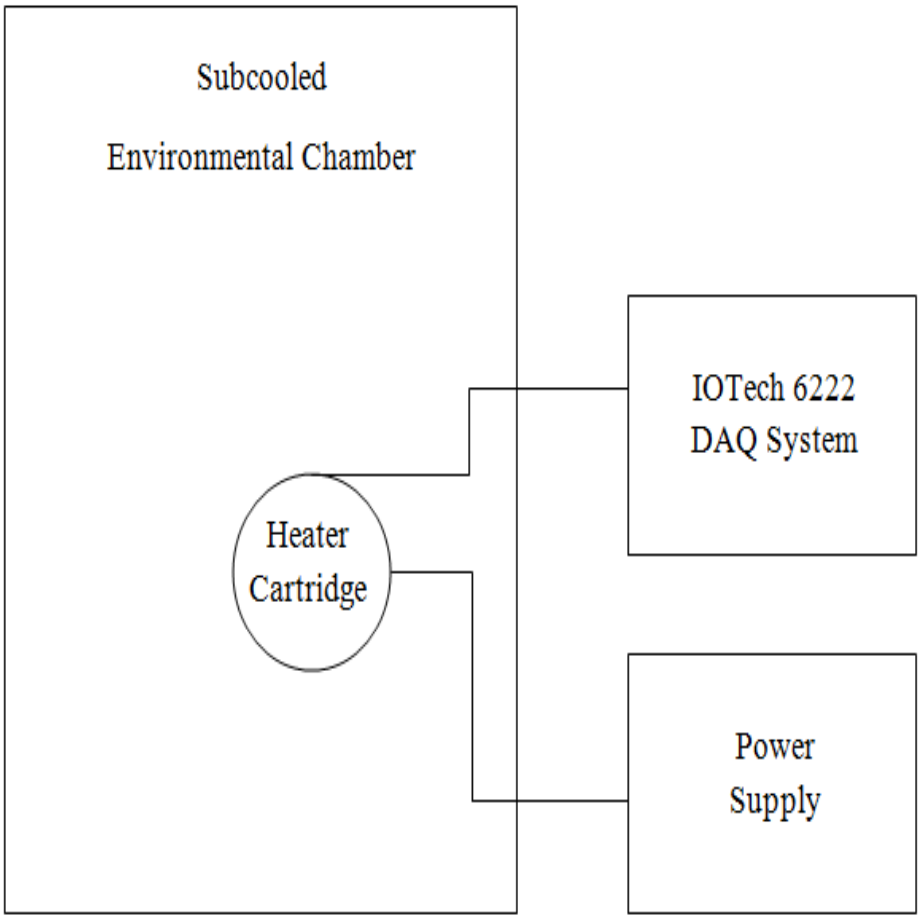

Figure 32. Schematic of the experimental setup used to measure the convective heat transfer coefficient.

The environmental chamber was subcooled to -40°C. The heater cartridge was used to introduce the subcooled conditions within the environmental chamber with heat flux in order to meet the conditions of Newton's Law of Cooling, which states that

$$q = -h(T_o - T_\infty) \qquad (3.16)$$

where q is the heat flux, T_o is the temperature of the heater cartridge, and T_∞ is the constant temperature within the environmental chamber. The heater cartridge was connected to a 6030A System Power Supply, which was set to 5.0 volts and 1.0 amperes, and placed inside the environmental chamber where it was then allowed to heat. The temperature of the heater cartridge was monitored using an IOTech Data Acquisition System, series number 6222. The temperature of the heater cartridge was observed until the temperature plateaued, which was rounded to the nearest whole number and recorded. The primary component of the heater cartridges that were contributing heat into the environmental chamber were four cylindrical prongs, each of identical size. The 6030A System Power Supply was then powered off, and the heater cartridge was removed from the 6030A System Power Supply and allowed to cool to room temperature. The diameter and height of cylindrical prongs were measured using a Vernier caliper and found to be 0.00635 m and 0.060 m, respectively. Knowing the diameter, *d*, and in turn, the radius, *r*, and the height, *h*, of the cylindrical prongs, the area of the prongs, *A*, was found using the following equation,

$$2\pi r(r + h) = A. \tag{3.17}$$

Heat flux is watts per unit area, thus knowing the area of each prong and the voltage and current that the system was operating under, it was possible to calculate heat flux using this experimental setup. Heat flux was calculated using the following equation,

$$\frac{iV}{4A} = \frac{P}{4A} = q \tag{3.18}$$

where *i* is current, *V* is voltage, and *P* represents power, which is the product of the current multiplied by the voltage. Recalling Equation 3.16, after calculating the heat flux, Newton's Law of Cooling can then be applied to determine the convective heat transfer coefficient, *h*, of the operating system within the environmental chamber, with *h* being the only unknown.

Knowing the convective heat transfer coefficient, the Biot number for the sessile droplet inside of the environmental chamber was then calculated. The Biot number numerically describes temperature distribution throughout a system during transient heating or cooling processes, assuming that the temperature distribution is uniform throughout the system. Lumped system analysis can only be performed on a system if the Biot number of the system is less than 0.1. The Biot number, *Bi*, is given by

$$\frac{h\left(V/A_s\right)}{k} = \frac{hL_c}{k} = Bi < 0.1 \tag{3.19}$$

where V is volume, A_s is the surface area of the sessile droplet, k is the thermal conductivity coefficient, and L_c is the characteristic length. The thermal conductivity of water was found in literature to be 0.613 W/m·K at room temperature (Cengel & Boles, 2008; Gieck & Gieck, 2006). The sessile droplet was assumed to be a sphere, thus the characteristic length was given by

$$\frac{V}{A_s} = \frac{\frac{4}{3}\pi r^3}{4\pi r^2} = \frac{r}{3} = L_c. \tag{3.20}$$

The radius of the sessile droplet, r, was determined by analyzing JPEG images captured by the high speed camera using ImageJ. Similarly to the experiment in section 3.3, an image was opened in ImageJ and a scale was set using the 'set scale…' feature based on any distinguishable, yet measureable, feature in the image with respect to the number of pixels within the distinguished feature. The feature chosen for this experiment was the syringe needle. Using the 'straight line' tool, a horizontal line was made across the syringe needle to reference the diameter of the needle. The syringe needle was measured with a Venier Caliper, and was found to be 1.0 mm in diameter. 'Set scale…' was found in the ImageJ toolbar under the tab labeled

'analyze'. The number of pixels within the line made earlier to reference the diameter of the syringe needle was noted after choosing 'set scale…' in ImageJ. The known distance and unit of the known distance were input into ImageJ.

Another horizontal line was then made across the widest portion of the sessile droplet, which was typically located at the midsection of the sessile droplet. The "measure" feature was then utilized to determine the length of the newly drawn line based on the scale that was previously set. The length that was measured by ImageJ using the "measure" feature served as the diameter of the sessile droplet. The radius of the sessile droplet was then used to obtain the characteristic length of the sessile droplet. The Biot number was then calculated using Equation 3.19. Once confirmed that the Biot number of the system was less than 0.1, the Fourier number was calculated. The Fourier number describes the magnitude of the effects of the degree of cooling or heating within a system, and was obtained using the following equation

$$Fo = \frac{\alpha t}{{L_c}^2} \tag{3.21}$$

where α is thermal diffusivity and t is time. Time, t, was obtained from the images taken by the high speed camera. Each frame recorded by the high speed camera was marked with a time stamp which indicated when a particular event occur based on the frame rate at which the images were taken. Thermal diffusivity is a thermophysical property the represents the rate at which heat is capable of diffusing through a medium. The larger the thermal diffusivity, the faster heat will diffuse through a medium. The thermal diffusivity is given by

$$\alpha = \frac{k}{\rho c} \tag{3.22}$$

where ρ is the density and c is the specific heat. The density and specific heat of water has been reported throughout literature to be 1000 kg/m^3 and 4.22 kJ/kg·K, respectively (Cengel & Boles,

2008). The Fourier number can then be calculated using Equation 3.21 after calculating the thermal diffusivity. A heat transfer lumped system analysis can then be performed by applying the following equation,

$$\frac{T(t)-T_\infty}{T_i-T_\infty} = e^{-\left({}^{hL_c}/_{k}\right)\left({}^{\alpha t}/_{{L_c}^2}\right)} = e^{-BiFo} \qquad (3.23)$$

where T_∞ is the temperature within the environmental chamber, T_i is the initial temperature of the droplet, which in case was room temperature, *T(t)* is temperature with respect to time and *t* is time. Time, *t*, was obtained from the images taken by the high speed camera. Each frame recorded by the high speed camera was marked with a time stamp which indicated when a particular event occurred based on the frame rate at which the images were taken. *T(t)* was the only unknown term in Equation 3.23 and the term of interest in this analysis. Therefore Equation 3.23 was rewritten as

$$T(t) = e^{-BiFo}(T_i - T_\infty) - T_\infty. \qquad (3.24)$$

All of the terms in Equation 3.24 were constant, with the exception of time, *t*, and *T(t)* which is a function of time. Equation 3.24 was written, solved and plotted using MATLAB, a computer programming language used for numerical computing.

Table 2 presents the results from a temporal independent study performed on the MATLAB code written for the heat transfer lumped system analysis. A temporal independent study was performed in order to determine an optimum time step to operate the heat transfer lumped system code in which the time step did not have a significant effect on the results. The temporal independent study was performed at time steps of 10, 1, 0.1, 0.01, and 0.001 seconds. Time for the system to reach -40°C was observed to increase from 3.48 to 3.486 seconds

between time steps of 0.01 and 0.001, respectively, thus 0.01 was the time step used in the present study to conduct the lumped system analysis.

Table 2

Results of a temporal independent study performed on the code written for heat transfer lumped system analysis.

Δt, s	Time, s (to reach -40°C)
10	10
1	4
0.1	3.50
0.01	3.48
0.001	3.486

CHAPTER 4

Results

The following chapter will begin by presenting the results of the shear stress tests. The shear stress tests were conducted on bare aluminum at -5, -10, -20, and -30°C. Experiments were also conducted on methoxymethylethoxypropanol, polymethylhydrosiloxane, and octylphenol ethoxylate treated aluminum, stainless steel, copper, and polycarbonate substrates at -10°C. An additional experiment was conducted on bare aluminum, stainless steel, copper, and polycarbonate substrates to determine a baseline of the adhesive strength of ice in the present study. The current chapter will then present the results obtained from measuring the contact angles of sessile droplets on bare and methoxymethylethoxypropanol, polymethylhydrosiloxane, and octylphenol ethoxylate treated aluminum, stainless steel, copper, and polycarbonate substrates. Next, the results of the images taken using shadowgraphing will be presented. Finally, the results of the heat transfer lumped system analysis on the sessile droplet exposed to subcooled conditions will be presented and compared to the results observed while using shadowgraphing to view freezing in a sessile droplet and the rate at which freezing occurs.

4.1. Adhesive Strength of Ice on Various Substrates at Subcooled Temperatures

Shear stress tests were conducted to determine the adhesive strength of ice to substrates chosen to simulate materials used on aircraft structures. Prior to testing the adhesive strength of ice to methoxymethylethoxypropanol, polymethylhydrosiloxane, and octylphenol ethoxylate treated aluminum, stainless steel, copper, and polycarbonate substrates, shear stress tested were conducted on bare aluminum at -5, -10, -20, and -30°C to determine whether temperature had an effect on the adhesive strength of ice. The raw data measured for all of the shear stress tests conducted in the present study are presented in the appendices. Figure 33 and Table A-1

displays the results from the shear stress tests conducted on bare aluminum at -5, -10, -20, and -30°C. 30 trials were conducted at each temperature. As Fortin et al. (2010) stated, there is a large range and variation in the reported adhesive strength data throughout literature making it difficult to quantify the adhesive strength of ice with an absolute value, and the data presented in Figure 33 and Table A-1 are nothing short of that statement. The data measured throughout the current adhesive strength test and other variations of the experiment in the present study were scattered. There was never any certain absolute value that could be assigned to represent the adhesive strength of ice.

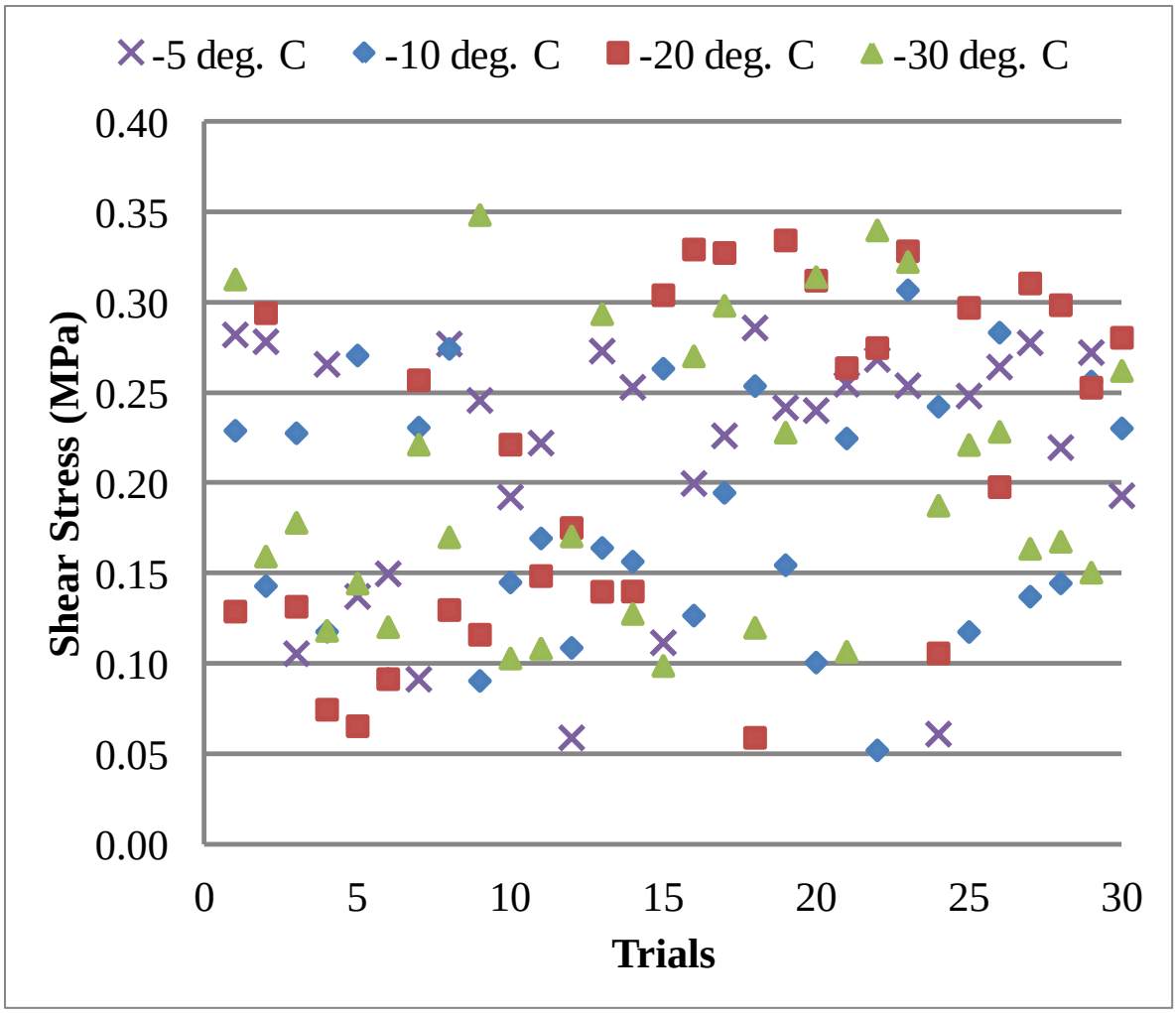

Figure 33. Adhesive strength of ice on bare aluminum at -5, -10, -20, and -30°C.

Table 3 presents a summary of the average, standard deviation, and uncertainty analysis of the data collected from the adhesive strength tests conducted on bare aluminum at various subcooled temperatures. Table 3 reveals that temperature had very little effect on the average adhesive strength of ice to aluminum substrates. The average adhesive strength was measured to be 0.215±0.031 MPa at -5°C. The average adhesive strength of ice measured at -10°C was 0.184±0.031 MPa, decreasing compared to the average adhesive strength measured at -5°C. The average adhesive strength at -20°C was measured to be 0.215±0.041 MPa, increasing compared to the 0.184±0.031 MPa measured at -10°C. The average adhesive strength was measured to be 0.202±0.035 MPa at -30°C, decreasing compared to the 0.213±0.041 MPa measured at -20°C.

Table 3

Summary of the adhesive strength of ice on bare aluminum at -5, -10, -20, and -30 ℃.

Temperature	Average Shear Stress (MPa)	Standard Deviation	Random Standard Uncertainty	Random Uncertainty (95% Confidence)
-5°C	0.215	0.070	0.013	0.031
-10°C	0.184	0.070	0.013	0.031
-20°C	0.213	0.094	0.017	0.041
-30°C	0.202	0.08	0.015	0.035

Though the data in Figure 33 and Table A-1 appear scattered, there was very little deviation in the in the average adhesive strength of the data collected at -5, -10, -20, and -30°C, which can be observed in Table 3. The average adhesive strength of ice measured on aluminum

at -5, -10, -20, and -30°C, suggests that the adhesive strength of ice is not dependent on temperature.

Once it was determined that the adhesive strength of ice was not dependent on temperature, the remaining shear stress tests were conducted at -10°C, and instead of 30 trials, eight trials were performed for each substrate and surface modification. Figure 34 shows the average adhesive strength of the shear stress of ice on bare stainless steel, copper, and polycarbonate substrates at -10°C from the data presented in Table A-2. The results suggest that ice measured the highest adhesive strengths on the copper substrates, and the lowest adhesive strengths on the aluminum substrates.

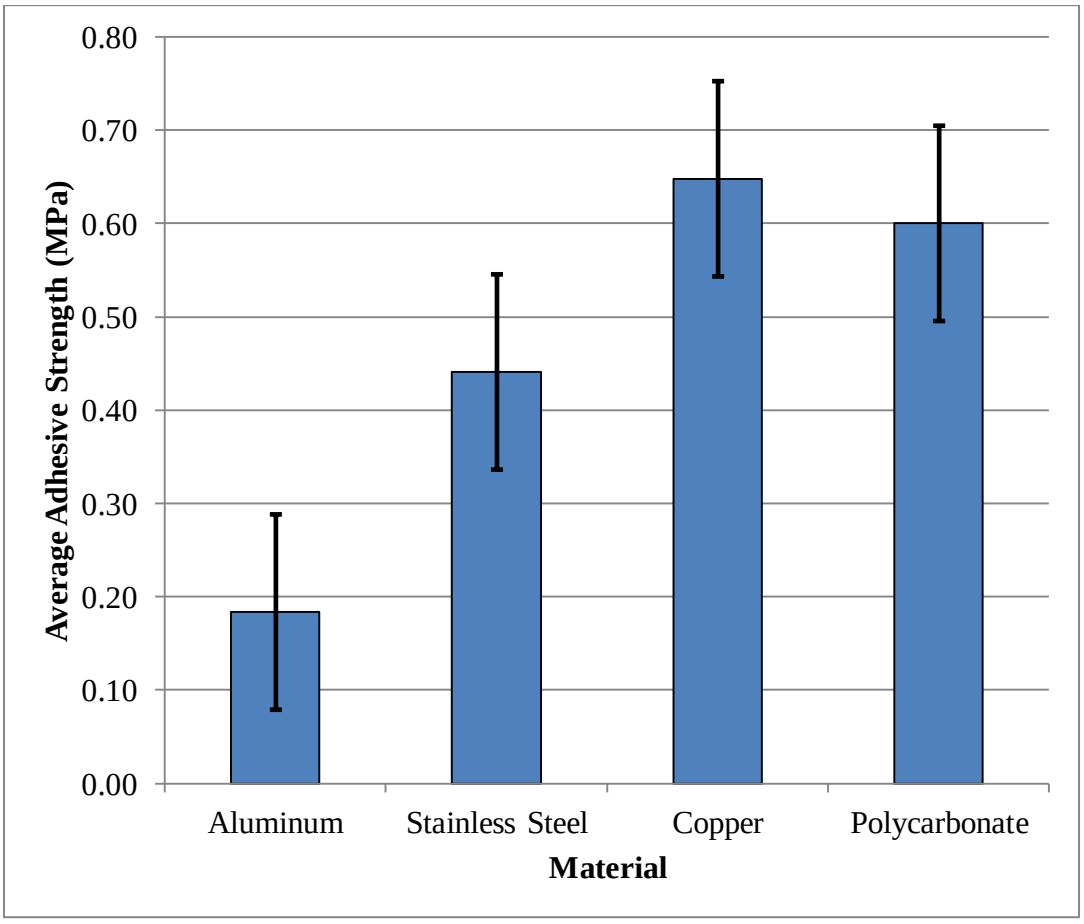

Figure 34. Average adhesive strength of ice on bare substrates.

Table 4 presents the average, standard deviation, and uncertainty analysis of the data shown in Table A-2. The values in Table 4 correspond with the data measured from the adhesive strength tests conducted on bare aluminum, copper, stainless steel, and polycarbonate at -10°C. The results reveal that the average adhesive strength of ice was most significant on bare copper than it was on aluminum, stainless steel, and polycarbonate. Table 4 also reveals that there was a relatively larger variation in the adhesive strength of ice on copper, which was determined from the standard deviation calculated. The average adhesive strength of stainless steel was measured to be 0.441±0.035 MPa, which agrees well with the average adhesive strength of 0.480 MPa reported by Jellinek et al. (1981). The average adhesive strength of ice on bare aluminum was measured to be the least of the materials used throughout the present study.

Table 4

Summary of the adhesive strength of ice on bare substrates.

Material	Average Shear Stress (MPa)	Standard Deviation	Random Standard Uncertainty	Random Uncertainty (95% Confidence)
Aluminum	0.184	0.069	0.013	0.031
Stainless Steel	0.441	0.041	0.014	0.035
Copper	0.648	0.182	0.064	0.156
Polycarbonate	0.600	0.094	0.033	0.080

Figure 35 presents the average adhesive strength of ice on methoxymethylethoxypropanol treated aluminum, stainless steel, copper, and polycarbonate substrates at -10°C from the data shown in Table A-3. Methoxymethylethoxypropanol is a chemical that is advertised in industry to operate as water repellant. Figure 35 suggests that the methoxymethylethoxypropanol

treatment increased the adhesive strength of ice on all of the substrates observed in the present study. Similar to the results measured on the adhesive strength of ice to the bare substrates, copper was measured to demonstrate the highest average adhesive strength after being treated with methoxymethylethoxypropanol. Aluminum demonstrated the lowest average adhesive strength after being treated with methoxymethylethoxypropanol.

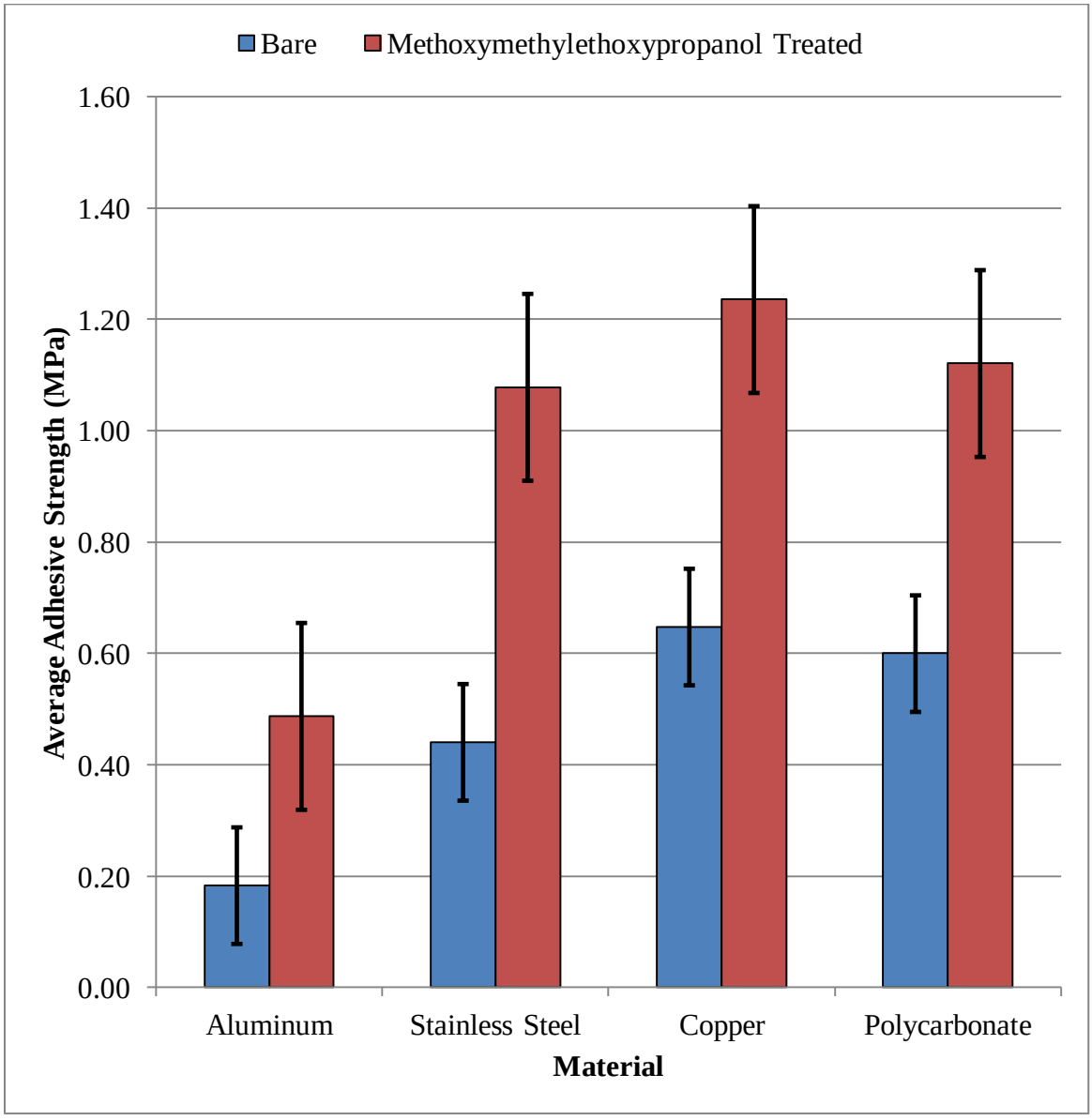

Figure 35. Average adhesive strength of ice on methoxymethylethoxypropanol treated substrates.

Table 5 presents the average, standard deviation, and uncertainty analysis of the data presented in Table A-3. The values in Table 5 correspond with the data measured from the adhesive strength tests conducted on methoxymethylethoxypropanol treated substrates. Aluminum was measured to have the lowest adhesive strength values compared to the remaining substrates observed in the present study, while copper was measured to have the highest adhesive strength values. Aluminum measured an average adhesive strength of 0.487±0.069 MPa, while the stainless steel, copper, and polycarbonate substrates measured average adhesive strengths of 1.078±0.058, 1.236±0.060, and 1.121±0.135 MPa respectively.

Table 5

Summary of the adhesive strength of ice on methoxymethylethoxypropanol treated substrates.

Material	Average Shear Stress (MPa)	Standard Deviation	Random Standard Uncertainty	Random Uncertainty (95% Confidence)
Aluminum	0.487	0.081	0.029	0.069
Stainless Steel	1.078	0.067	0.024	0.058
Copper	1.236	0.070	0.025	0.060
Polycarbonate	1.121	0.158	0.056	0.135

Table 6 presents the adhesion reduction factor, ARF, and percent difference of the average adhesive strengths measured on methoxymethylethoxypropanol treated substrates. The ARF compares the average shear stress measured on treated substrates to the average shear stress measured for bare substrates. A bare beam would have an ARF of one, while numbers less than one would indicate an increase in the adhesive strength of ice on a substrate, and numbers larger than one would indicate a decrease in the adhesive strength of ice. Table 6 reveals that the

methoxymethylethoxypropanol treatment increased the adhesive strength of ice on all of the substrates observed in the present study. The adhesive strength of ice to aluminum, stainless steel, copper, and polycarbonate increased by 165.60%, 144.60%, 90.77%, and 86.80% respectively. From the results in Table 6, it can be concluded that methoxymethylethoxypropanol, a chemical advertised to repel water, does not necessarily repel icing.

Table 6

ARF and percent difference of methoxymethylethoxypropanol treated substrates.

Methoxymethylethoxypropanol			
Material	Average Shear Strength	ARF	Percent Difference (%)
Aluminum	0.487	0.38	165.60
Stainless Steel	1.078	0.41	144.60
Copper	1.236	0.52	90.77
Polycarbonate	1.121	0.54	86.80

Figure 36 presents the average adhesive strength of ice on polymethylhydrosiloxane treated aluminum, stainless steel, copper, and polycarbonate substrates at -10°C from the data presented in Table A-4. Figure 36 reveals that the polymethylhydrosiloxane treatment increased the adhesive strength of ice on the copper substrates the most compared to the remaining substrates observed in the present study. The adhesive strength of ice measured on the metallic substrates was measured to have increased. However, the adhesive strength of ice was reduced on polymethylhydrosiloxane treated polycarbonate. Similar to the results measured on the adhesive strength of ice to the bare substrates, copper was measured to demonstrate the highest

average adhesive strength after being treated with polymethylhydrosiloxane. Aluminum demonstrated the lowest average adhesive strength after being treated with polymethylhydrosiloxane.

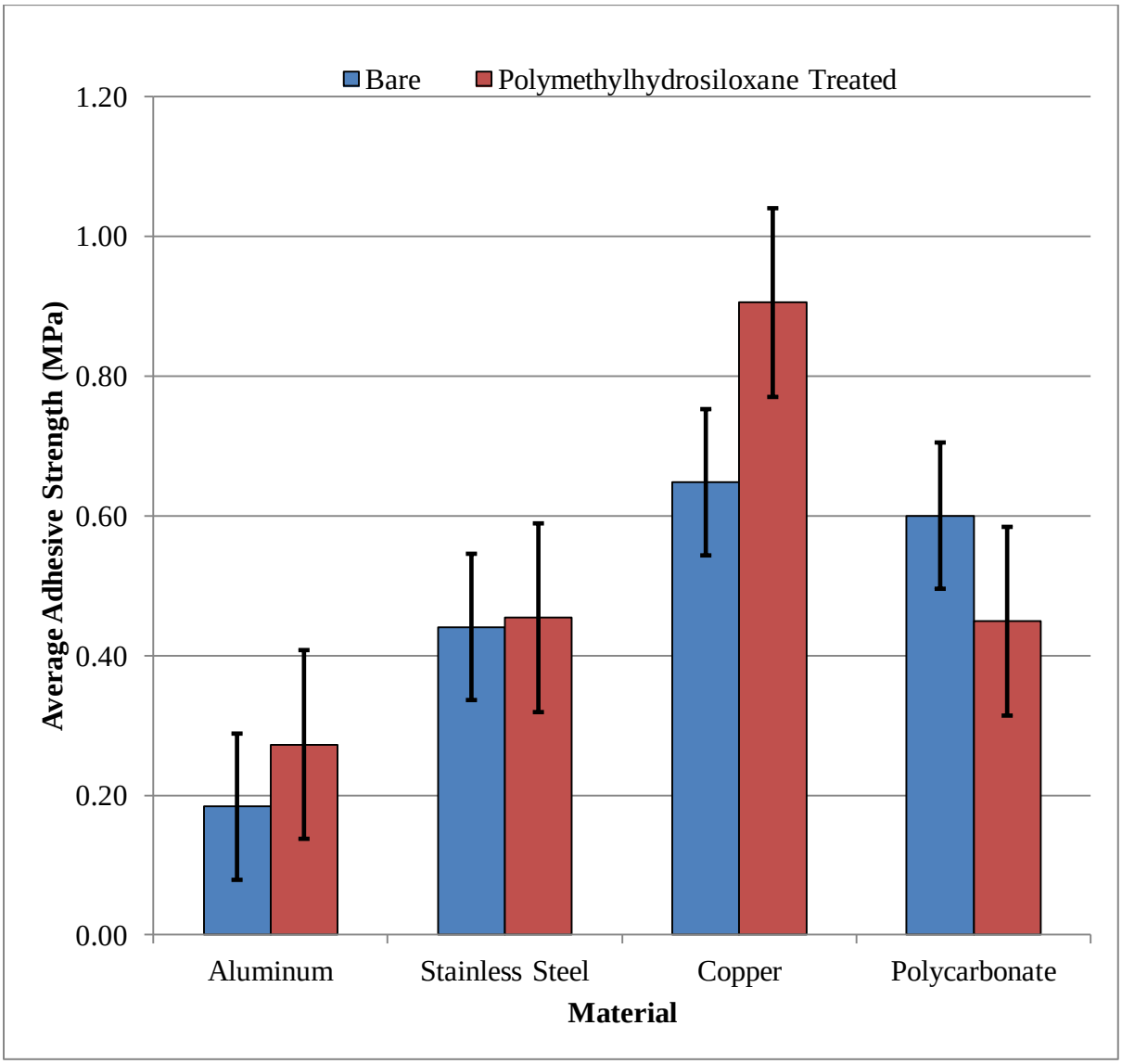

Figure 36. Average adhesive strength of ice on polymethylhydrosiloxane treated substrates.

Table 7 presents the average, standard deviation, and uncertainty analysis of the data presented in Table A-4. The results reveal the average adhesive strength of ice on the polymethylhydrosiloxane treated copper was greatest compared to the remaining substrates

observed in the present study. The average adhesive strength of ice measured on polymethylhydrosiloxane treated copper was 0.905±0.189 MPa. Polymethylhydrosiloxane treated aluminum measured the lowest average adhesive strength of the substrates observed in the present study, averaging at 0.273±0.039 MPa.

Table 7

Summary of the adhesive strength of ice on polymethylhydrosiloxane substrates.

Material	Average Shear Stress (MPa)	Standard Deviation	Random Standard Uncertainty	Random Uncertainty (95% Confidence)
Aluminum	0.273	0.046	0.016	0.039
Stainless Steel	0.454	0.184	0.065	0.158
Copper	0.905	0.221	0.078	0.189
Polycarbonate	0.449	0.090	0.032	0.077

Table 8 presents the ARF and percent difference of the of the average adhesive strengths measured on polymethylhydrosiloxane treated substrates. Table 8 reveals that the polymethylhydrosiloxane surface treatment increased the adhesive strength of ice on all of the substrates except for the polycarbonate. The polymethylhydrosiloxane surface treatment increased the adhesive strength of ice on aluminum, stainless steel, and copper by 48.55%, 2.97%, and 39.69% respectively. The polymethylhydrosiloxane surface treatment reduced the average adhesive strength of ice on the polycarbonate substrates by 25.19%. Physically, polymethylhydrosiloxane possesses an oily consistency. During the experiments, it was observed that while in the environmental chamber, the polymethylhydrosiloxane had completely dissipated on the metal substrates. However, the polymethylhydrosiloxane remained present on

the polycarbonate throughout the present study. The presence of the treatment on the substrate could be due to the polycarbonate possessing insulating capabilities, which reduces the rate of heat tranfer of the surrounding temperatures within the environmental chamber through the substrate, and in turn, the rate of dissipation of the polymethylhydrosiloxane surface treatment.

Table 8

ARF and percent difference of polymethylhydrosiloxane treated substrates.

Polymethylhydrosiloxane			
Material	Average Shear Strength	ARF	Percent Difference
Aluminum	0.273	0.67	48.55
Stainless Steel	0.454	0.97	2.97
Copper	0.905	0.72	39.69
Polycarbonate	0.449	1.34	-25.19

Figure 37 presents the average adhesive strength of ice on octylphenol ethoxylate treated aluminum, stainless steel, copper, and polycarbonate substrates at -10°C from the data presented in Table A-5. Octylphenol ethoxylate was observed to reduce the average adhesive strength of ice on all of the substrates observed in the present study. As with the previous values measured, ice displayed the highest average adhesive strength on copper substrates and the lowest average adhesive strength on aluminum. Octylphenol ethoxylate was the only surfactant used in the present study measured to reduce the adhesive strength of all substrates. The characteristics demonstrated by the octylphenol ethoxylate to reduce the adhesive strength of ice on aluminum, stainless steel, copper, and polycarbonate are characteristics desired in order reduce the adhesive strength of ice on aircraft structures.

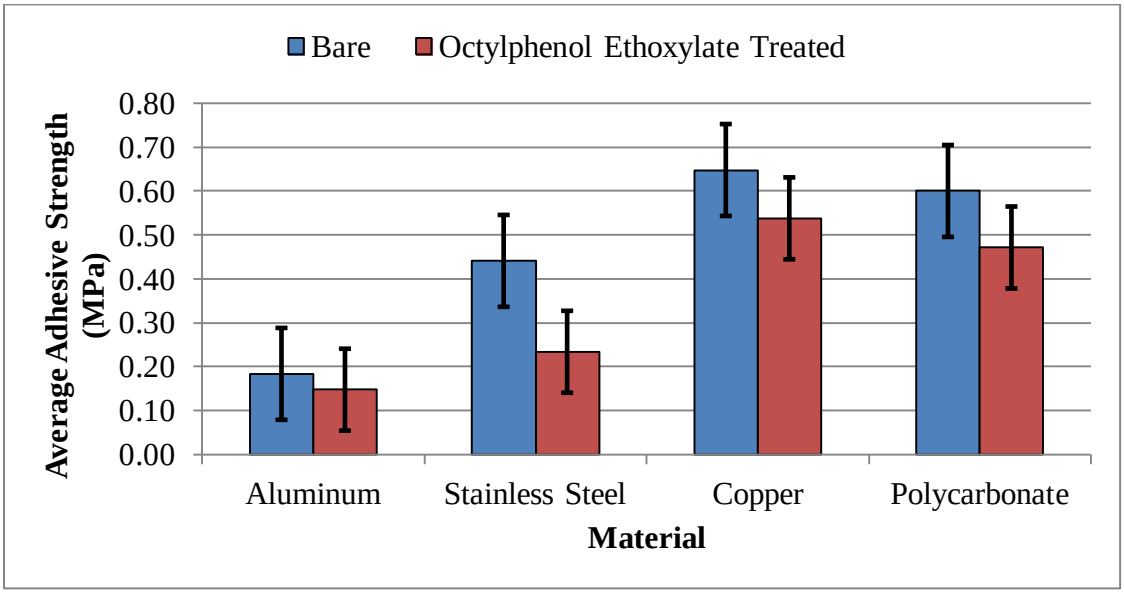

Figure 37. Average adhesive strength of ice on octylphenol ethoxylate treated substrates.

Table 9 presents the average, standard deviation, and uncertainty analysis of the data presented in Table A-5. The highest average adhesive strength was measured on the copper substrates. The average adhesive strength of ice measured on octylphenol ethoxylate treated aluminum, stainless steel, copper, and polycarbonate was measured to be 0.147±0.092, 0.234±0.091, 0.538±0.064, and 0.471±0.178 MPa respectively.

Table 9

Summary of the adhesive strength of ice on octylphenol ethoxylate treated substrates.

Material	Average Shear Stress (MPa)	Standard Deviation	Random Standard Uncertainty	Random Uncertainty (95% Confidence)
Aluminum	0.147	0.107	0.038	0.092
Stainless Steel	0.234	0.107	0.038	0.091
Copper	0.538	0.074	0.026	0.064
Polycarbonate	0.471	0.208	0.074	0.178

Table 14 presents the ARF and percent difference of the shear stress tests performed on the octylphenol ethoxylate treated substrates. Table 14 reveals that the octylphenol ethoxylate surface treatment reduced the adhesive strength of all substrates observed in the present study. The ARF values calculated indicate that the adhesive strength of ice was reduced on all of the substrates observed in the present study. Octylphenol ethoxylate reduced the adhesive strength of ice most effectively on stainless steel, and least effectively on copper. The adhesive strength of ice was reduced by 19.64% on aluminum, 46.97% on stainless steel, 17% on copper, and 21.45% on polycarbonate.

Table 10

ARF and percent difference of the octylphenol ethoxylate treated substrates.

Octylphenol Ethoxylate			
Material	Average Shear Strength	ARF	Percent Difference
Aluminum	0.147	1.24	-19.64
Stainless Steel	0.234	1.89	-46.97
Copper	0.538	1.20	-17.00
Polycarbonate	0.471	1.27	-21.45

Figure 38 presents the average adhesive strength of ice on all variations of the aluminum substrates observed in the present study at -10°C. The raw data for the averages presented in Figure 38 is shown in Table A-6. Figure 38 reveals that methoxymethylethoxypropanol treated aluminum demonstrated the highest average adhesive strength compared to all variations of aluminum observed in the present study. Polymethylhydrosiloxane and methoxymethylethoxypropanol was measured to have increased the average adhesive strength of

ice on aluminum. Octylphenol ethoxylate was the only surfactant observed in the present study that reduced the adhesive strength of ice on aluminum.

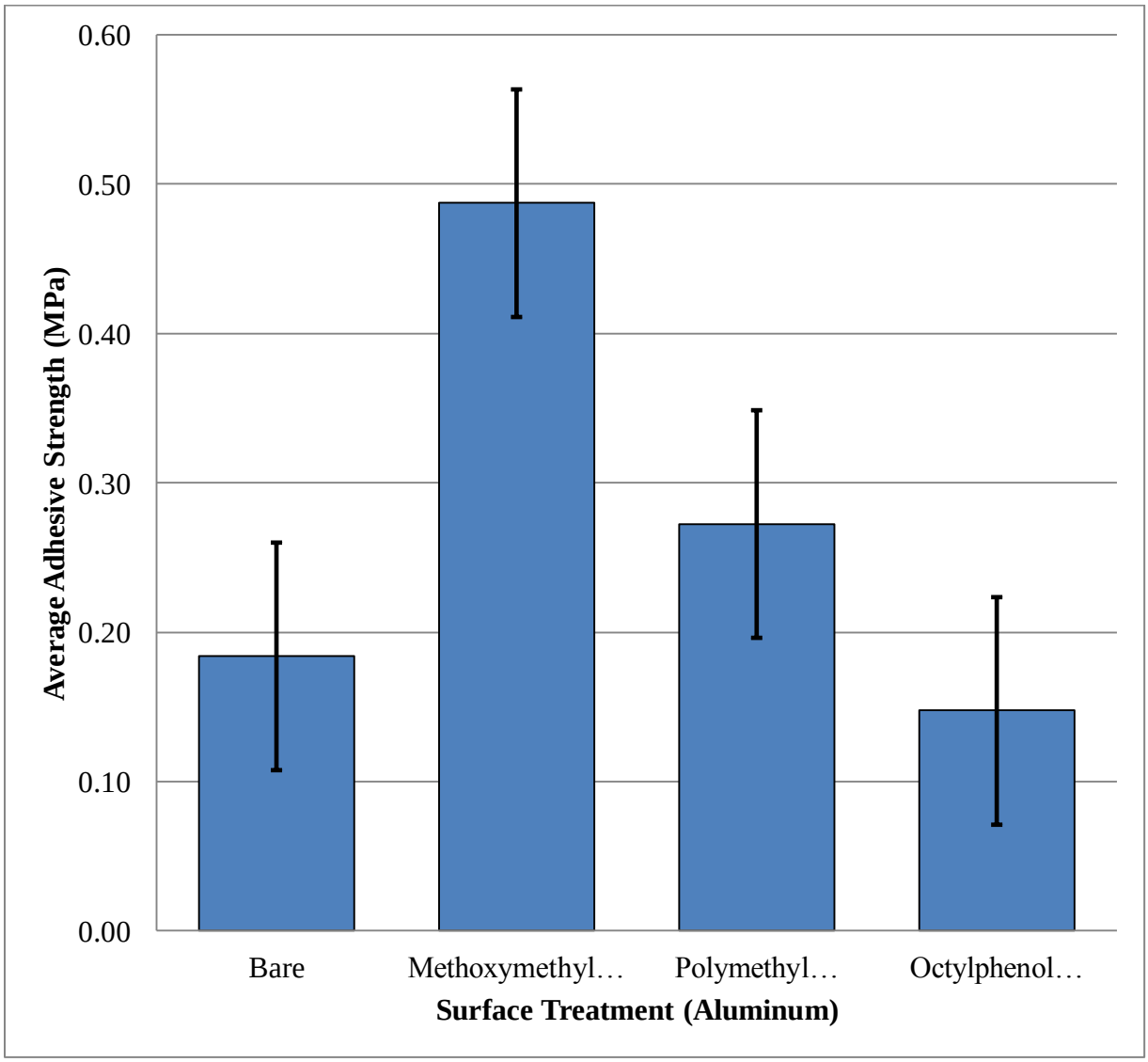

Figure 38. Average adhesive strength of ice on the variations of aluminum substrates.

Table 11 presents the average adhesive strength of ice on all variations of aluminum observed in the present study. The raw data for the values expressed in Table 11 are presented in Table A-6. The octylphenol ethoxylate was the only surfactant used in the present study that reduced the adhesive strength of ice on aluminum. Methoxymethylethoxypropanol was

measured to have increased the average adhesive strength of ice on aluminum the greatest of all of the surfactants observed in the present study. The methoxymethylethoxypropanol and polymethylhydrosiloxane surface treatments both increased the adhesive strength of ice on the aluminum substrates. Bare aluminum measured an average adhesive strength of 0.184±0.059 MPa. Methoxymethylethoxypropanol, polymethylhydrosiloxane, and octylphenol ethoxylate treated aluminum measured an average adhesive strength of 0.487±0.069, 0.273±0.039, and 0.147±0.092 MPa, respectively.

Table 11

Summary of the average adhesive strength of ice on all variations of aluminum substrates.

Aluminum	Average Shear Stress (MPa)	Standard Deviation	Random Standard Uncertainty	Random Uncertainty (95% Confidence)
Bare	0.184	0.069	0.024	0.059
Methoxymeth…	0.487	0.081	0.029	0.069
Polymethyl…	0.273	0.046	0.016	0.039
Octylphenol…	0.147	0.107	0.038	0.092

Table 12 presents the ARF and percent difference of the average adhesive strength of ice on all variations of the aluminum substrates observed in the present study. The ARF values indicate an increase in the adhesive strength of ice to aluminum substrates treated with methoxymethylethoxypropanol and polymethylhydrosiloxane. The ARF also indicates a decrease in the adhesive strength of ice on aluminum substrates treated with octylphenol ethoxylate. The methoxymethylethoxypropanol treatment was measured the highest average adhesive strength of all of the surfactants observed in the present study. The

methoxymethylethoxypropanol and polymethylhydrosiloxane surface treatments increased the adhesive strength of ice on aluminum by 165.60% and 48.55% respectively. The octylphenol ethoxylate reduced the adhesive strength of ice by 19.64%.

Table 12

ARF and percent difference of all variations of aluminum substrates.

Aluminum			
Surface Treatment	Average Shear Strength (MPa)	ARF	Percent Difference
Bare	0.184	1	N/A
Methoxymethylethoxypropanol	0.487	0.38	165.60
Polymethylhydrosiloxane	0.273	0.67	48.55
Octylphenol Ethoxylate	0.147	1.24	-19.64

Figure 39 presents the average adhesive strength of ice on all variations of the stainless steel substrates observed in the present study at -10°C. The raw data for the averages presented in Figure 39 is shown in Table A-7. Figure 39 reveals that methoxymethylethoxypropanol treated stainless steel demonstrated the highest average adhesive strength compared to all variations of stainless steel observed in the present study. Similar to the results observed on the aluminum substrates, polymethylhydrosiloxane and methoxymethylethoxypropanol was measured to have increased the average adhesive strength of ice on stainless steel. Polymethylhydrosiloxane treated stainless steel measured an average adhesive strength approximately equivalent to the average adhesive strength measured on bare stainless steel.

Octylphenol ethoxylate was the only surfactant observed in the present study that reduced the adhesive strength of ice on stainless steel.

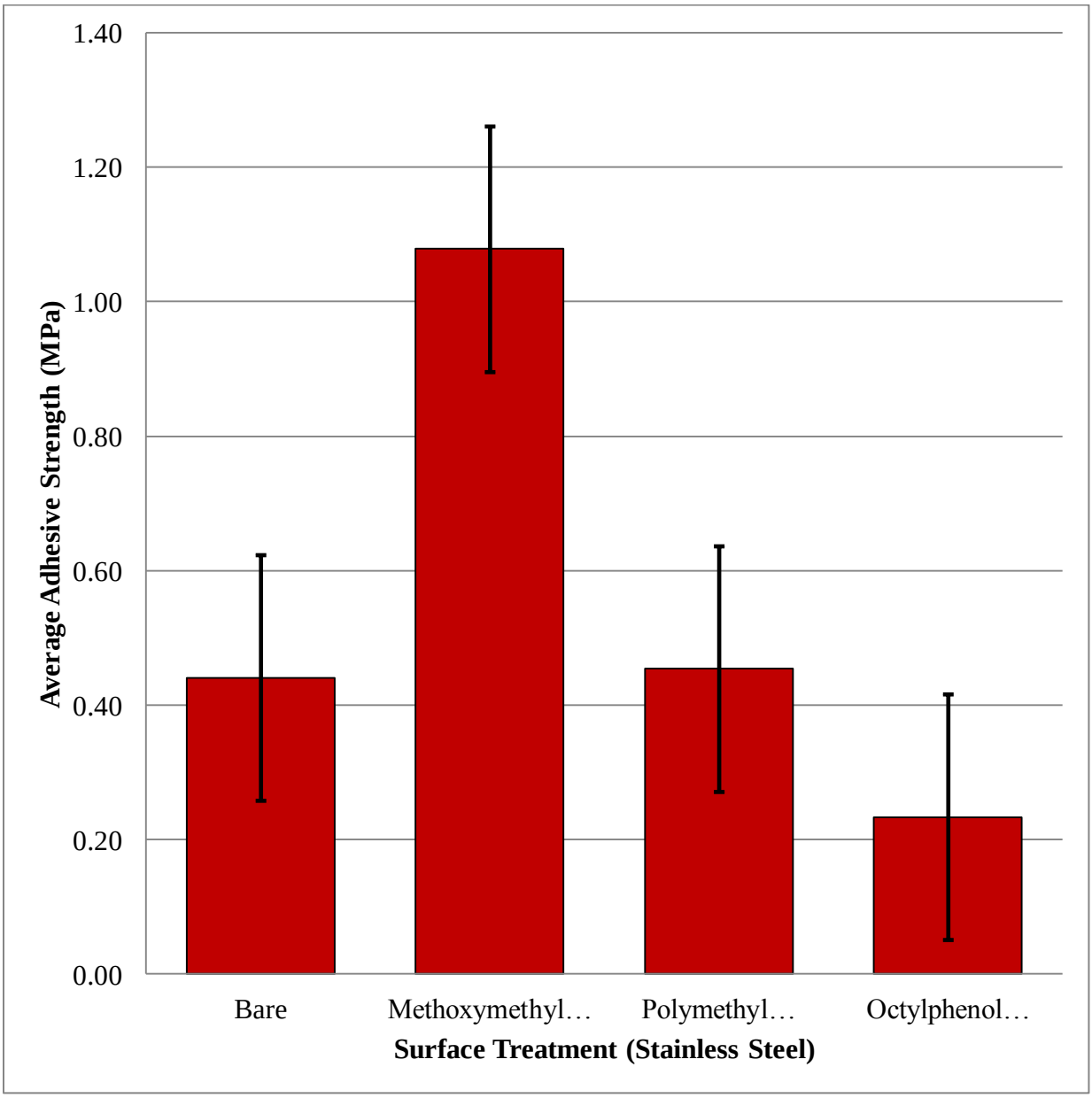

Figure 39. Average adhesive strength of ice on the variations of stainless steel substrates.

Table 13 presents the average adhesive strength of ice on all variations of stainless steel. The raw data for the values expressed in Table 13 are presented in Table A-7. Octylphenol ethoxylate was the only surfactant used in the present study that reduced the adhesive strength of

ice on stainless steel. The methoxymethylethoxypropanol and polymethylhydrosiloxane surface treatments increased the adhesive strength of ice on the stainless steel substrates. Methoxymethylethoxypropanol measured the highest average adhesive strength of ice to stainless steel. The average adhesive strength of ice on polymethylhydrosiloxane treated stainless steel was observed to have increased by 0.013 MPa compared to the average adhesive strength of ice on bare stainless steel. Bare stainless steel measured an average adhesive strength of 0.441±0.035 MPa. Methoxymethylethoxypropanol, polymethylhydrosiloxane, and octylphenol ethoxylate treated stainless steel measured an average adhesive strength of 1.078±0.058, 0.454±0.158, and 0.234±0.091 MPa, respectively.

Table 13

Summary of the average adhesive strength of ice on all variations of stainless steel substrates.

Stainless Steel	Average Shear Stress (MPa)	Standard Deviation	Random Standard Uncertainty	Random Uncertainty (95% Confidence)
Bare	0.441	0.041	0.014	0.035
Methoxymethyl…	1.078	0.067	0.024	0.058
Polymethyl…	0.454	0.184	0.065	0.158
Octylphenol…	0.234	0.107	0.038	0.091

Table 14 presents the ARF and percent difference of the average adhesive strength of ice on all variations of the stainless substrates observed in the present study. The ARF values indicate an increase in the adhesive strength of ice to stainless steel substrates treated with methoxymethylethoxypropanol and polymethylhydrosiloxane, and a decrease in the adhesive strength of ice on stainless steel substrates treated with octylphenol ethoxylate.

Methoxymethylethoxypropanol increased the average adhesive strength of ice to stainless steel the most of all of the surfactants observed in the present study. The average adhesive strength of ice on methoxymethylethoxypropanol treated stainless steel was more than double the average adhesive strength of ice measured on bare aluminum. The methoxymethylethoxypropanol and polymethylhydrosiloxane surface treatment increased the adhesive strength of ice on stainless steel by 144.60% and 2.97% respectively, while the octylphenol ethoxylate reduced the adhesive strength of ice by 46.97%.

Table 14

ARF and percent difference of all variations of stainless steel substrates.

Stainless Steel			
Surface Treatment	Average Shear Strength (MPa)	ARF	Percent Difference
Bare	0.441	1	N/A
Methoxymethylethoxypropanol	1.078	0.41	144.60
Polymethylhydrosiloxane	0.454	0.97	2.97
Octylphenol Ethoxylate	0.234	1.89	-46.97

Figure 40 presents the average adhesive strength of ice on all variations of the copper substrates observed in the present study at -10°C. The raw data for the averages presented in Figure 40 is shown in Table A-8. Figure 40 reveals that methoxymethylethoxypropanol treated copper demonstrated the highest average adhesive strength compared to all variations of copper observed in the present study Similar to the results observed on the aluminum and stainless steel substrates, polymethylhydrosiloxane and methoxymethylethoxypropanol was measured to have

increased the average adhesive strength of ice on copper. Octylphenol ethoxylate was the only surfactant observed in the present study that reduced the adhesive strength of ice on copper.

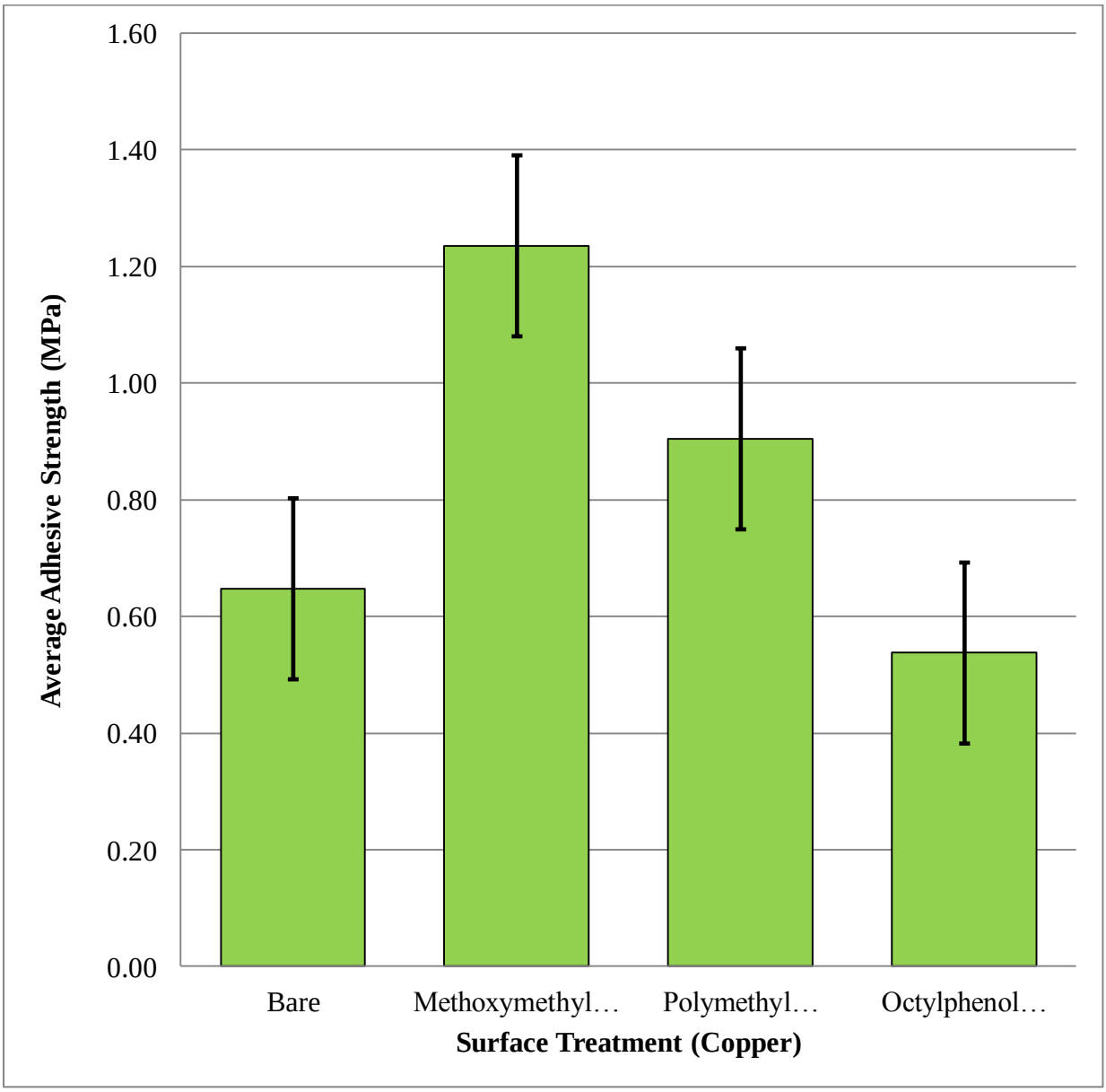

Figure 40. Adhesive strength of ice on the variations of copper substrates.

Table 15 presents the average adhesive strength of ice on all variations of copper. The raw data for the values expressed in Table 15 are presented in Table A-8. Octylphenol ethoxylate was the only surfactant used in the present study that reduced the adhesive strength of

ice on copper. Methoxymethylethoxypropanol measured the highest average adhesive strength of ice to copper. Methoxymethylethoxypropanol and polymethylhydrosiloxane surface treatments both increased the adhesive strength of ice on the copper substrates. Bare copper measured an average adhesive strength of 0.648±0.156 MPa. Methoxymethylethoxypropanol, polymethylhydrosiloxane, and octylphenol ethoxylate treated copper measured an average adhesive strength of 1.236±0.060, 0.905±0.189, and 0.538±0.064 MPa, respectively.

Table 15

Summary of the average adhesive strength of ice on all variations of copper substrates.

Copper	Average Shear Stress (MPa)	Standard Deviation	Random Standard Uncertainty	Random Uncertainty (95% Confidence)
Bare	0.648	0.182	0.064	0.156
Methoxymethyl…	1.236	0.070	0.025	0.060
Polymethyl…	0.905	0.221	0.078	0.189
Octylphenol…	0.538	0.074	0.026	0.064

Table 16 presents the ARF and percent difference of the average adhesive strength of ice on all variations of the copper observed in the present study. The ARF values indicate an increase in the adhesive strength of ice to copper substrates treated with methoxymethylethoxypropanol and polymethylhydrosiloxane. The ARF also indicates a decrease in the adhesive strength of ice on copper substrates treated with octylphenol ethoxylate. Methoxymethylethoxypropanol increased the average adhesive strength of ice to copper the most of all variations of copper observed in the present study. The methoxymethylethoxypropanol and polymethylhydrosiloxane surface treatments increased the adhesive strength of ice on copper

by 90.77% and 39.69% respectively. Octylphenol ethoxylate reduced the adhesive strength of ice by 17%.

Table 16

ARF and percent difference of all variations of copper substrates.

Copper			
Surface Treatment	Average Shear Strength	ARF	Percent Difference
Bare	0.648	1	N/A
Methoxymethylethoxypropanol	1.236	0.52	90.77
Polymethylhydrosiloxane	0.905	0.72	39.69
Octylphenol Ethoxylate	0.538	1.20	-17.00

Figure 41 presents the average adhesive strength of ice on all variations of the polycarbonate substrates observed in the present study at -10°C. The raw data for the averages presented in Figure 41 is shown in Table A-9. Figure 41 reveals that methoxymethylethoxypropanol the only surfactant measured to increase the average adhesive strength compared to all variations of polycarbonate observed in the present study. Polymethylhydrosiloxane had adverse affects on the polycarbonate compared to the metal substrates observed in the present study. Polymethylhydrosiloxane was measured to have increased the average adhesive strength of all metallic substrates observed in the present study. However, polymethylhydrosiloxane was measured to have reduced the adhesive strength of ice on polycarbonate. Polymethylhydrosiloxane and octylphenol ethoxylate demonstrated ice adhesion reduction capabilities on polycarbonate. Polymethylhydrosiloxane reduced the adhesive strength of ice on polycarbonate more effectively than octylphenol ethoxylate.

Polymethylhydrosiloxane would not be ideal in the application of reducing the adhesive strength of ice on aircraft structures since it only demonstrated ice adhesion reduction capabilities on polycarbonate substrates.

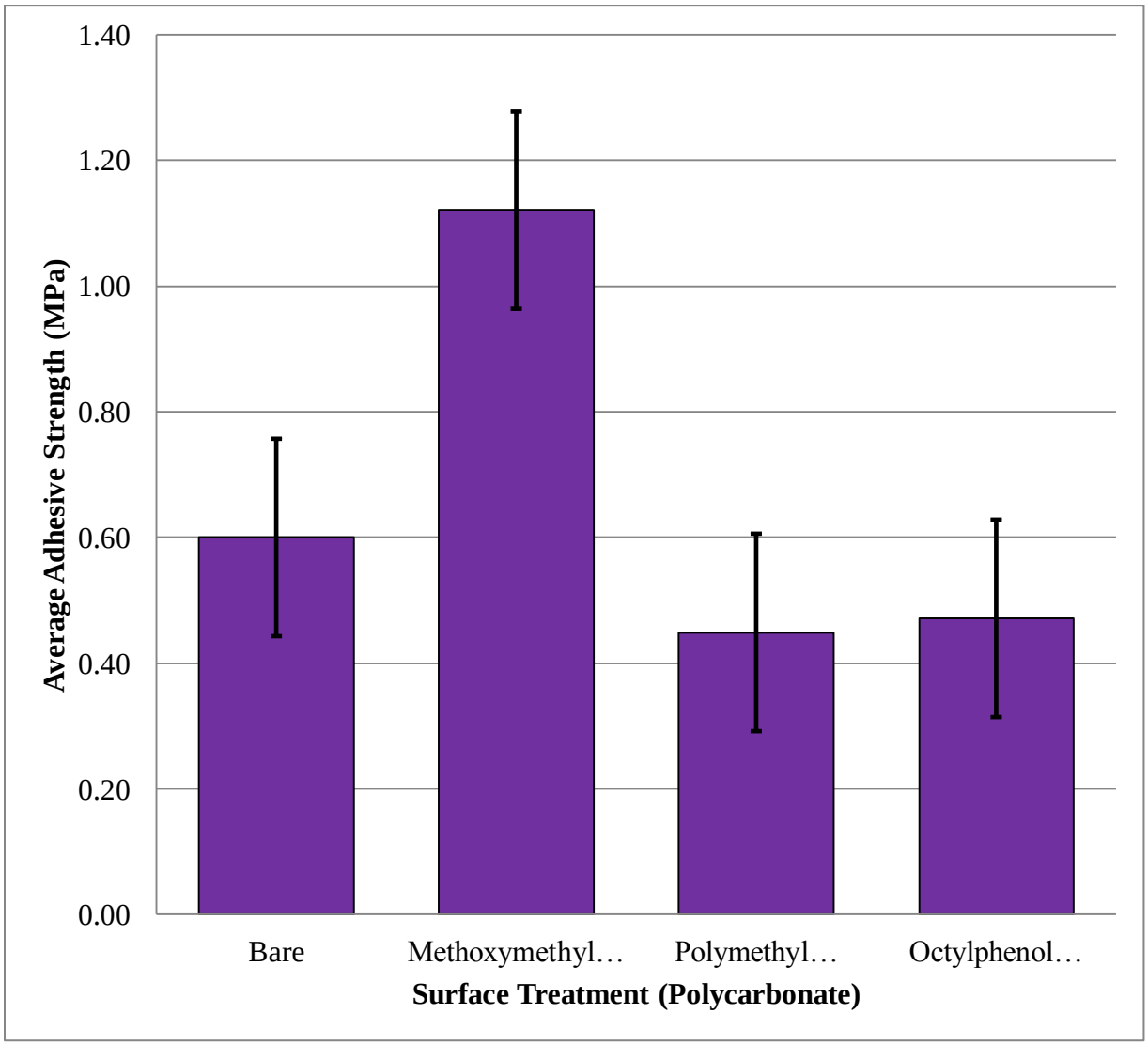

Figure 41. Adhesive strength of ice on the variations of polycarbonate substrates.

Table 17 presents the average adhesive strength of ice on all variations of polycarbonate. The raw data for the values expressed in Table 17 are presented in Table A-9. The octylphenol ethoxylate and the polymethylhydrosiloxane surfactants reduced the adhesive strength of ice on polycarbonate. The methoxymethylethoxypropanol surface treatment increased the adhesive

strength of ice on the polycarbonate substrates. Notably, the polymethylhydrosiloxane was observed to reduce the adhesive strength of ice on polycarbonate more effectively than the octylphenol ethoxylate. The average adhesive strength of ice on bare polycarbonate was measured to be 0.600±0.080 MPa. The average adhesive strength of ice on methoxymethylethoxypropanol, polymethylhydrosiloxane, and octylphenol ethoxylate treated polycarbonate were measured to be 1.121±0.135, 0.449±0.077, and 0.471±0.178 MPa respectively.

Table 17

Summary of the average adhesive strength of ice on all variations of polycarbonate substrates.

Polycarbonate	Average Shear Stress (MPa)	Standard Deviation	Random Standard Uncertainty	Random Uncertainty (95% Confidence)
Bare	0.600	0.094	0.033	0.080
Methoxymethyl…	1.121	0.158	0.056	0.135
Polymethyl…	0.449	0.090	0.032	0.077
Octylphenol…	0.471	0.208	0.074	0.178

Table 18 presents the ARF and percent difference of the average adhesive strength of ice on all variations of the polycarbonate observed in the present study. The ARF values indicate an increase in the adhesive strength of ice to polycarbonate substrates treated with methoxymethylethoxypropanol, and a decrease in the adhesive strength of ice on poycarbonate substrates treated with octylphenol ethoxylate and polymethylhydrosiloxane. The methoxymethylethoxypropanol surface treatment increased the adhesive strength of ice on copper by 86.80%. Polymethylhydrosiloxane and octylphenol ethoxylate reduced the adhesive

strength of ice by 25.19% and 21.45%, respectively. Though polymethylhydrosiloxane reduced the adhesive stregnth of ice more effectively on polycarbonate than the octylphenol ethoxylate surfactant, polymethylhydrosiloxane would not be considered ideal for reducing the adhesive strength of ice on aircraft structures.

Table 18

ARF and percent difference of all variations of polycarbonate substrates.

Polycarbonate			
Surface Treatment	Average Shear Strength	ARF	Percent Difference
Bare	0.600	1	N/A
Methoxymethylethoxypropanol	1.121	0.54	86.80
Polymethylhydrosiloxane	0.449	1.34	-25.19
Octylphenol Ethoxylate	0.471	1.27	-21.45

Figure 42 presents a bar graph summarizing of all of the average adhesive strength data collected in the present study. Polymethylhydrosiloxane and methoxymethylethoxypropanol was measured to have increased the average adhesive strength of ice on aluminum, stainless steel, and copper. Methoxymethylethoxypropanol, a chemical advertised as water repellant, was measured to increase the adhesive strength of ice of all of the substrates observed in the present study. Methoxymethylethoxypropanol consistently increased the adhesive strength of ice on all of the substrates observed in the present study. Substrates treated with the methoxymethylethoxypropanol measured the highest average adhesive strength values compared to all of the variations observed in the present study. Octylphenol ethoxylate was measured to reduce the adhesive strength of ice on all substrates; however, the polymethylhydrosiloxane

reduced the adhesive strength of ice on polycarbonate more effectively. Octylphenol ethoxylate demonstrates ice adhesive reduction properties that are desired.

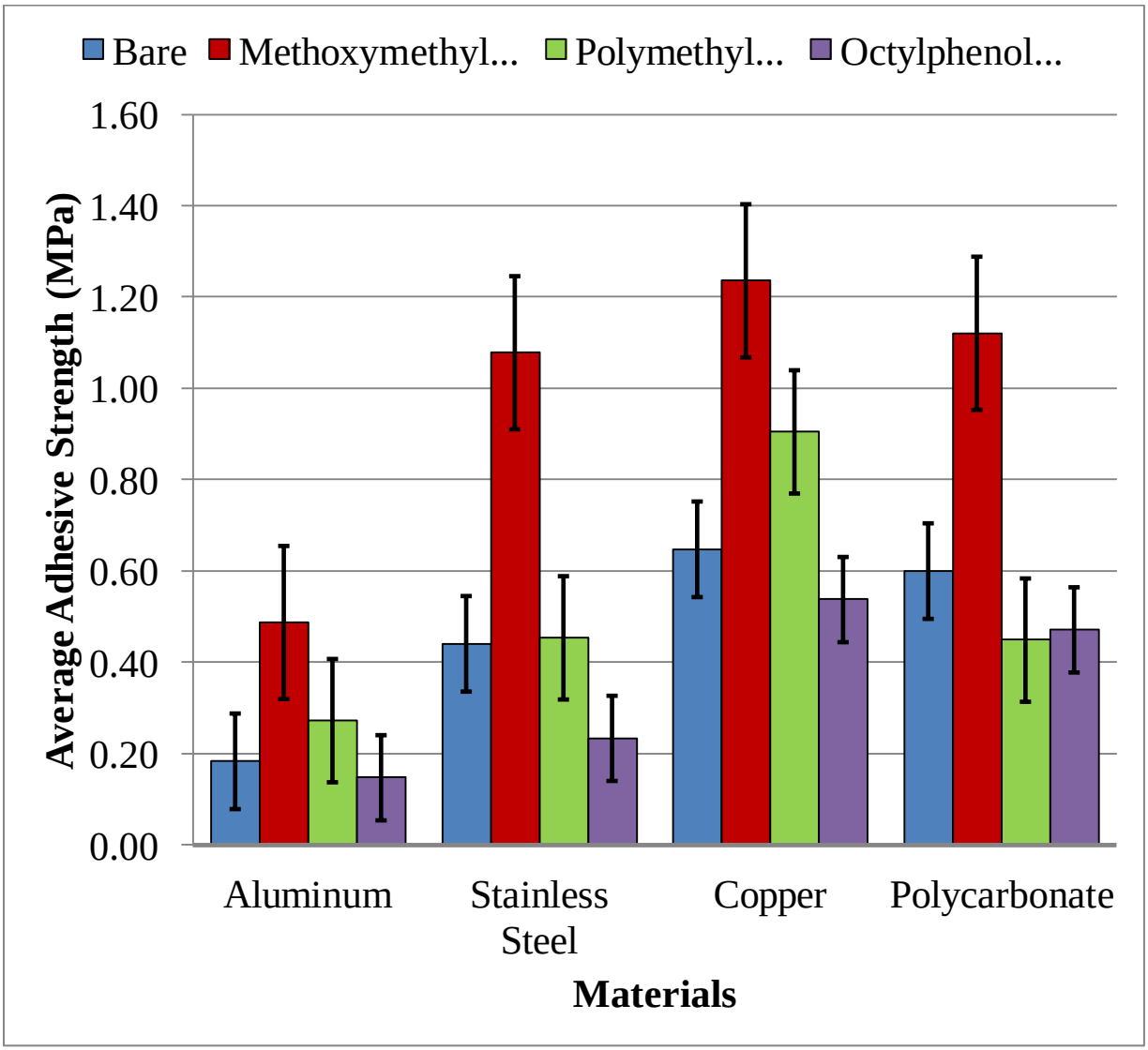

Figure 42. Summary of all of the average adhesive strength data collected in the present study.

4.2. Measurement of Wettability on Surfactant Treated Substrates

Figure 43 shows images of a sessile droplet on bare aluminum, stainless steel, copper, and polycarbonate. The sessile droplet on a bare aluminum substrate displayed in Figure 43(a) appears to exhibits non-wetting surface properties. The sessile droplets on the surface of the

stainless steel, copper, and polycarbonate substrates displayed in Figures 43(b), 43(c), and 43(d) respectively, exhibit surface properties that correspond with wetting.

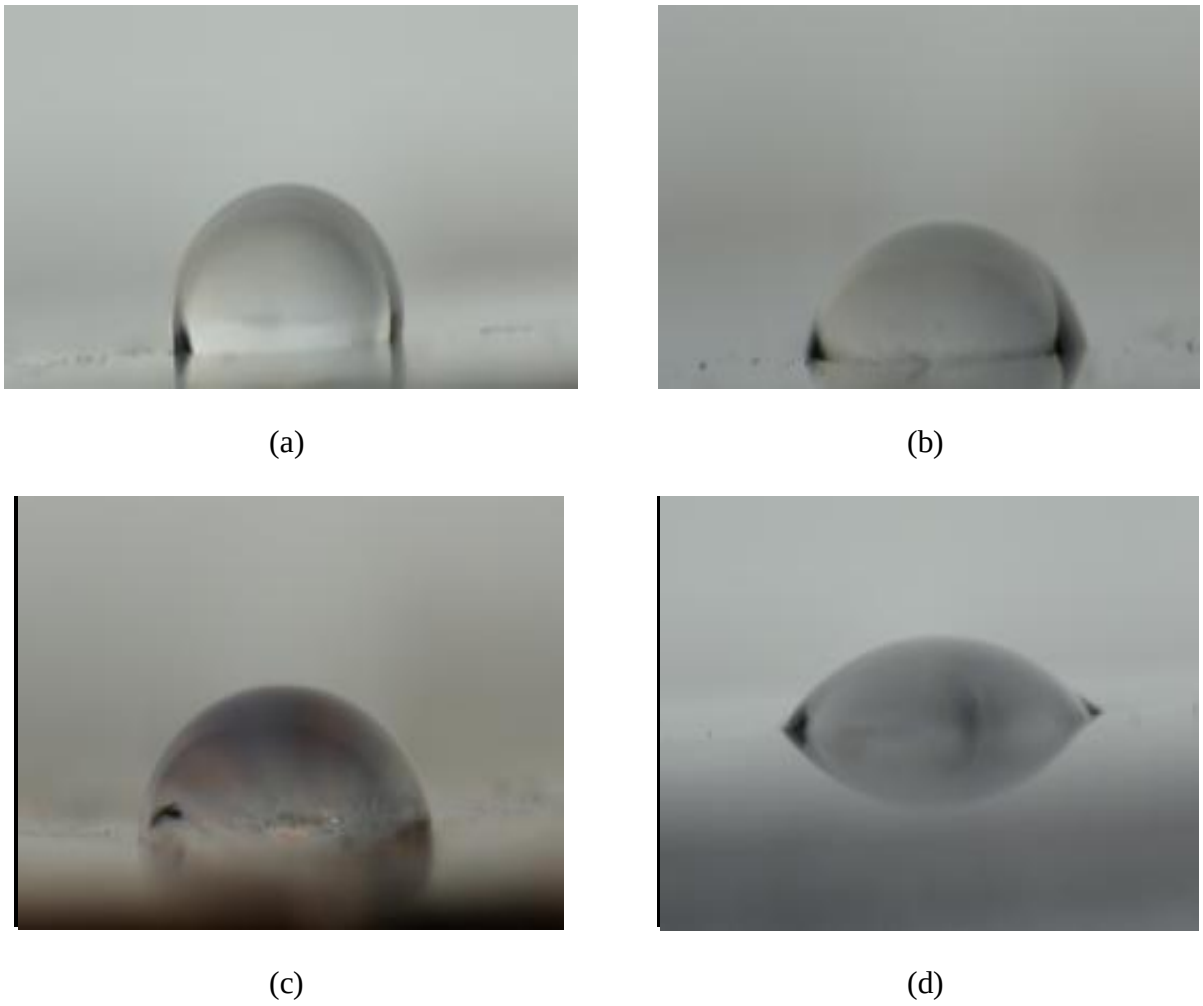

Figure 43. Sessile droplet on bare (a) aluminum, (b) stainless steel, (c) copper, and (d) polycarbonate substrates.

Table 19 presents the respective average contact angles measured on the sessile droplet. Table 19 reveals that bare aluminum possesses slightly hydrophobic surface properties, causing the droplet shown in Figure 43(a) to display a contact angle slightly greater than 90°. The copper, polycarbonate, and stainless steel substrates all possessed wetting surface properties, demonstrating contact angles less than 90°. The bare polycarbonate substrate displayed the

smallest average contact angles suggesting that bare polycarbonate highest wettability of all the bare substrates observed in the present study. The bare aluminum substrate measured the highest average contact angle suggesting that bare aluminum had the lowest wettability of the bare substrates observed in the present study. The average contact angles measured on bare aluminum, stainless steel, copper, and polycarbonate were 90.0°±4.9°, 76.7°±1.9°, 80.3°±5.5°, and 66.5°±1.3° respectively. Recalling the results from Chapter 4.1, the average adhesive strength of ice on bare aluminum, stainless steel, copper, and polycarbonate was measured to be 0.184±0.031, 0.441±0.035, 0.684±0.156, and 0.600±0.080 MPa, respectively. The results demonstrate that the adhesive strength of ice on a material with low wettability (i.e. aluminum) is weaker compared to materials with higher wettability (i.e. stainless steel, copper, and polycarbonate).

Table 19

Contact angles measurements of sessile droplets on bare substrates.

Bare					
Material	Contact Angle			Average	Standard Deviation
Aluminum	95.6	86.5	88.1	90.0	4.9
Stainless Steel	75.8	75.3	78.9	76.7	1.9
Copper	86.6	77.4	76.9	80.3	5.5
Polycarbonate	67.1	65.0	67.6	66.5	1.3

Methoxymethylethoxypropanol is a chemical that is advertised in industry as water repellant. Figure 44 shows images of a sessile droplet on methoxymethylethoxypropanol treated aluminum, stainless steel, copper, and polycarbonate. All of the sessile droplets shown in Figure

44 are wetting the surfaces of each of the respective substrates. The results suggest that methoxymethylethoxypropanol does not necessarily repel water on all of the substrates observed in the present study.

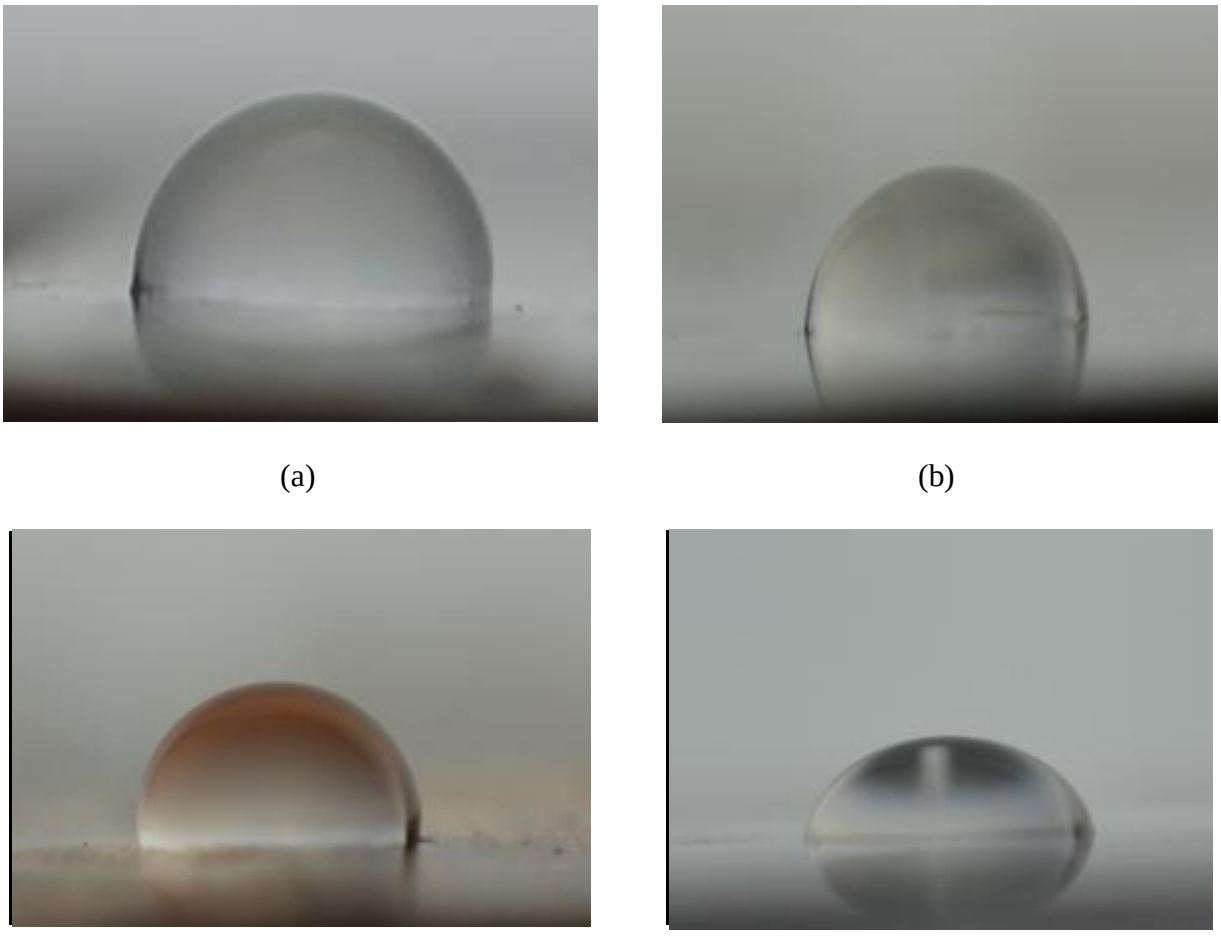

(a) (b)

(c) (d)

Figure 44. Sessile droplet on methoxymethylethoxypropanol treated (a) aluminum, (b) stainless steel, (c) copper, and (d) polycarbonate substrates.

Table 20 presents the respective average contact angles measured on sessile droplets and the percent difference compared to the average contact angles measured on the corresponding bare substrates. Table 20 reveals that the methoxymethylethoxypropanol reduced the surface energy of the aluminum, stainless steel, and copper, which is suggested by the decrease in

average contact angle measured on the sessile droplets. The methoxymethylethoxypropanol increased the wettability of the stainless steel, copper, and aluminum substrates. The contact angles measured on polycarbonate was determined to have increased. The results suggest that methoxymethylethoxypropanol increased the surface energy of polycarbonate, thus wettability was measured to decrease. Methoxymethylethoxypropanol did not demonstrate water repelling properties on all of the materials observed in the present study. Recalling the results from Chapter 4.1, methoxymethylethoxypropanol treated substrates were measured to increase the adhesive strength of ice on all substrates observed in the present study. The results suggest that water repellant does not necessarily imply ice repellency.

Table 20

Contact angles measurements of sessile droplets on methoxymethylethoxypropanol treated substrates.

Methoxymethylethoxypropanol						
Material	Contact Angle			Average	Standard Deviation	Percent Difference
Aluminum	81.9	72.7	76.8	77.1	4.6	-14.4
Stainless Steel	57.0	65.2	65.5	62.6	4.8	-18.4
Copper	80.1	77.7	72.7	76.8	3.8	-4.3
Polycarbonate	73.8	75.6	72.8	74.1	1.4	11.3

Figure 45 shows images of a sessile droplet on polymethylhydrosiloxane treated aluminum, stainless steel, copper, and polycarbonate. Recalling the results from chapter 4.1, polymethylhydrosiloxane increased the average adhesive strength of ice on all metallic substrates, however, reduced the average adhesive strength of ice on polycarbonate.

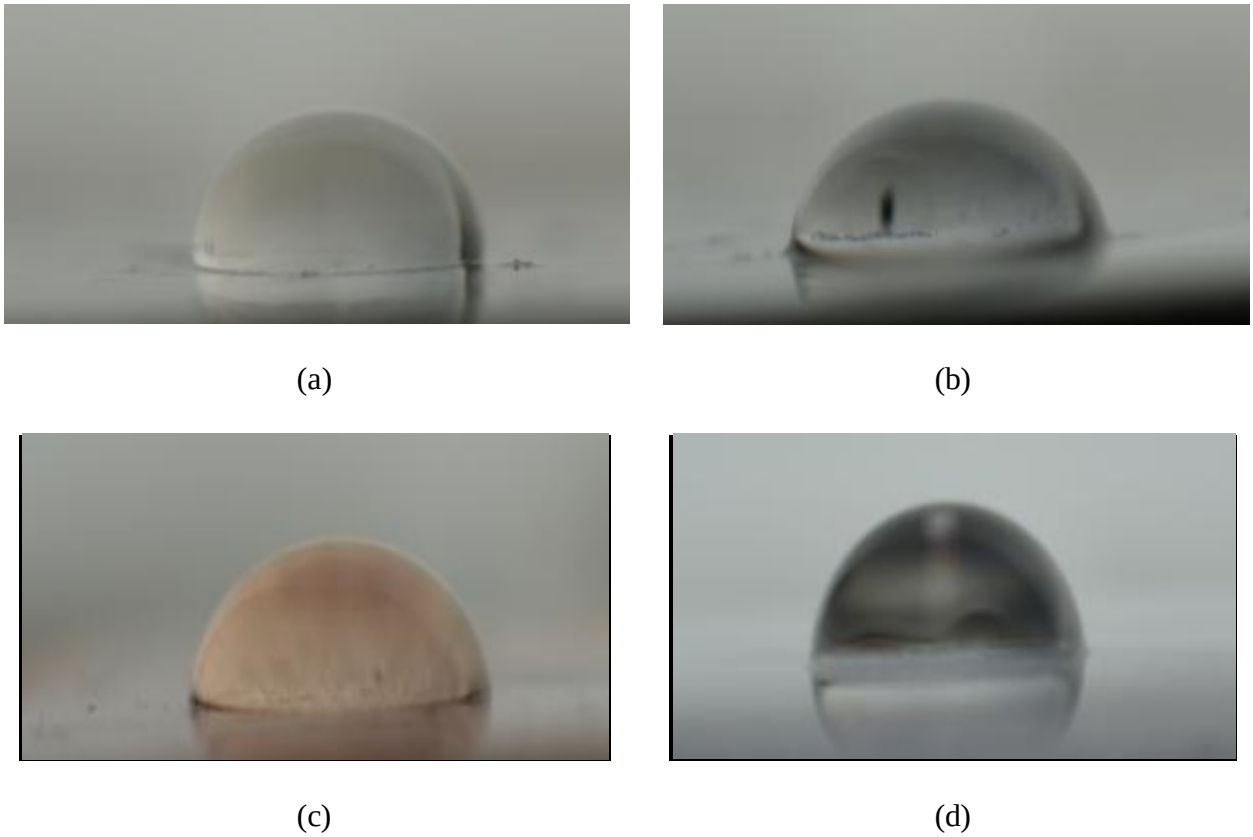

(a) (b)

(c) (d)

Figure 45. Sessile droplet on polymethylhydrosiloxane treated (a) aluminum, (b) stainless steel, (c) copper, and (d) polycarbonate substrates.

Table 21 presents the respective contact angles measured on sessile droplets and the percent difference compared to the average contact angles measured on the corresponding bare substrates. Table 21 reveals that the polymethylhydrosiloxane surface treatment reduced the surface energy of the copper, causing copper to become more wetting. Polymethylhydrosiloxane was also measured to have increased the surface energy of aluminum, stainless steel, and polycarbonate, causing the contact angle of each material to increase. The polymethylhydrosiloxane surface treatment was measured to have increased the average contact angle of aluminum, stainless steel, and polycarbonate by 6.1%, 4.3%, and 44.1%, respectively. The polymethylhydrosiloxane surface treatment was measured to have decreased the average

contact angle of copper by 12.2%. Polymethylhydrosiloxane treated aluminum and polycarbonate displayed hydrophobic surface properties, displaying average contact angles of 95.5°±2.9° and 95.9°±3.4°, respectively. Recalling the results from Chapter 4.1, polymethylhydrosiloxane was measured to have reduced the average adhesive strength of ice on polycarbonate by 25.19% The results suggest that hydrophobic surfaces are capable of reducing the adhesive strength of ice. Though polymethylhydrosiloxane reduced the adhesive stregnth of ice on polycarbonate, polymethylhydrosiloxane would not be considered ideal for reducing the adhesive strength of ice on aircraft structures since ice adhesion reduction was only measured on polycarbonate.

Table 21

Contact angles measurements of sessile droplets on polymethylhydrosiloxane treated substrates.

Polymethylhydrosiloxane						
Material	Contact Angle			Average	Standard Deviation	Percent Difference
Aluminum	97.1	97.2	92.1	95.5	2.9	6.1
Stainless Steel	83.1	76.8	80.0	80.0	3.2	4.3
Copper	71.2	68.7	71.8	70.5	1.6	-12.2
Polycarbonate	98.2	92.0	97.5	95.9	3.4	44.1

Figure 46 shows images of a sessile droplet on octylphenol ethoxylate treated aluminum, stainless steel, copper, and polycarbonate. All of the sessile droplets shown in Figure 46 are highly wetting. The results suggest that the octylphenol ethoxylate surfactant greatly reduces the surface energy of all of the substrates observed in the present study. Octylphenol ethoxylate demonstrates ice adhesive reduction properties that are desired in reducing icing on aircraft

structures since it is capable of reducing the adhesive strength of ice on various materials similar to those used on aircraft structures.

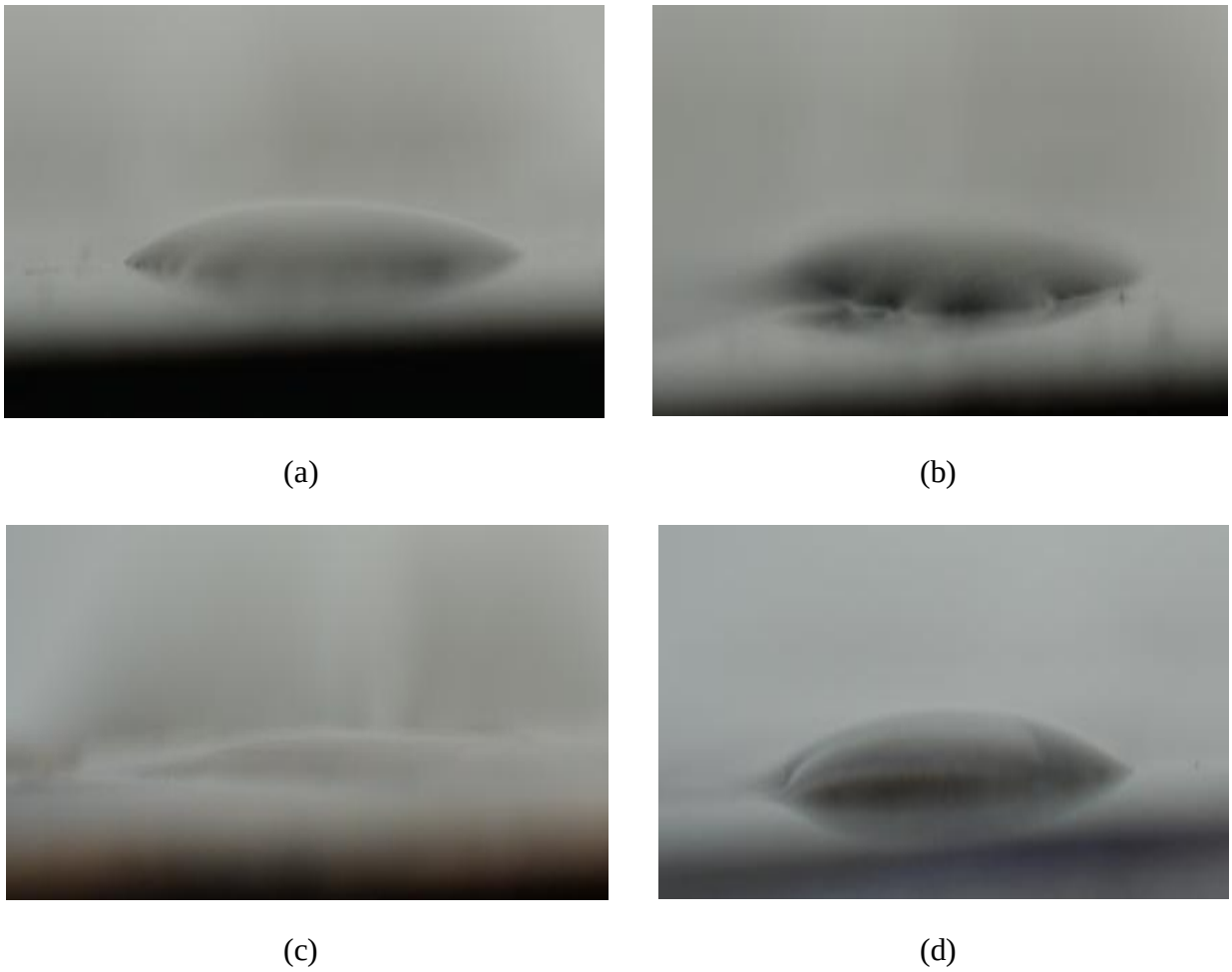

(a) (b)

(c) (d)

Figure 46. Sessile droplet on octylphenol ethoxylate treated (a) aluminum, (b) stainless steel, (c) copper, and (d) polycarbonate substrates.

Table 22 presents the respective contact angles measured on sessile droplets and the percent difference compared to the average contact angles measured on the corresponding bare substrates. Table 22 reveals the octylphenol ethoxylate surface treatment reduced the surface energy of each substrate greatly, causing all substrates observed in the present study to demonstrate superhydrophilic surface properties. Recalling the results from Chapter 4.1, the octylphenol ethoxylate surface treatment reduced the adhesive strength of ice on all of the

substrates, demonstrating that surfaces do not necessarily have to be hydrophobic to reduce the adhesive strength of ice.

Table 22

Contact angles measurements of sessile droplets on octylphenol ethoxylate treated substrates.

Octylphenol Ethoxylate						
Material	Contact Angle			Average	Standard Deviation	Percent Difference
Aluminum	21.7	20.0	22.1	21.3	1.1	-76.4
Stainless Steel	16.7	23.9	20.9	20.5	3.6	-73.3
Copper	5.0	10.6	14.2	9.9	4.7	-87.6
Polycarbonate	29.3	31.6	27.7	29.5	2.0	-55.7

4.3. Observation of Freezing Sessile Droplets in a Subcooled Environment

Figure 47 presents a schematic depicting how the freezing process of the sessile droplets occurred. A droplet was dispensed from a syringe composed completely of liquid, depicted in Figure 47 as the teal colored droplet. As time progressed and nucleation began, a layer of ice formed around the outside of the droplet, encasing the liquid content of the droplet within a shell of ice, depicted as the blue colored droplet in Figure 47. During this particular point in the nucleation process, the droplet was observed to increase in area, physically expanding and deforming from its original profile. The nucleation process progressed from the outside of the sessile droplet towards the center until the entire droplet became solid. The results observed suggest, that a sessile droplet exposed to ambient temperatures below freezing, will undergo a nucleation process where the sessile droplet will freeze from the outside of the droplet inward.

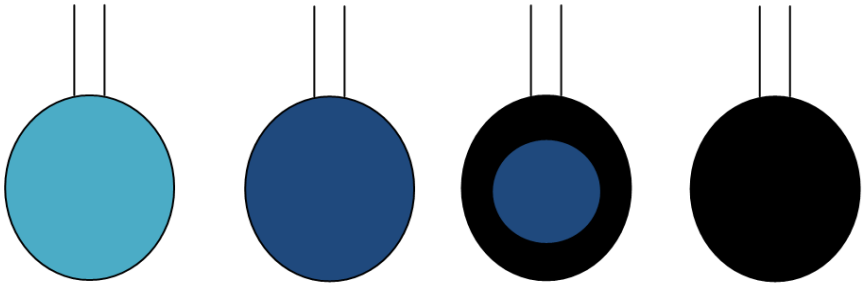

Figure 47. Schematic of the freezing process of a sessile droplet.

Figure 48 presents images recorded of an actual sessile droplet freezing using high speed imaging. As previously described, the droplets were observed freezing from the outside inward. The time elapsed for the event shown in Figure 48, which occurred from approximately 28% solid ice and 72% liquid water to 100% solid ice, was 6.52 seconds. The volumetric freeze rate of the sessile droplet was measured to be 4.62 mm^3/second and the duration of the entire freezing process of a sessile droplet at -40°C was found to be 10.67 seconds. Figure 48(a) reveals that ice nucleates in a sessile droplet in the form of a crescent shape which appears thickest at the region of contact between the sessile droplet and the needle tip of the syringe. The results suggest that the tip of the syringe needle possessed sites that allowed for a heterogeneous nucleation process to initiate.

(a) 0 seconds (b) 3.81 seconds (c) 6.52 seconds

Figure 48. Images of a sessile droplet freezing at subcooled temperatures recorded using high speed imaging.

In an earlier study conducted by Jin and Hu (2010), freezing within a sessile droplet on a cold plate cooled to -2°C was reported to occur in 35 seconds, while in the present study, freezing of a sessile droplet at -40°C was observed to occur in 10.67 seconds, demonstrating that the nucleation rate is dependent on temperature. The results comply with the theory mentioned in Chapter 2.2.1. At lower temperatures nucleation more readily occurs, requiring a smaller critical radius and less activation energy compared to a nucleation process at higher temperatures.

Figure 49 are images of the polystyrene test section used to capture images of the freezing sessile droplet. Condensation was observed forming to the aluminum test stand and the polycarbonate window within the polystyrene test section. The condensation that accumulated on the aluminum and polycarbonate surfaces would eventually transform into ice. However, icing did not develop on the polystyrene itself. Aluminum and polycarbonate physically possess thermally conductive material properties, while polystyrene is an adequate insulator capable of conducting little to no thermal energy. The results suggest condensation and ice cannot form on materials that lack thermal conductivity. Thus, there must be thermal conductivity present for nucleation to occur and ice to form on the surface of a material. Testing the idea that ice cannot form on materials that lack thermal conductivity, a liquid sessile droplet was placed on a polystyrene substrate and introduced to subcooled temperatures. The droplet was observed to maintain its capabilities of nucleating and forming into ice at subcooled temperatures. However, the frozen sessile droplet did not adhere to the polystyrene substrate. The results disagree with the suggestion that ice cannot form on materials that lack thermal conductivity. Condensation remained inexistent on the surface of the polystyrene substrate, suggesting that condensation may not be capable of forming onto thermally insulated material.

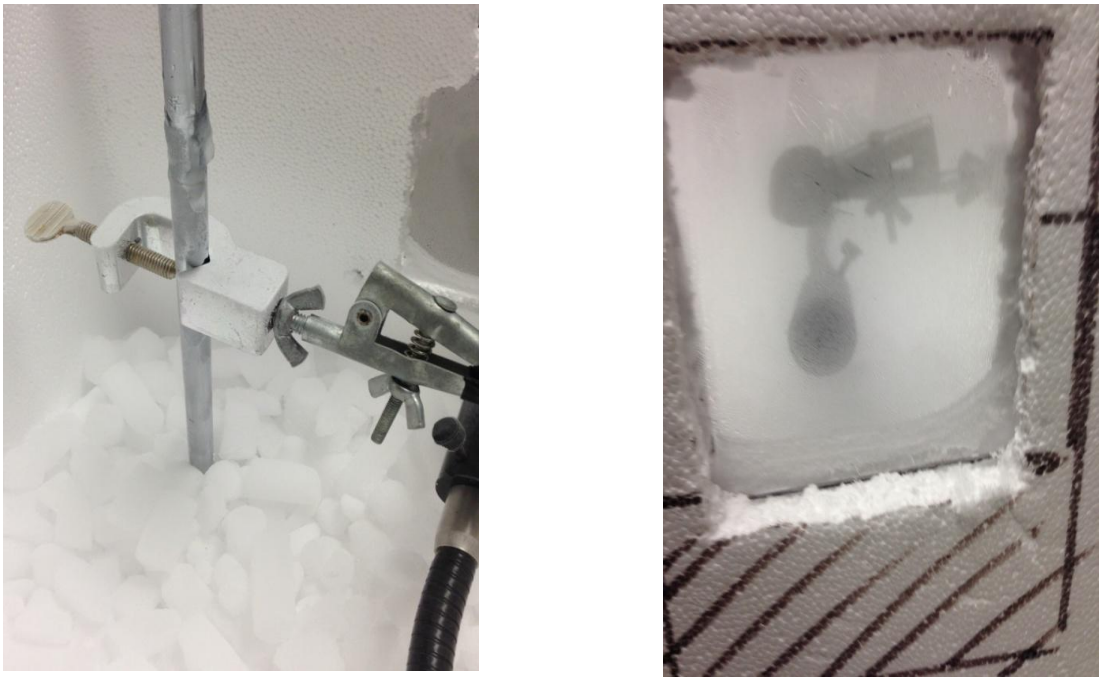

(a) (b)

Figure 49. Freezing observed in polystyrene test section on (a) aluminum test stand and (b) polycarbonate window.

Figure 50 are images that were taken by the high speed camera while visualizing freezing of droplets in supercooled silicone oil. The specific gravity of silicone oil is 0.872, thus silicone oil is denser than water. The specific gravity of ice is 0.917, thus ice is denser than silicone oil. Droplets were observed sinking to the bottom of the test tube due the difference in density between the two liquids. As the droplets sank to the bottom of the test tube, gas bubbles were visualized being released from the sinking droplet. The production of the gas bubbles became more frequent prior to the solidifying droplets rising to the surface of the silicone oil. As the solidifying droplets rose to the surface of the silicone oil, gas bubbles surrounded the droplets. The gas bubbles acted as a method of floatation contributing to the acceleration of the droplet to surface of the silicone oil before detaching from the droplet. The droplets dispensed into the supercooled silicone oil maintained a spherical shape throughout the duration of the nucleation

process. The results suggest that air was entrapped with the droplet during the nucleation process. The entrapped air occupied within the ice droplets reduced the density of the ice observed in the present study, thus ice was visualized floating in the silicone oil. The results suggest that homogenous nucleation occurred during the phase transformation.

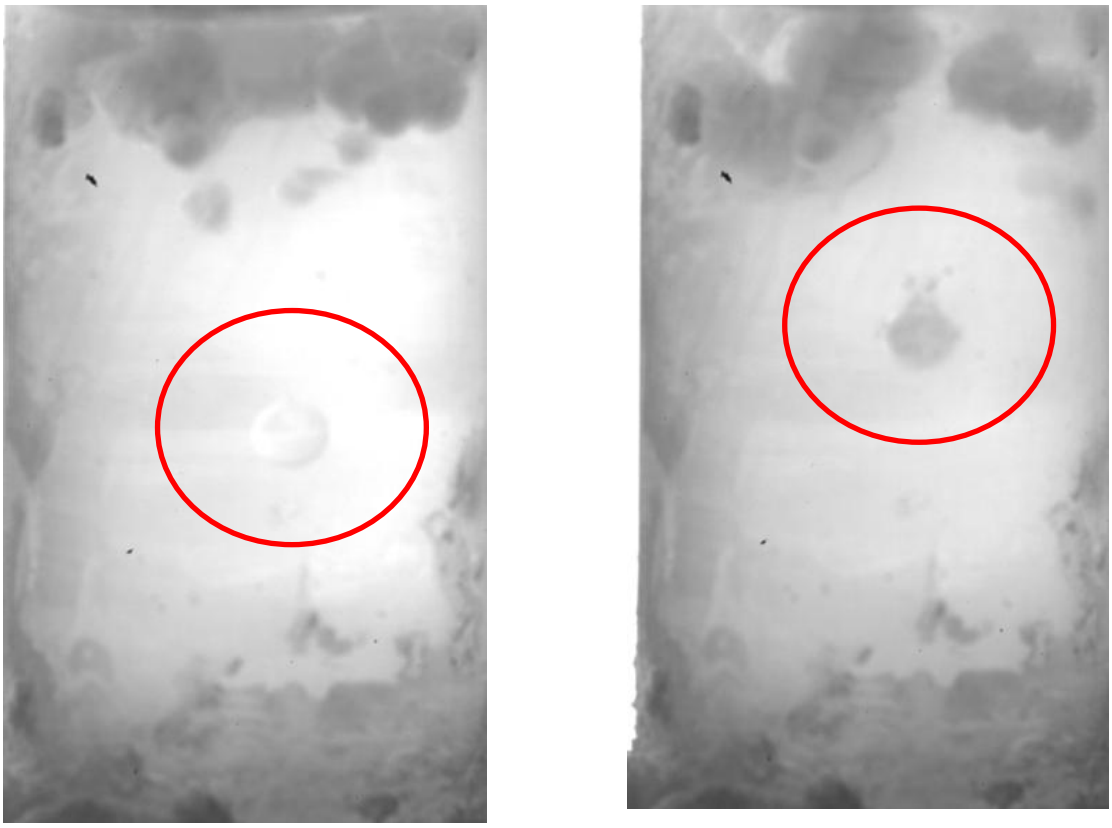

(a) (b)

Figure 50. Visualization of droplet in supercooled silicone oil (a) before and (b) after freezing.

Figure 51 are images of sessile droplets frozen in supercooled silicone oil. Droplets were allowed to sink to the bottom of the test tube at room temperature prior to supercooling the silicone oil. In contrast to the droplets shown in Figure 50, the droplets in Figure 51 deformed from the original spherical shape into a spherical cap. Droplets were observed freezing from the bottom to the peak of the spherical cap. The peak of the freezing spherical cap appeared deformed in its final form due to volume expansion during the nucleation process. Gas bubbles

were observed being released from the sessile droplet as freezing occurred, similar to the droplets described in Figure 50. The droplets did not rise to the surface of the silicone oil however, suggesting that a bond was formed between the droplet and the surface of the test tube. The results suggest that heterogeneous nucleation occurred during this particular phase transformation.

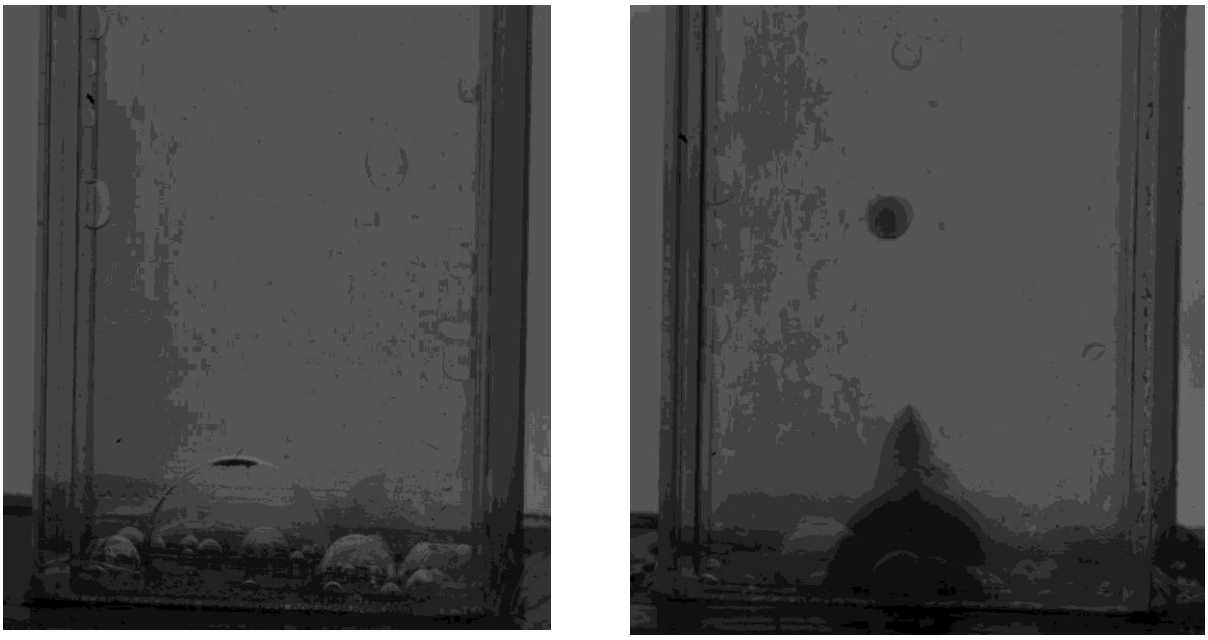

(a) (b)

Figure 51. Sessile droplets (a) before and (b) after freezing in supercooled silicone oil.

4.3. Heat Transfer Lumped System Analysis of a Supercooled Droplet

Figure 52 shows the results from the lumped system analysis performed on a spherical droplet under similar conditions as the sessile droplet in Chapter 4.3. Figure 52 suggests that the temperature within a sessile droplet when introduced to an ambient temperature of -40°C will be cooled to -40°C in 1.5 seconds. Recall the observations made in Chapter 4.3, the sessile droplet under investigation did not completely nucleate into ice until an elapsed time of 10.67 seconds.

The results suggest that heat transfer lumped system analysis is not capable of predicting the onset of freezing or volumetric freeze rate of a droplet exposed to subcooled conditions.

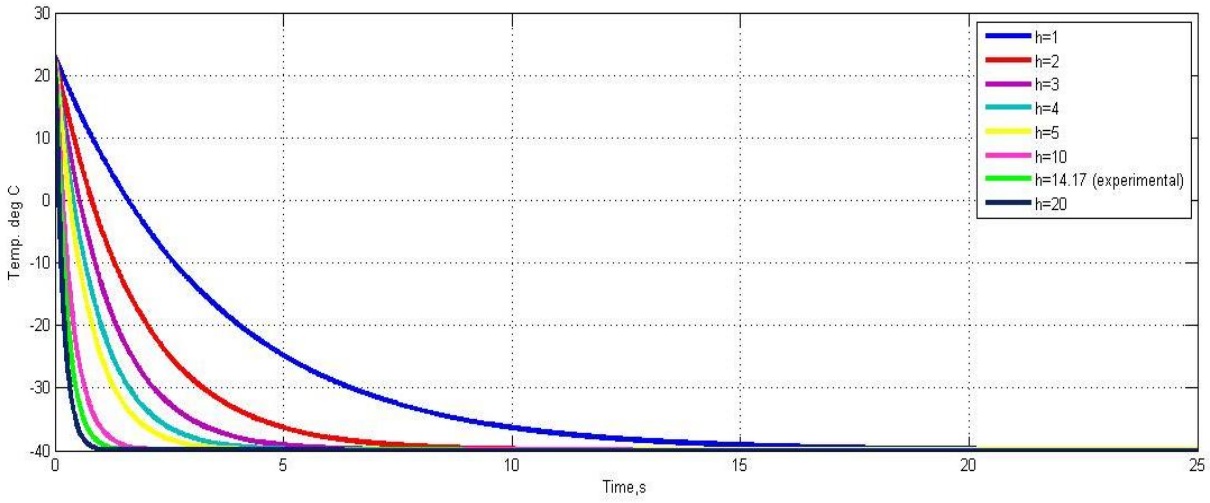

Figure 52. Lumped system analysis performed on a spherical droplet in a subcooled environment.

CHAPTER 5

Discussion and Future Research

All of the specific objectives of the present study have been met. The average adhesive strength of ice on aluminum at -5, -10, -20, and -30°C was measured to be 0.215±0.031, 0.184±0.031, 0.213±0.041, and 0.202±0.035 MPa respectively. The results suggest that the adhesive strength of ice is not dependent on temperature. Further tests were conducted on bare, methoxymethylethoxypropanol treated, polymethylhydrosiloxane treated, and octylphenol ethoxylate treated aluminum, stainless steel, copper, and polycarbonate substrates at -10°C. Though none of the surfactants used in the current study proved to be truly ice-phobic, the octylphenol ethoxylate, a surfactant that causes surfaces to exhibit superhydrophilic characteristics, reduced the adhesive strength of ice on all of the substrates. Polymethylhydrosiloxane reduced the adhesive strength of ice on polycarbonate. However, polymethylhydrosiloxane increased the adhesive strength of ice on all metals observed in the present study. Methoxymethylethoxypropanol increased the adhesive strength of ice on all substrates, suggesting water repellant surfactants do not necessarily repel icing.

Sessile droplets supercooled to -40°C were observed nucleating heterogeneously from the outside of the droplet inward, initiating from the tip of a syringe needle tip. The sessile droplet completely solidified in 10.67 seconds, at a volumetric freezing rate of 4.62 mm^3/second. In an earlier study conducted by Jin and Hu (2010), freezing within a sessile droplet on a cold plate cooled to -2°C was reported to occur in 35 seconds, while in the present study, freezing of a sessile droplet at -40°C was observed to occur in 9.46 seconds, suggesting that the nucleation rate is dependent on temperature.

While observing the freezing process in sessile droplets, ice was observed developing and adhering to an aluminum test stand and polycarbonate window within a polystyrene test section. Condensation and ice were not observed to form on the polystyrene test section. Aluminum and polycarbonate physically possess thermally conductive material properties, while polystyrene is an adequate insulator capable of conducting little to no thermal energy. The results suggest condensation cannot form on materials that lack thermal conductivity, thus there must be thermal conductivity present for condensation to form on the surface of a material.

According to the results from the heat transfer lumped system analysis, a liquid droplet exposed to a subcooled environment will take 1.50 seconds to cool to -40°C from room temperature. The time determined from the lumped system analysis was less than the results measured in Chapter 4.3, in which the nucleation process of a sessile droplet introduced to a subcooled environment completely developed in 10.67 seconds. The results suggest that heat transfer lumped system analysis is not capable of predicting the onset of freezing or volumetric freeze rate of a droplet exposed to subcooled conditions.

An area to be considered for future studies in icing on aircraft structures is the development of microstructures capable of producing hydrophobic and hydrophilic surface properties. The current study demonstrated that both hydrophobic and hydrophilic surface properties are capable are reducing the adhesive strength of ice by means of coatings. Coatings become an issue when introduced to rapid and consistent precipitation rates, and cratering in the film occurs, however, this problem can be solved if the use of coatings becomes obsolete.

Another area to be considered for future studies is the role that conductivity may play in the formation and adhesive strength of ice. As mentioned in Chapter 4.3, it was observed that at subcooled temperatures, condensation was attracted to aluminum and polycarbonate surfaces.

Condensation would accumulate to the aluminum and polycarbonate surfaces, and eventually transform into ice. However, condensation, nor ice, was observed forming on the surrounding polystyrene, suggesting that thermal conductivity may dictate the attraction of condensation and perhaps the initiation of a heterogeneous nucleation process.

Lastly, another area to be considered for future studies in aircraft icing is the combination of anti-icing and de-icing techniques. Combining anti-icing and de-icing techniques could essentially reduce the workload of a single operating anti-icing or de-icing technique. The use of multiple anti-icing and de-icing techniques in conjunction with each other may create a more efficient ice removal procedure with a longer operational lifespan. Throughout the area of aircraft icing there is continuous development of anti-icing and de-icing techniques. Numerous combinations are possible with the continuous development of anti-icing and de-icing techniques, some of which could proficiently reduce the adhesive strength of ice and have yet to be discovered.

References

Aksay, I. A., Hoge, C. E., & Pask, J. A. (1974). Wetting under Chemical Equilibrium Conditions. *Journal of Physical Chemistry, 12*(78), 1178-1183.

Allen, J. S. (2003). An Analytical Solution for Determination of Small Contact Angles from Sessile Srops of Arbitrary Size. *Journal of Colloid and Interface Science, 261*.

Anderson, D. N., & Reich, A. D. (1997). Tests of the Performance of Coatings for Low Adhesion. *AIAA Paper 97-0303*.

Anderson, J. D. (2007). *Fundamentals of Aerodynamics* (4th ed.). New York: McGraw-Hill.

Atchison, K., & Bohn, P. T. (1981). *NASA Lewis Working on De-Icing for Small Planes, Copters*. (NASA 81-38). Washington, DC: NASA.

Benson, T. (2009). Schlieren System. Retrieved from http://www.grc.nasa.gov/WWW/k-12/airplane/tunvschlrn.html

Bernardin, J. D., Mudawar, I., Walsh, C. B., & Franses, E. I. (1996). Contact Angle Temperature Dependence for Water Droplets on Practical Aluminum Surfaces. *International Journal of Heat and Mass Transfer, 40*(5), 1017-1033.

Boinovich, L., & Emelyanenko, A. (2011). Wetting and Surface Forces. *Advances in Colloid and Interface Science, 165*, 60-69.

Bonn, D., Eggers, J., Indekeu, J., Meunier, J., & Rolley, E. (2009). Wetting and Spreading. *Reviews of Modern Physics, 81*, 739-805.

Callister, W. D. (2005). *Material Science and Engineering: An Integrated Approach* (2nd ed.). Hoboken, NJ: Wiley.

Cengel, Y. A., & Boles, M. A. (2008). *Thermodynamics: An Engineering Approach* (6th ed.). New York: McGraw Hill.

Chung, C. K., Chang, W. T., Chen, C. F., & Liao, M. W. (2011). Effect of Temperature of the Evolution of Diffusivity, Microstructure, and Hardness of Nanocrystalline Nickel Films Electrodeposited at Low Temperatures. *Materials Letters, 65*(3), 416-419.

De Coninck, J., De Ruijter, M. J., & Voue, M. (2000). Dynamics of Wetting. *Current Opinion in Colloid & Interface Science, 6*, 49-53.

De Gennes, P. G. (1985). Wetting: Statics and Dynamics. *Review of Modern Physics, 57*(3), 827-863.

Due, J. L., Muller, M. R., & Swangler, M. (1996). Cratering Phenomena on Aircraft Anti-Icing Films. *Journal of Aircraft, 33*(1), 131-138.

FAA. (2013). Airplane Flying Handbook Retrieved from http://talkaviation.com/content/section/357-airplane-flying-handbook.html

Farhadi, S., Farzaneh, M., & Kulinich, S. A. (2011). Anti-Icing Performance of Superhydrophobic Surfaces. *Applied Surface Science, 257*(14), 6264-6269.

Farzaneh, M. (2000). Ice Accretions on High-Voltage Conductors and Insulators and Related Phenomena. *Philosophical Transactions: Mathematical, Physical and Engineering Sciences, 358*(1776).

Ferreira, T., & Rasband, W. (2013). *ImageJ User Guide*. National Institute of Health Retrieved from http://rsbweb.nih.gov/ij/docs/guide/user-guide.pdf.

Figliola, R. S., & Beasley, D. E. (2011). *Theory and Design for Mechanical Measurements* (5th ed.). Hoboken, NJ: John Wiley and Sons, Inc.

Findenegg, G. H., & Herminghaus, S. (1997). Wetting: Statics and Dynamics. *Current Opinion in Colloid & Interface Science, 2*, 301-307.

Flegenheimer, M. (2011, December 21). All 5 Aboard Plane Die as It Crashes on an Interstate in New Jersey, *New York Times*. Retrieved from http://www.nytimes.com/2011/12/21/nyregion/at-least-3-dead-after-small-plane-crashes-on-i-287-in-new-jersey.html

Fletcher, N. H. (2013). Effect of Electric Charge on Collisions between Cloud Droplets. *Journal of Applied Meteorology & Climatology, 52*, 517-520.

Fortin, G., Beisswenger, A., & Perron, J. (2010). Centrifuge Adhesion Tests to Evaluate Icephobic Coatings. *AIAA Paper 2010-7837*.

Freiberger, A., & Lacks, H. (1961). Ice-phobic Coatings for De-icing Naval Vessels. *Naval Research, 1*, 234-249.

Geer, W. C., & Scott, M. (1930). *Technical Notes: The Prevention of Ice Hazards on Planes*. (345). National Advisory Committee for Aeronautics.

Gieck, K., & Gieck, R. (2006). *Engineering Formulas* (8th ed.). New York: McGraw Hill.

Hallett, J., & Isaac, G. A. (2008). Aircraft Icing in Glaciated and Mixed Phase Clouds. *Journal of Aircraft, 45*(6), 2120-2130.

Harireche, O., Verdin, P., Thompson, C. P., & Hammond, D. W. (2008). Explicit Finite Volume Modeling of Aircraft Anti-Icing and De-Icing. *Journal of Aircraft, 45*(6), 1924-1936.

Hicks, R. E. (2013a). *Brief of Accident*. (ERA12FA115). Washington, DC: Retrieved from http://dms.ntsb.gov/aviation/AccidentReports/kv0yp2fjquhfty45tcs45l451/N05212013120000.pdf.

Hicks, R. E. (2013b). *Factual Report Aviation*. (ERA12FA115). Washington, DC: Retrieved from

http://dms.ntsb.gov/aviation/AccidentReports/ezmwfz55kr24yh45x2qjh0451/J05212013120000.pdf.

Hidaka, S., Yamashita, A., & Takata, Y. (2006). Effect of Contact Angle on Wetting Limit Temperature. *Heat Transfer-Asian Research, 35*(7), 513-526.

Janecek, V., & Nikolayev, V. S. (2013). Apparent Contact Angle Model at Partial Wetting and Evaporation: Impact of Surface Forces. *Physical Review E, 87*.

Jellinek, H. H. G., Frankenstein, G. E., & Hanamoto, B. (1981). Method for Reducing the Adhesion of Ice to the Walls of Navigation Locks.

Jin, Z., & Hu, H. (2009). Quantification of Unsteady Heat Transfer and Phase Changing Process Inside Small Icing Water Droplets. *Review of Scientific Instruments, 80*(5).

Jin, Z., & Hu, H. (2010). Icing Process of Small Water Droplets Impinging onto a Frozen Cold Plate. *Journal of Thermodynamics and Heat Transfer, 24*(4), 841-844.

Kako, T., Nakajima, A., Irie, H., Kato, Z., Uematsu, K., Watanabe, T., & Hashimoto, K. (2004). Adhesion and Sliding of Wet Snow on a Super-Hydrophobic Surface with Hydrophilic Channels. *Journal of Materials Science, 39*, 547-555.

Karmakov, I. (2000). Wetting or Non-Wetting Liquid? *Physics Education, 35*(6), 435-438.

Kawanishi, T., Seimiya, T., & Sasaki, T. (1969). Some Remarks on Surface Tension Measurements by the Wilhelmy Method Using a Tilted or a Roughened Plate. *Australian Journal of Chemistry, 22*, 2247-2248.

Korkan, K. D., Dadone, L., & Shaw, R. J. (1983). Performance Degradation of Propeller Systems Due to Rime Ice Accretion. *Journal of Aircraft, 21*(1), 44-49.

Krasovitski, B., & Marmur, A. (2005). Drops Down the Hill: Theoretical Study of Limiting Contact Angles and the Hysteresis Range on a Tilted Plate. *Colloids and Surfaces A: Physicochemical and Engineering Aspects, 136*, 209-215.

Kuo, J. S., Spicar-Mihalic, P., Rodriguez, I., & Chiu, D. T. (2003). Electrowetting-Induced Droplet Movement in an Immiscible Medium. *Langmuir, 19*(2), 250-255.

Labeas, G. N., Diamantakos, I. D., & Sunaric, M. M. (2006). Simulation of the Electroimpulse De-Icing Process of Aircraft Wings. *Journal of Aircraft, 43*(6), 1876-1885.

Landsburg, B. (2008). *Safety Advisory: Aircraft Icing*. Retrieved from http://www.aopa.org/asf/publications/sa11.pdf.

Liu, Y., & German, R. M. (1996). Contact Angle and Solid-Liquid-Vapor Equilibrium. *Acta Metallurgy and Materials, 44*(4), 1657-1663.

Ma, M., & Hill, R. M. (2006). Superhydrophobic Surfaces. *Current Opinion in Colloid & Interface Science, 11*, 193-202.

Mason, J. G., Strapp, J. W., & Chow, P. (2006). The Ice Particle Threat to Engines in Flight. *AIAA Paper 2006-206*.

Miller, D. R., Lynch, C. J., & Tate, P. A. (2004). Overview of High Speed Close-Up Imaging in an Icing Environment. *AIAA Paper 2004-407*.

NASA. (2013a). A Pilot's Guide to Ground Icing, 2013, from http://aircrafticing.grc.nasa.gov/courses.html

NASA. (2013b). A Pilot's Guide to In-Flight Icing, 2013, from http://aircrafticing.grc.nasa.gov/courses.html

Nepf, H. (2003). Visualization based on Refractive-Index Affects. Retrieved from http://web.mit.edu/fluids-modules/www/exper_techniques/6.Shadowgraph_and_Schlierin.pdf

Ohring, M. (2002). *Material Science of Thin Films* (2nd ed.): Academic Press.

Pähtz, T. T., Herrmann, H. J., & Shinbrot, T. T. (2010). Why Do Particle Clouds Generate Electric Charges? *Nature Physics, 6*(5), 364-368.

Panigrahi, P. K., & Maralldhar, K. (2012). *Schlieren and Shadowgraph Methods in Heat and Mass Transfer* (Vol. 2). New York: Springer.

Parthasarathy, S. P., Cho, Y. I., & Back, L. H. (1985). *Fundamental Study of Flow Fields Generated by Rotorcraft Blades Using Wide-Field Shadowgraph*. (JPL PUB 85-64). Pasadena, CA: NASA.

Pierce, E., Carmona, F. J., & Amirfazli, A. (2007). Understanding of Sliding and Contact Angle Results in Tilted Plate Experiments. *Colloids and Surfaces A: Physicochemical and Engineering Aspects, 323*, 73-82.

Qi, Y., Klausner, J. F., & Mei, R. (2004). Role of Surface Structure in Heterogeneous Nucleation. *International Journal of Heat and Mass Transfer, 47*, 11.

Reehorst, A. L., Addy, H. E., & Colantonio, R. O. (2010). Examination of Icing Induced Loss of Control and Its Mitigations. *AIAA Paper 2010-8140*.

Reich, A. (1994). Interface Influences upon Ice Adhesion to Airfoil Materials. *AIAA Paper 94-0714*.

Sakaue, H., Morita, K., Goto, M., Shimizu, M., Hyakutake, T., & Nishide, H. (2008). Chemical Flow Control Method using Combination of Hydrophobic and Hydrophilic Coatings. *AIAA Paper 2008-632*.

Salas-Vernis, J. L., Jayachandran, J. P., Park, S., Kelleher, H. A., Allen, S. A. B., & Kohl, P. A. (2004). Hydrophobic/Hydrophilic Surface Modification Within Buried Channels. *Journal of Vacuum Science and Technology B, 22*(953).

Samaha, M. A., & Gad-al-Hak, M. (2011). Fabrication and Characterization of Low-Cost Superhydrophobic Coatings *AIAA Paper 2011-3275*.

Scavuzzo, R. J., & Chu, M. L. (1987). *Structural Properties of Impact Ices Accreted on Aircraft Structures*. (NASA-CR-179580). NASA.

Scavuzzo, R. J., Chu, M. L., & Ananthaswamy, V. (1994). Influence of Aerodynamic Forces in Ice Shedding. *Journal of Aircraft, 31*(3), 526-530.

Scavuzzo, R. J., Chu, M. L., & Kellacky, C. J. (1990). Impact Ice Stresses in Rotating Airfoils. *Journal of Aircraft, 28*(7), 450-455.

Scavuzzo, R. J., Chu, M. L., Woods, E. J., Raju, R., & Khatkhate, A. A. (1990). Finite Element Studies of the Electro Impulse De-Icing System. *Journal of Aircraft, 27*(9).

Settles, G. S., Hackett, E. B., Miller, J. D., & Weinstein, L. M. (2001). *Full-Scale Schlieren Flow Visualization*: Springer-Verlag.

Shastri, R. P., Ehresman, E. M., & Murthy, S. N. P. (1994). Effects of Water Addition on Combustor Performance. *AIAA Paper 94-3273*.

Smith, T., Prince, M., DeWeese, C., Curtis, L., Weiser, E., & Cano, R. (2008). Coating Reduces Ice Adhesion. *NASA Technical Briefs*, 15.

Sparaco, P. (1994). Swedish Crash Prompts Clear-Ice Guidelines. *Aviation Week and Space Technology*, 49-50.

Thomas, S. K., Cassoni, R. P., & MacArthur, C. D. (1996). Aircraft Anti-Icing and De-Icing Techniques and Modeling. *Journal of Aircraft, 33*(5), 841-854.

Venna, S. V., Lin, Y., & Botura, G. (2007). Piezoelectric Transducer Actuated Leading Edge De-Icing with Simultaneous Shear and Impulse Forces. *Journal of Aircraft, 44*(2), 509-515.

Zhang, Y. F., Yu, X. Q., Zhou, Q. H., & Li, K. N. (2010). Fabrication and Anti-Icing Performance of a Superhydrophobic Copper Surface with Low Adhesion. *Acta Physico-Chimica Sinica, 26*(5), 1457-1462.

Appendix

Collection of raw data from adhesive shear strength tests

Table A-1

Adhesive strength of ice on bare aluminum at -5, -10, -20, and -30℃

[redacted]	Shear Stress (MPa)			
Trial	-5°C	-10°C	-20°C	-30°C
1	0.282	0.229	0.129	0.313
2	0.278	0.143	0.294	0.159
3	0.106	0.228	0.132	0.178
4	0.266	0.118	0.075	0.118
5	0.137	0.271	0.065	0.144
6	0.150	0.092	0.091	0.120
7	0.091	0.231	0.257	0.221
8	0.277	0.274	0.130	0.170
9	0.246	0.090	0.116	0.348
10	0.192	0.145	0.221	0.103
11	0.222	0.169	0.148	0.108
12	0.059	0.109	0.175	0.170
13	0.273	0.164	0.140	0.293
14	0.253	0.156	0.140	0.128
15	0.112	0.263	0.304	0.099
16	0.200	0.127	0.329	0.270

Table A-1 *(cont.)*

	Shear Stress (MPa)			
Trial	-5°C	-10°C	-20°C	-30°C
17	0.226	0.195	0.327	0.298
18	0.285	0.254	0.059	0.120
19	0.242	0.155	0.334	0.228
20	0.240	0.101	0.312	0.314
21	0.255	0.225	0.264	0.107
22	0.268	0.052	0.275	0.340
23	0.254	0.307	0.328	0.322
24	0.061	0.242	0.106	0.187
25	0.248	0.118	0.297	0.221
26	0.264	0.283	0.198	0.228
27	0.278	0.137	0.310	0.164
28	0.220	0.144	0.298	0.167
29	0.272	0.256	0.253	0.150
30	0.193	0.230	0.280	0.262

Table A-2

Adhesive strength of ice on bare substrates.

[redacted]	Shear Stress (MPa)		
Trials	Stainless Steel	Copper	Polycarbonate
1	0.422	0.941	0.692
2	0.401	0.741	0.630
3	0.480	0.408	0.641
4	0.410	0.568	0.654
5	0.403	0.815	0.393
6	0.515	0.444	0.628
7	0.439	0.679	0.541
8	0.457	0.587	0.622

Table A-3

Adhesive strength of ice on methoxymethylethoxypropanol treated substrates.

[redacted]	Shear Stress (MPa)			
Trials	Aluminum	Stainless Steel	Copper	Polycarbonate
1	0.392	1.131	1.198	1.329
2	0.574	1.039	1.334	0.964
3	0.543	1.143	1.226	0.869
4	0.515	1.100	1.262	1.196
5	0.465	1.002	1.319	1.255

Table A-3 *(cont.)*

	Shear Stress (MPa)			
Trials	Aluminum	Stainless Steel	Copper	Polycarbonate
6	0.409	1.175	1.128	1.049
7	0.596	0.999	1.244	1.072
8	0.404	1.038	1.177	1.233

Table A-4

Adhesive strength of ice on polymethylhydrosiloxane treated substrates.

	Shear Stress (MPa)			
Trials	Aluminum	Stainless Steel	Copper	Polycarbonate
1	0.215	0.662	0.912	0.431
2	0.279	0.254	1.153	0.421
3	0.308	0.257	1.201	0.561
4	0.249	0.556	1.095	0.396
5	0.356	0.623	0.731	0.534
6	0.225	0.336	0.672	0.434
7	0.287	0.295	0.647	0.287
8	0.261	0.648	0.829	0.527

Table A-5

Adhesive strength of ice on octylphenol ethoxylate treated substrates.

[redacted]	Shear Stress (MPa)			
Trials	Aluminum	Stainless Steel	Copper	Polycarbonate
1	0.241	0.132	0.406	0.183
2	0.348	0.336	0.591	0.515
3	0.174	0.108	0.568	0.636
4	0.095	0.083	0.532	0.136
5	0.064	0.326	0.589	0.417
6	0.059	0.280	0.632	0.657
7	0.034	0.312	0.523	0.624
8	0.164	0.293	0.461	0.603

Table A-6

Adhesive strength of ice on the variations of aluminum substrates.

[redacted]	Aluminum, Shear Stress (MPa)			
Trials	Bare	Methoxymethyl-ethoxypropanol	Polymethylhydrosiloxane	Octylphenol Ethoxylate
1	0.184	0.392	0.215	0.241
2	0.184	0.574	0.279	0.348
3	0.184	0.543	0.308	0.174
4	0.184	0.515	0.249	0.095

Table A-6 *(cont.)*

[redacted]	Aluminum, Shear Stress (MPa)			
Trials	Bare	Methoxymethyl-ethoxypropanol	Polymethylhydrosiloxane	Octylphenol Ethoxylate
5	0.184	0.465	0.356	0.064
6	0.184	0.409	0.225	0.059
7	0.184	0.596	0.287	0.034
8	0.184	0.404	0.261	0.164

Table A-7

Adhesive strength of ice on the variations of stainless steel substrates.

[redacted]	Stainless Steel, Shear Stress (MPa)			
Trials	Bare	Methoxymethyl-ethoxypropanol	Polymethylhydrosiloxane	Octylphenol Ethoxylate
1	0.422	1.131	0.662	0.132
2	0.401	1.039	0.254	0.336
3	0.480	1.143	0.257	0.108
4	0.410	1.100	0.556	0.083
5	0.403	1.002	0.623	0.326
6	0.515	1.175	0.336	0.280
7	0.439	0.999	0.295	0.312
8	0.457	1.038	0.648	0.293

Table A-8

Adhesive strength of ice on the variations of copper substrates.

[redacted]	Copper, Shear Stress (MPa)			
Trials	Bare	Methoxymethyl-ethoxypropanol	Polymethylhydrosiloxane	Octylphenol Ethoxylate
1	0.941	1.198	0.912	0.406
2	0.741	1.334	1.153	0.591
3	0.408	1.226	1.201	0.568
4	0.568	1.262	1.095	0.532
5	0.815	1.319	0.731	0.589
6	0.444	1.128	0.672	0.632
7	0.679	1.244	0.647	0.523
8	0.587	1.177	0.829	0.461

Table A-9

Adhesive strength of ice on the variations of polycarbonate substrates.

[redacted]	Polycarbonate, Shear Stress (MPa)			
Trials	Bare	Methoxymethyl-ethoxypropanol	Polymethylhydrosiloxane	Octylphenol Ethoxylate
1	0.692	1.329	0.431	0.183
2	0.630	0.964	0.421	0.515
3	0.641	0.869	0.561	0.636

Table A-9 *(cont.)*

	Polycarbonate, Shear Stress (MPa)			
Trials	Bare	Methoxymethyl-ethoxypropanol	Polymethylhydrosiloxane	Octylphenol Ethoxylate
4	0.654	1.196	0.396	0.136
5	0.393	1.255	0.534	0.417
6	0.628	1.049	0.434	0.657
7	0.541	1.072	0.287	0.624
8	0.622	1.233	0.527	0.603